$^{19}\mathrm{F}(\alpha, n)^{22}\mathrm{Na}$, $^{22}\mathrm{Ne}(p, n)^{22}\mathrm{Na}$, and the Role of their Inverses in the Destruction of $^{22}\mathrm{Na}$

Thesis by

Patricia Rose Wrean

In Partial Fulfillment of the Requirements

for the Degree of

Doctor of Philosophy

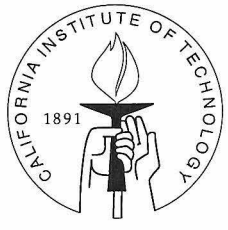

California Institute of Technology

Pasadena, California

1998

(Submitted May 26, 1998)

Acknowledgements

This thesis could not have been written without the support of the many people who helped me during my research at the Kellogg Radiation Lab. I would particularly like to thank my advisor, Dr. Ralph Kavanagh, for his support and guidance, and for teaching me the fine eye for detail needed to be a nuclear physicist. Many thanks are also due to Dr. Charlie Barnes, my mentor, for being a constant source of encouragement, to Bob Carr, our accelerator physicist, who never tired of answering my endless questions, and to my colleague Carl Brune, for taking me under his wing when I first got here and helping me get started in my research. I would also like to acknowledge the technical contributions of the staff at Kellogg: Al Massey, for fixing my electronics, Jim Pendlay, for teaching me AutoCAD, Jack Richards, for supervising me in the machine shop, and Pat Huber, for his work on the Kellogg computer systems. Many thanks are also due to Stefan Schmidt, of the Ruhr-Universität Bochum, Germany, for making the implanted ^{22}Ne targets used in the second half of my thesis project.

I would especially like to express my appreciation to all of my fellow students at Caltech who kept me sane. Particular thanks go to Jim Panetta and Alycia Weinberger, who suffered with me through innumerable problem sets, Mike Kelsey, who inspired me with his enthusiasm for physics, Bill Boone, for patiently listening whenever I really needed to vent, and Leila Belkora and Anita Gould, for teaching me strength in adversity.

My family also supported me every step of the way. I would like to thank my father and mother for believing in me throughout my academic career, and my brother Doug and sister Shelley for being at the other end of the phone whenever I needed them.

And lastly, I am very grateful to my fiancé, Guy Druce, for being my source of strength all the time I've been away from him in Pasadena, and for still being willing to put up with me after I am through.

Financial support for the research presented in this thesis was provided in part

by NSF grants PHY91-15574 and PHY94-20470.

Abstract

The inverses of the $^{19}\mathrm{F}(\alpha, n)^{22}\mathrm{Na}$ and $^{22}\mathrm{Ne}(p, n)^{22}\mathrm{Na}$ reactions may be important destruction mechanisms for $^{22}\mathrm{Na}$ in neutron-rich, high-temperature or explosive nucleosynthesis. I have measured the cross sections for the $^{19}\mathrm{F}(\alpha, n)^{22}\mathrm{Na}$ and $^{22}\mathrm{Ne}(p, n)^{22}\mathrm{Na}$ reactions from threshold to 3.1 and 5.4 MeV, respectively. The absolute efficiency of the 4π neutron detector was determined by Monte Carlo calculations and calibrated using two standard sources and two nuclear reactions. Cross sections for the inverse reactions have been calculated using the principle of detailed balance, and reaction rates for both the reactions and their inverses determined for temperatures between 0.01 and 10 GK for $^{19}\mathrm{F}(\alpha, n)^{22}\mathrm{Na}$ and between 0.1 and 10 GK for $^{22}\mathrm{Ne}(p, n)^{22}\mathrm{Na}$.

Contents

List of Figures

List of Tables

Part I

Introduction

Chapter 1 ^{22}Na and Explosive Nucleosynthesis

The production of long-lived radioisotopes in novae and supernovae is of particular interest, due to the possibility of observing the γ rays of their decay. Current stellar, supernova, and nova models predict the formation of many such radioisotopes, including ^{60}Fe, ^{26}Al, ^{44}Ti, and ^{22}Na, which have lifetimes of 2.2×10^6, 1.1×10^6, 71, and 3.8 years respectively. Because of their long lifetimes, ^{60}Fe and ^{26}Al tend to be observed as a steady, diffuse source of γ rays from our galaxy, while ^{44}Ti and ^{22}Na would most likely be observed as emanating from the site of origin, due to their relatively short lifetimes.

The galactic distribution of ^{26}Al has been studied [Die97], but for ^{60}Fe only an upper limit, close to the predicted intensities, has been published. Remarkably, γ rays from ^{44}Ti have been seen in the Cas A supernova remnant which is $\sim$ 300 years old [Die97]. Also, γ rays from ^{56}Ni $\rightarrow$ ^{56}Co $\rightarrow$ ^{56}Fe and ^{57}Co $\rightarrow$ ^{57}Fe have been seen in the debris from SN1987A, but their lifetimes are short enough (8.8, 111.5, and 392 days for ^{56}Ni, ^{56}Co, and ^{57}Co, respectively) that they have not been identified in the galactic γ-ray background.

Because of the long mean time between galactic supernovae (about 30 years for Type II supernovae [Tim95]), observational limits on the intensities of ^{22}Na lines (511 and 1275 keV) can put constraints on nucleosynthetic yields of these radioisotopes in individual supernovae. In the case of novae, which have a much shorter mean time between them (a rate of around 40/year in our galaxy [Mah82]), observational limits on the amount of ^{22}Na could in principle provide information about the average galactic production rate of ^{22}Na in novae. At this time, no ^{22}Na γ rays have been observed, either in the diffuse background or from discrete events.

It is possible for the lifetime of ^{22}Na in a neutron flux to be dominated not by its

radioactive decay, but rather by the destruction mechanisms of $^{22}\mathrm{Na}(n,p)^{22}\mathrm{Ne}$ and $^{22}\mathrm{Na}(n,\alpha)^{19}\mathrm{F}$. In this thesis, I measure cross sections and reaction rates which may serve as a guide in determining which mechanism will dominate the fate of ^{22}Na, given the ambient neutron flux.

1.1 Supernovae and ^{22}Na Production

In 1975, D.D. Clayton first discussed the possibility of detecting ^{22}Na produced in supernovae by the following sequence of reactions [Cla75]:

$$^{14}\mathrm{N}(\alpha,\gamma)^{18}\mathrm{F}(\alpha,p)^{21}\mathrm{Ne}(p,\gamma)^{22}\mathrm{Na}\ . \tag{1.1}$$

For peak temperatures of about 0.6 GK, this and similar series of reactions could create large concentrations of ^{22}Na. Clayton states that the ^{22}Na yield is strongly temperature-dependent, and suggests that the yield of ^{22}Na would serve as a "thermometer" for Type II supernovae.

Recent computer simulations of explosive hydrodynamics and nucleosynthesis in Type II supernovae, performed by Woosley and Weaver [Woo95] and Thielemann, Nomoto, and Hashimoto [Thi96], give the amounts of ^{22}Na that would be produced in a supernova depending upon the initial conditions of the star. Woosley and Weaver verify Clayton's prediction [Cla75] that ^{22}Na is produced by protons, spalled by neutrinos from abundant elements such as ^{16}O and ^{20}Ne, being captured by ^{21}Ne. The ejected mass of ^{22}Na calculated by Woosley and Weaver varies from 8×10^{-8} $\mathrm{M}_\odot$ for a 12 $\mathrm{M}_\odot$ star with metallicity $Z = Z_\odot$ to 2×10^{-5} $\mathrm{M}_\odot$ for a 40 $\mathrm{M}_\odot$ star with $Z = 0.01Z_\odot$, and 3×10^{-16} $\mathrm{M}_\odot$ for a 35 $\mathrm{M}_\odot$ star with $Z = 0$. Woosley and Weaver also note that the yield of ^{22}Na depends in part on neutrino irradiation: for a 25 $\mathrm{M}_\odot$ star, the effect of neutrino irradiation increases the amount of ^{22}Na ejected from 1.6×10^{-6} to 3.4×10^{-6} $\mathrm{M}_\odot$ for $T_\nu = 8$ GK. In an earlier paper [Woo80], they state that yields of 3×10^{-5} $\mathrm{M}_\odot$ of ^{22}Na would give clearly discernible signals from a galactic supernova explosion.

Initial stellar mass ($M_\odot$)	Ejected mass of ^{22}Na($M_\odot$)	
	Woosley and Weaver	Thielemann *et al.*
13	1.45×10^{-7}	9.84×10^{-8}
15	1.09×10^{-6}	3.98×10^{-8}
20	2.96×10^{-7}	1.33×10^{-7}
25	3.43×10^{-6}	2.56×10^{-7}

Table 1.1: Comparison of ejected masses of ^{22}Na calculated by Woosley and Weaver and by Thielemann, Nomoto, and Hashimoto.

Similar calculations by Thielemann, Nomoto, and Hashimoto [Thi96] give similar yields for the most abundant isotopes, but differ in the ejected masses of ^{22}Na, as shown in Table 1.1. (There is a discussion of the differences between the theoretical models of the two groups in the Woosley and Weaver paper.)

Observational constraints on the amount of ^{22}Na produced in supernovae may serve to verify these theoretical models. Woosley and Weaver [Woo80] note, however, that due to ^{22}Na's short half-life, a calculation of the γ transport in the expanding supernova remnant is required for a meaningful analysis of the yield of γ rays from ^{22}Na that one would expect to observe given these ejected masses. This may be a complex matter because of the possibility of a non-isotropic expansion of the supernovae ejecta, as seen in some 2-dimensional models, and suggested by SN1987A.

1.2 ^{22}Na Production in Novae

Network calculations [Sta97, Jos97, Coc95, Sta93] have shown that ^{22}Na may be formed in "astrophysically interesting" quantities (on the order of 10^{-5} $M_\odot$) for novae involving an ONeMg white dwarf. Although these calculations include the effects of all relevant reactions, ^{22}Na is produced predominantly by reactions in the Ne-Na cycle, as shown in Figure 1.1.

As roughly 25% of well studied novae are classified as neon-type novae [Jos97], and about 40 novae occur in the Galaxy per year [Mah82], the 1275-keV line from the decay of ^{22}Na (with a mean life of 3.75 years) should be observable from many

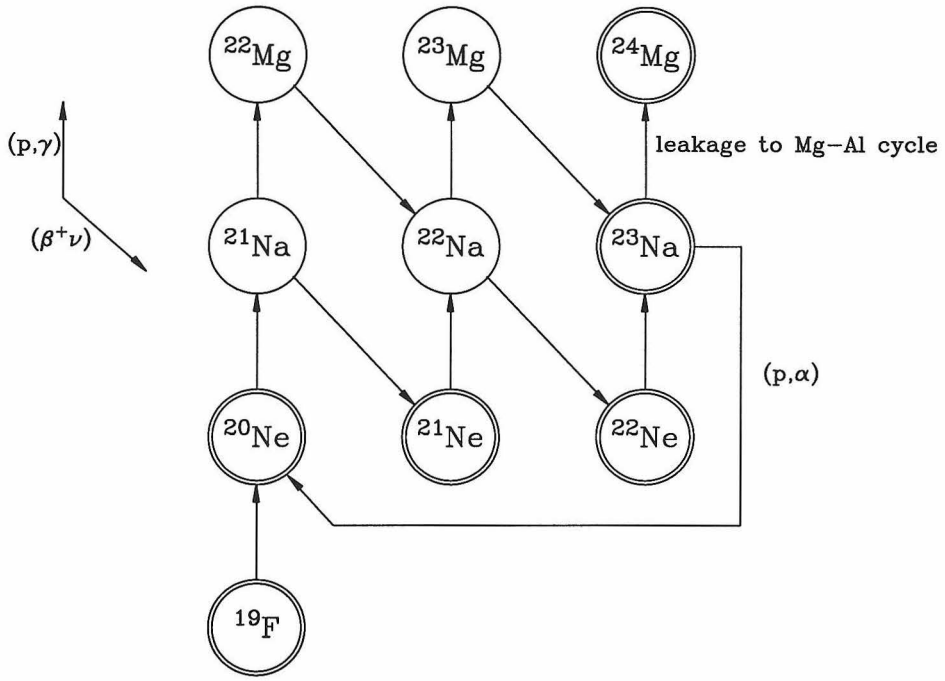

Figure 1.1: The Ne-Na cycle. Stable nuclei are indicated by double circles.

such novae.

Although the possibility in such a nova of a neutron flux great enough to destroy ^{22}Na seems remote, it is interesting to note that all searches by gamma-ray telescopes, such as HEAO3 [Mah82], and, more recently, COMPTEL [Iyu95], have failed to detect ^{22}Na in any quantity, and have only set upper limits on ^{22}Na production. In particular, the COMPTEL results give an average 2σ upper limit on the ejected mass of ^{22}Na of 4×10^{-8} $M_\odot$ from a neon-type nova.

1.3 ^{22}Na and the Ne-E anomaly

The study of the isotopic composition of meteorites has revealed some perplexing anomalies, in that the isotopic abundances of certain elements vary greatly from the abundances of terrestrial material. Such anomalies include the presence of excess ^{129}Xe, thought to be due to the decay of ^{129}I [Rey60], excess ^{26}Mg, the daughter of ^{26}Al [Lee76], and the presence of almost pure ^{22}Ne, known as Ne-E [Wie81].

Various scenarios for the origins of Ne-E have been suggested: implantation from a wind from ^{22}Ne-rich He-burning shells of low-mass asymptotic giant branch (AGB) stars [Lew90, Gal90], nuclear reactions induced by the collision of two large planets in the solar system (!) [Hol95], and the presence of ^{22}Na in the grains from which the meteorite was formed, which then decays to ^{22}Ne *in situ* by positron emission and electron capture. However, Clayton [Cla92] asserts that the envelopes of low-mass AGB stars contain too much ^{20}Ne to be a source of Ne-E. Further, the fact that the Ne-E in some ordinary chondrites is released at temperatures less than 800°C [Nie77] imposes strong constraints on the temperature of incorporation and subsequent history. Holden and Woolfson [Hol95] state that the 3.8-year lifetime of ^{22}Na implies that the raw material containing ^{22}Na must have cooled over a time scale of only tens of years, which is at variance with the timescales for meteorites containing excess ^{129}Xe (on the order of 2×10^8 years). Possibly, all that is required is that grains containing ^{22}Na formed quickly, the ^{22}Na decayed *in situ*, and the grains were built into the material later found as meteorites on a more relaxed time schedule.

If Ne-E is due to the presence of ^{22}Na (the generally accepted theory), in a neutron-rich environment the (n,p) and (n,α) reactions may also be important. Although the reaction $^{22}\mathrm{Na}(n,p)^{22}\mathrm{Ne}$ also results in ^{22}Ne, the (n,α) reaction would result in some of the ^{22}Na being converted into ^{19}F. A knowledge of the reaction rates for the (n,α) and (n,p) reactions is necessary to determine whether the (n,α) reaction would significantly affect the production of ^{22}Ne under neutron-rich conditions.

Chapter 2 Theoretical Overview

2.1 Energy Levels of ^{22}Na

Figure 2.1 shows the energy-level diagram for ^{22}Na [End90]. The Q-value and threshold energy for the $^{19}\mathrm{F}(\alpha,n)^{22}\mathrm{Na}$ reaction are $-1951.7(5)$ and 2362.9(6) keV, respectively, while the $^{22}\mathrm{Ne}(p,n)^{22}\mathrm{Na}$ reaction has a Q-value and threshold energy of $-3624.6(5)$ and 3790.7(5) keV, respectively [Nat98]. For the $^{19}\mathrm{F}(\alpha,n)^{22}\mathrm{Na}$ reaction, only reactions involving the ground state of ^{22}Na and hence the n_0 neutron group, were experimentally accessible. The $^{22}\mathrm{Ne}(p,n)^{22}\mathrm{Na}$ data, however, ranged in energy from 3.6 to 5.4 MeV, *i.e.,* from below the n_0 threshold to above the n_4 threshold.

2.2 Reaction Kinematics

Consider the reaction $1 + 2 \rightarrow 3 + 4 + Q$, as shown in Figure 2.2, in which Q is the energy released in the reaction (endothermic reactions have a negative Q-value). The total energy in the center-of-mass frame, W, is related to the total energy in the lab frame, W_{lab}, by

$$W = \frac{W_{lab}}{\gamma} \tag{2.1}$$

where γ is defined as

$$\gamma \equiv \frac{1}{\sqrt{1-\beta^2}}\,, \tag{2.2}$$

and β, $\frac{1}{c}$ times the velocity of the center-of-mass frame with respect to the laboratory frame, is given by [Ded62]

$$\beta = \frac{\sqrt{E_{lab}(E_{lab}+2m_1)}}{(E_{lab}+m_1+m_2)}\,. \tag{2.3}$$

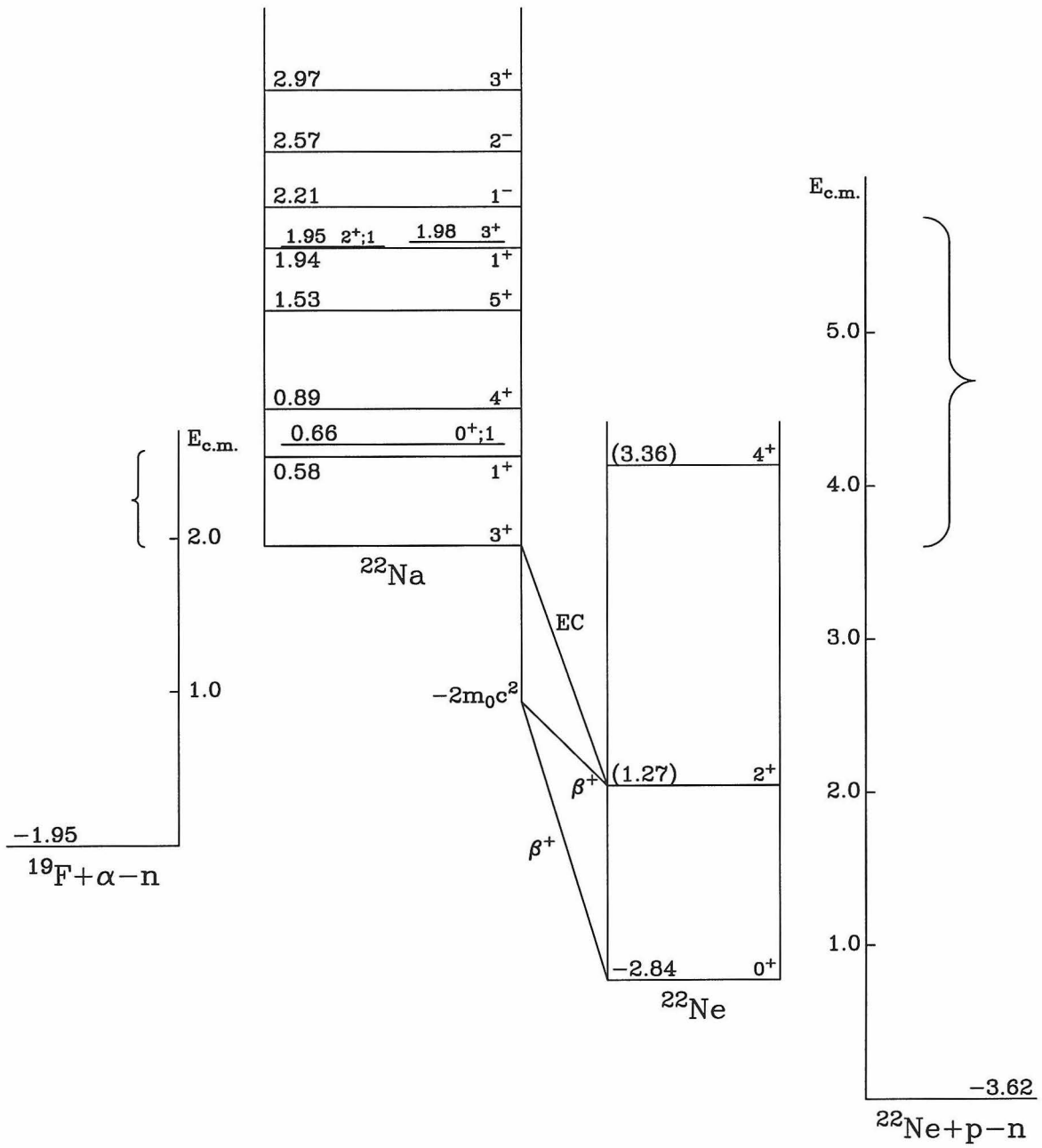

Figure 2.1: The ^{22}Na energy-level diagram. All energies are given in MeV. Energies given in brackets are relative to the ground state of ^{22}Ne; all other energies are given relative to the ground state of ^{22}Na. The brackets denote the experimentally accessible energies. The branching ratio for the decay of ^{22}Na to the ground state of ^{22}Ne is 0.07(2)% [Sai90].

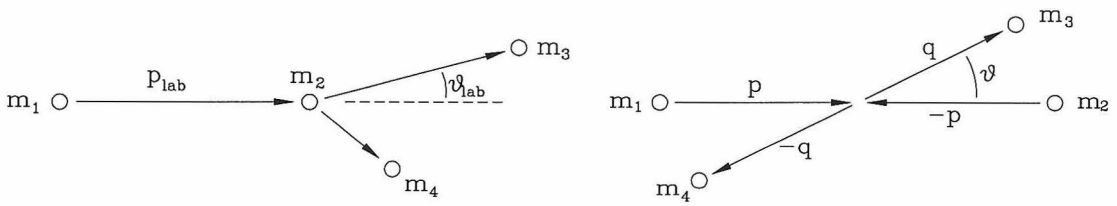

Figure 2.2: Reaction kinematics.

Here m_i is the mass of the ith particle, and E_{lab} is the kinetic energy of the bombarding particle in the lab frame (*i.e.*, the beam energy). Since $W_{lab} = E_{lab} + m_1 + m_2$, equation 2.1 may be rewritten as

$$W = \frac{1}{\gamma}(E_{lab} + m_1 + m_2) \ , \tag{2.4}$$

which may be simplified to

$$W = \sqrt{(m_1 + m_2)^2 + 2m_2 E_{lab}} \ . \tag{2.5}$$

The relationship between the momentum of particle 1 in the center-of-mass frame, p, and its momentum in the lab frame, p_{lab}, is [Jac75]

$$p = \frac{m_2 \ p_{lab}}{W} \ . \tag{2.6}$$

Writing p_{lab} in terms of E_{tot}, the total energy of the particle in the lab frame,

$$p_{lab} = \sqrt{E_{tot}^2 - m_1^2} = \sqrt{E_{lab}^2 + 2m_1 E_{lab}} \ , \tag{2.7}$$

since $E_{tot} = E_{lab} + m_1$. Therefore

$$p = \frac{m_2}{W}\sqrt{E_{lab}^2 + 2m_1 E_{lab}} \ . \tag{2.8}$$

The energy and momentum of particle 3, E_3 and q, in the center of mass frame

are given by [Ded62]

$$E_3 = \frac{m_2}{W}[E_{lab} - E_{th} + \frac{m_3}{m_2}(m_3 + m_4)] \tag{2.9}$$

and

$$q = \frac{m_2\sqrt{(E_{lab} - E_{th})(E_{lab} - E_d)}}{W} , \tag{2.10}$$

where

$$E_d = \frac{1}{2m_2}[(m_3 - m_4)^2 - (m_1 + m_2)^2] \tag{2.11}$$

and

$$E_{th} = \frac{1}{2m_2}[(m_3 + m_4)^2 - (m_1 + m_2)^2] . \tag{2.12}$$

For endoergic reactions, E_{th} is the threshold energy. The above expressions are of use in the calculation of cross sections using the principle of detailed balance (Section 2.6).

The energy in the lab frame, $E_{3,lab}$, and the lab angle, θ_{lab}, for particle 3 are derived from the above quantities using the following relations [Ded62]. The energy of the third particle in the lab frame is given by the usual Lorentz transformation

$$E_{3,lab} = \gamma(E_3 + q\ \beta\cos\theta) , \tag{2.13}$$

and by substituting in for γ, E_3, β, and q, an expression for $E_{3,lab}$ may be obtained which depends only on θ and the known quantities E_{lab} and m_i. Similarly, an expression for θ_{lab} in terms of these quantities may be found from [Ded62],

$$\tan\theta_{lab} = \frac{\sqrt{1-\beta^2}\sin\theta}{\cos\theta + g_3} , \tag{2.14}$$

where g_3 is the rather complicated expression

$$g_3 = \frac{[E_{lab} - E_{th} + \frac{m_3}{m_2}(m_3 + m_4)]}{(E_{lab} + m_1 + m_2)}\sqrt{\frac{E_{lab}(E_{lab} + 2m_1)}{(E_{lab} - E_{th})(E_{lab} - E_d)}} . \tag{2.15}$$

These relativistic expressions were used for the neutron energy and lab angle in the

generation of neutrons with the correct momentum distribution for the Monte Carlo calculations (Section 6.4).

2.3 Cross Sections and Resonance Strengths

The cross section for a single, narrow resonance in the nuclear reaction $(1+2 \rightarrow 3+4)$ at center-of-mass energy E is given by the Breit-Wigner formula [Fow67]

$$\sigma(E) = \frac{\pi\hbar^2}{2\mu E} \frac{\omega_r \Gamma_1 \Gamma_2}{(E - E_r)^2 + \Gamma^2/4} , \tag{2.16}$$

where μ is the reduced mass of the particles in the entrance channel, E_r is the energy of the resonance in the center of mass frame, Γ_1 and Γ_2 are the partial widths in the center-of-mass frame for the decay of the resonant state into particles $1+2$ and $3+4$ respectively, Γ is the sum over all partial widths ($\Gamma = \Sigma\Gamma_i$), and ω_r is the statistical factor

$$\omega_r = (1 + \delta_{12}) \frac{g_r}{g_1 g_2} . \tag{2.17}$$

The terms in the statistical factor are the Kronecker delta, δ_{12}, which accounts for the possibility that the two particles in the entrance channel might be identical, and g_i, the spin multiplicity of the ith particle. The spin multiplicity is calculated from $g_i = 2J_i + 1$, where J_i is the spin of the ith particle and g_r and J_r are the spin multiplicity and spin of the resonant state, respectively.

The strength of a resonance, $(\omega\gamma)_r$, is defined as [Fow67]

$$(\omega\gamma)_r \equiv \omega_r \gamma_r \equiv \left(\frac{\omega \Gamma_1 \Gamma_2}{\Gamma} \right)_r , \tag{2.18}$$

and is related to the integral of the cross section over the resonance by

$$(\omega\gamma)_r = \frac{\mu E_r}{\pi^2 \hbar^2} \int_r \sigma(E) dE , \tag{2.19}$$

obtained by integrating Equation 2.16. Since for a Breit-Wigner resonance

$$\int \sigma(E)dE = \frac{\pi}{2}\sigma(E_r)\Gamma_r \ , \tag{2.20}$$

the strength of the resonance may also be written as

$$(\omega\gamma)_r = \frac{\mu E_r \sigma(E_r)\Gamma_r}{2\pi\hbar^2} \ . \tag{2.21}$$

2.4 Experimental Yields

The yield of neutrons detected per incident particle, Y_n, for an ideal, thin, and uniform target and monoenergetic beam of energy E_b is given by

$$Y_n = (nt)\sigma(E_b)\varepsilon(E_b) \ , \tag{2.22}$$

where (nt) is the areal number density of target atoms, σ is the reaction cross section, and ε is the neutron-detection efficiency. For a target which is not infinitesimally thin, the beam loses energy as it passes through the target, and the yield is then given by

$$Y_n = \int_{E_t}^{E_b} \frac{\sigma(E')\varepsilon(E')f dE'}{\frac{dE}{dX}(E')} \ , \tag{2.23}$$

in which $E_t = E_b - \Delta E$, where ΔE is the energy loss of the beam in the target, f is the number of target atoms in each target molecule, and $\frac{dE}{dX}(E')$ is the stopping power per target molecule. Here the laminar thickness dX in the stopping power is measured in target molecules per unit area.

If the target is sufficiently thick that the beam is completely stopped in the target, the resulting yield is called the thick-target yield and is given by

$$Y_{\text{thick}} = \int_0^{E_b} \frac{\sigma(E')\varepsilon(E')f dE'}{\frac{dE}{dX}(E')} \ . \tag{2.24}$$

If the variation in the detection efficiency and stopping power are negligible over

a particular resonance, then the areal density of the target, (nt), of a target may be derived from the yield of that resonance by combining equations 2.19 and 2.23:

$$(nt) = \frac{\mu E_r}{\pi^2 \hbar^2 \ (\omega\gamma)_r \ \varepsilon(E_r)} \int_r Y(E) dE \ . \tag{2.25}$$

2.5 Reaction Rates

In stars and supernovae, nuclei are not monoenergetic, but almost always have a Maxwell-Boltzmann distribution of velocities characterized by their temperature. To determine the rate at which the nuclei react, the energy-dependent cross section must then be averaged over this velocity distribution. The rate at which reactions will occur is therefore given by

$$r(T) = \frac{n_i n_j}{1 + \delta_{ij}} N_A \langle \sigma v \rangle \ , \tag{2.26}$$

where $r(T)$ is the reaction rate per unit volume as a function of temperature (with units moles cm^{-3} s^{-1}), n_i and n_j are the number densities of the reactants, and $N_A\langle \sigma v \rangle$ is the product of the cross section and the relative velocity of particles i and j averaged over the Maxwell-Boltzmann velocity distribution. $N_A\langle \sigma v \rangle$ is found by convoluting the cross section with a Maxwell-Boltzmann distribution [Fow67] as follows:

$$N_A \langle \sigma v \rangle = \left(\frac{8}{\mu \pi} \right)^{\frac{1}{2}} \frac{N_A}{(kT)^{\frac{3}{2}}} \int_0^\infty \sigma(E) E \exp\left(\frac{-E}{kT} \right) dE \ , \tag{2.27}$$

where N_A is Avogadro's number, k is Boltzmann's constant, T is the temperature, and E is the energy in the center of mass frame.

For a single resonance, if the full width of the resonance Γ_r is much less than the effective spread in energy of the interacting particles, then the reaction rate may be approximated by

$$N_A \langle \sigma v \rangle = N_A \left(\frac{2\pi\hbar^2}{\mu k T} \right)^{\frac{3}{2}} \frac{(\omega\gamma)_r}{\hbar} \exp\left(\frac{-E_r}{kT} \right) \ . \tag{2.28}$$

2.6 Detailed Balance

The principle of detailed balance allows us to calculate the cross section of a reaction from its inverse. The relation between the cross section of the reaction $1+2 \rightarrow 3+4$ and its inverse is given by [Fow67, Seg77]

$$\frac{\sigma_{34\rightarrow 12}}{\sigma_{12\rightarrow 34}} = \frac{(1+\delta_{34})}{(1+\delta_{12})} \frac{g_1 g_2}{g_3 g_4} \frac{{p_1}^2}{{p_3}^2} , \tag{2.29}$$

where p_i is the momentum of the ith particle in the center of mass system. Substituting in equations 2.8 and 2.10 gives

$$\frac{\sigma_{34\rightarrow 12}}{\sigma_{12\rightarrow 34}} = \frac{(1+\delta_{34})}{(1+\delta_{12})} \frac{g_1 g_2}{g_3 g_4} \frac{(E_{lab}^2 + 2m_1 E_{lab})}{(E_{lab} - E_{th})(E_{lab} - E_d)} . \tag{2.30}$$

Similarly, the ratio of reaction rates for a reaction and its inverse is [Fow67]

$$\frac{N_A\langle\sigma v\rangle_{34\rightarrow 12}}{N_A\langle\sigma v\rangle_{12\rightarrow 34}} = \frac{(1+\delta_{34})}{(1+\delta_{12})} \frac{g_1 g_2}{g_3 g_4} \left(\frac{m_1 m_2}{m_3 m_4}\right)^{\frac{3}{2}} \exp\left(\frac{-Q}{kT}\right) , \tag{2.31}$$

where m_i is the mass of the ith particle.

The ratio between resonance strengths for the forward and inverse reactions is much simpler: since $(\omega\gamma)_r$ is proportional to the product of the partial widths for the entrance and exit channels, the partial widths cancel and the ratio is just

$$\frac{(\omega\gamma)_{34}}{(\omega\gamma)_{12}} = \frac{(\omega)_{34}}{(\omega)_{12}} = \frac{g_3 g_4}{g_1 g_2} . \tag{2.32}$$

The relationship between the energies corresponding to these resonance strengths can be found using equation 2.5.

Chapter 3 Experimental Overview

The goal of the present experiment is to measure the absolute cross sections of $^{19}\mathrm{F}(\alpha, n)^{22}\mathrm{Na}$ and $^{22}\mathrm{Ne}(p, n)^{22}\mathrm{Na}$ in order to guide further calculation of the thermonuclear reaction rates for the destruction of ^{22}Na in a neutron-rich environment.

3.1 Previous Work

3.1.1 Direct Measurements of $^{22}\mathrm{Na}(n,p)^{22}\mathrm{Ne}$ and $^{22}\mathrm{Na}(n,\alpha)^{19}\mathrm{F}$

Although direct measurements of the $^{22}\mathrm{Na}(n, p)^{22}\mathrm{Ne}$ cross section at (terrestrial) thermal neutron energies had previously been made [Kvi81, Ehe73], the first measurement of the cross section of this reaction as a function of energy was made by Gledenov *et al.* [Gle82], for energies from thermal up to 370 eV. They used a target of ^{22}NaCl, a silicon semiconductor detector to detect the protons, and neutrons and the time-of-flight spectrometer from the IBR-30 pulsed reactor at the Joint Institute for Nuclear Research Laboratory of Neutron Physics in Dubna, near Moscow.

Direct measurements of $^{22}\mathrm{Na}(n, \alpha)^{19}\mathrm{F}$ as well as the $^{22}\mathrm{Na}(n, p)^{22}\mathrm{Ne}$ reaction at thermal neutron energies have also been made by Koehler and O'Brien [Koe88]. In addition, they measured the p_0 and p_1 cross sections from thermal energy to 420 eV and 35 keV, respectively, for the $^{22}\mathrm{Na}(n, p)^{22}\mathrm{Ne}$ reaction, using the neutron source at LANSCE, the Los Alamos Neutron Scattering Center, with a ^{22}NaCl target. For the thermal neutron measurements, they used the Omega West Reactor at the Los Alamos National Laboratory. The protons and α-particles in both measurements were detected with silicon surface-barrier detectors.

However, for $^{22}\mathrm{Na}(n, \alpha)^{19}\mathrm{F}$, no data exist above thermal energies, while for the $^{22}\mathrm{Na}(n, p)^{22}\mathrm{Ne}$ reaction, few data exist for $E_n > 1$ keV, in which case we must turn to the inverse reactions and the principle of detailed balance.

3.1.2 Measurements of ^{19}F(α,n)^{22}Na

Measurements of the $^{19}\mathrm{F}(\alpha, n)^{22}\mathrm{Na}$ cross section have been made by Balakrishnan *et al.* [Bal78] and van der Zwan and Geiger [Zwa77]. Balakrishnan *et al.* used a paraffin-moderated 4π detector to measure the cross section between 2.6 and 5.1 MeV, while van der Zwan and Geiger used a stilbene crystal to measure the 0° cross section from threshold to 4.7 MeV. Earlier efforts include those by Ehehalt *et al.* [Ehe73], who measured the $^{19}\mathrm{F}(\alpha, n)^{22}\mathrm{Na}$ and $^{22}\mathrm{Ne}(p, n)^{22}\mathrm{Na}$ cross sections near the neutron threshold, Freeman and Mani [Fre64], who measured the $^{19}\mathrm{F}(\alpha, n)^{22}\mathrm{Na}$ excitation function from 3.05 to 4.9 MeV, and Williamson *et al.* [Wil60], who determined the yield curve from threshold to 4 MeV. Angular distributions for this reaction for beam energies ranging from 3.4 to 4.6 MeV have been measured by Batchelor and Towle [Bat59].

The thick-target yield for $^{19}\mathrm{F}(\alpha, n)^{22}\mathrm{Na}$ has also been measured by the following groups: Heaton *et al.* [Hea89], from 2.4 to 9.8 MeV; Norman *et al.* [Nor84], from 3.5 to 10.0 MeV, with cross sections calculated from the slope of the thick target yield *vs.* energy curve; and Bair and Gomez del Campo [Bai79], from 3.5 to 8.0 MeV.

3.1.3 Measurements of ^{22}Ne(p,n)^{22}Na

Two total cross section measurements for $^{22}\mathrm{Ne}(p, n)^{22}\mathrm{Na}$ have been performed, both using gas-cell targets. Saam *et al.* [Saa89] measured the cross section for three proton energies: 7, 12, and 16 MeV, while more recently Takács*et al.* [Tak96] extended these measurements by taking 15 points within the energy range 5.5–17.3 MeV.

3.1.4 Theoretical Calculations of Reaction Rates

Theoretical reaction rates are available for $^{22}\mathrm{Na}(n, \alpha)^{19}\mathrm{F}$ and $^{22}\mathrm{Na}(n, p)^{22}\mathrm{Ne}$, based on Hauser-Feshbach theory and calculated by Woosley *et al.* [Woo78]. However, the authors state that these calculations can only be expected to agree with the actual rate to within a factor of about two or three.

3.2 Scope of this Work

Although the $^{19}F(\alpha, n)^{22}Na$ reaction has been well-studied, as described above, there has been no total cross section measurement from threshold to 2.5 MeV (the lower limit of the Balakrishnan experiment). Although the van der Zwan data do cover this energy range, only the 0° cross section was measured, and angular distributions would be necessary to determine the total cross section from their data. My intent, therefore, is to measure the total cross sections for $^{19}F(\alpha, n)^{22}Na$ from threshold (2362.9(6) keV) to the limit of the accelerator. Since this measurement necessarily involves only the ground state of ^{19}F, only the $^{22}Na(n, \alpha_0)^{19}F$ reaction rate may be determined directly from these cross sections.

The existing cross section measurements for $^{22}Ne(p, n)^{22}Na$ all lie within the energy range 5.5–17.3 MeV, and further have large errors associated with the gas-cell target. In this experiment, I will measure the $^{22}Ne(p, n)^{22}Na$ total cross sections from threshold (3790.7(5) keV) to 5.4 MeV (the n_1 threshold), where no measurements have yet been made. Again, since this measurement necessarily involves only the ground state of ^{22}Ne, only the $^{22}Na(n, p_0)^{22}Ne$ reaction rate may be determined directly from these cross sections.

Part II

Experimental Apparatus and Procedures

Chapter 4 Pelletron Beams

The proton and α^+ beams were provided by the 3-MV Pelletron tandem accelerator at the Kellogg Radiation Laboratory. The proton beams, supplied by either the internal RF ion source or the external sputter source, ranged in energy from 340 keV to 5.8 MeV, while the α^+ beams, supplied by the internal ion source, ranged from 600 keV to 3.1 MeV. The pressure of the insulating SF_6 gas in the Pelletron tank was varied from its usual operating value of 70 psi to 45 psi for low-energy beams and to 80 psi for high-energy beams. For both the low-energy proton and α^+ beams, varying lengths of the accelerating tube were shorted out in order to get the desired voltage gradient for these low terminal potentials. The beam intensities of both protons and α^+'s were varied from tens of nA to 20 μA, depending on the neutron yield.

The beam energy was determined by a 90° analyzer magnet whose field was measured by both an NMR gaussmeter and a Hall probe. The energy of the beam, E_{lab}, is related to the field of the analyzer magnet by

$$E_{lab} = \sqrt{(kqB)^2 + m^2} - m \,, \tag{4.1}$$

where m and q are the mass and charge state of the beam, respectively, and k is the magnet constant. To calibrate the α^+ beam energies, as determined by the NMR gaussmeter, individual values of k were determined using the 1053.18(18)-keV resonance [Bru93] in $^{13}C(\alpha, n)$ and nine resonances ranging from 1530.03 to 2994.4 keV [Maa78] in $^{24}Mg(\alpha, \gamma)$, and are shown in Figure 4.1. The error bars plotted in the figure represent the statistical errors and do not include the uncertainty due to possible small changes in the trajectory of the beam or the error associated with being on a different part of the hysteresis curve after cycling the magnet. The resulting weighted average of k is 0.014959(4) MeV/gauss. The 1σ error bar for k was determined not only from the above measurements, but also on the observed limits

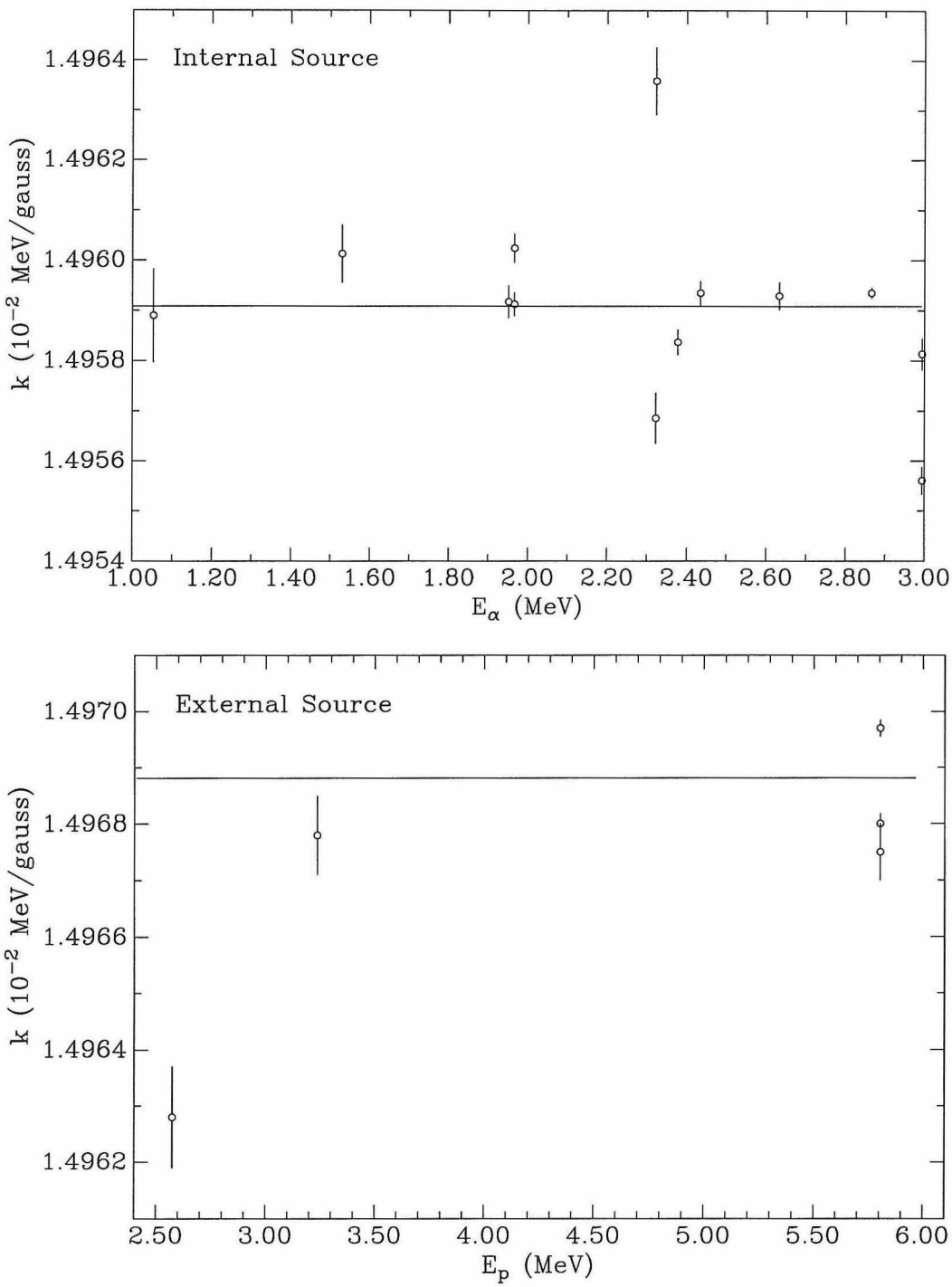

Figure 4.1: Determining the magnet constant k as a function of beam energy for calibration of the beam energies. The error bars represent the statistical errors.

on the repeatability of the resonance energies in $^{19}F(\alpha, n)^{22}Na$. The associated α^+ beam energies have an uncertainty of $\pm 0.05\%$.

For the proton beams provided by the external sputter source, k was measured using the 2574.3(3)-keV threshold in $^{18}O(p, n)^{18}F$, the 3235.5(3)-keV threshold in $^{13}C(p, n)^{13}N$, and the 5803.68(10)-keV threshold in $^{27}Al(p, n)^{27}Si$ [Nat98], and the results are also plotted in Figure 4.1. From these measurements, k was found to be 0.014969(7) MeV/gauss, with the error calculated from both these measurements and the repeatability of the resonance energies observed from the $^{22}Ne(p, n)^{22}Na$ measurements. The proton beam energies calculated from this constant are estimated to have an uncertainty of $\pm 0.1\%$.

During all runs, the trajectory of the beam was determined by the balancing of the fringes of the transmitted beams on the horizontal image slits by the feedback loop regulating terminal voltage, and by the balancing of the incident beams on the horizontal object slits by the operator. Although the slit widths are adjustable parameters, a total width of 2 mm for both the image and object slits was used for the duration of this experiment, and I estimate the consequent energy resolution to be $< 0.05\%$, *i.e.,* 1.5 keV for a 3 MeV beam.

Chapter 5 0° Beamline

The Pelletron accelerator has four beamlines, named after their angle with respect to a central east-west line. The beamline used in this experiment runs due west from the switching magnet and is called the 0° beamline. A scale diagram of this beamline is shown in Figure 5.1, showing the relative positions of the beam optics, vacuum system, target chamber, and neutron detector.

For the $^{19}F(\alpha, n)^{22}Na$ measurement, the beam was collimated by a 1.25 cm diameter Ta collimator located 70.5 cm upstream from the target, while a 0.5 cm diameter Ta collimator in the same location was used in the $^{22}Ne(p, n)^{22}Na$ experiment. The collimator is located at that distance from the target so that neutrons created by fringes of the beam striking the collimator are outside the active volume of the neutron detector, and are thus detected at a reduced efficiency. The collimator size was chosen to maximize the area of the target bombarded by the beam while ensuring that the beam could only strike the target and not any other part of the target chamber; as the implantation area of the ^{22}Ne targets was only $\sim$ 1 cm in diameter, a smaller collimator had to be used for those measurements. A suppression ring at -400 V was placed 14 cm downstream from the collimator in both experiments to ensure accurate beam integration by preventing electrons induced by the beam from entering the target chamber from upstream and preventing secondary electrons from leaving the target chamber.

The vacuum measured by the target chamber ion gauge was always less than 6×10^{-7} torr, while the pressure in the scattering chamber directly over the turbopump was typically 3×10^{-7} torr.

In order to minimize target deterioration, the beam was rastered over the aperture of the collimator by magnetic steerers.

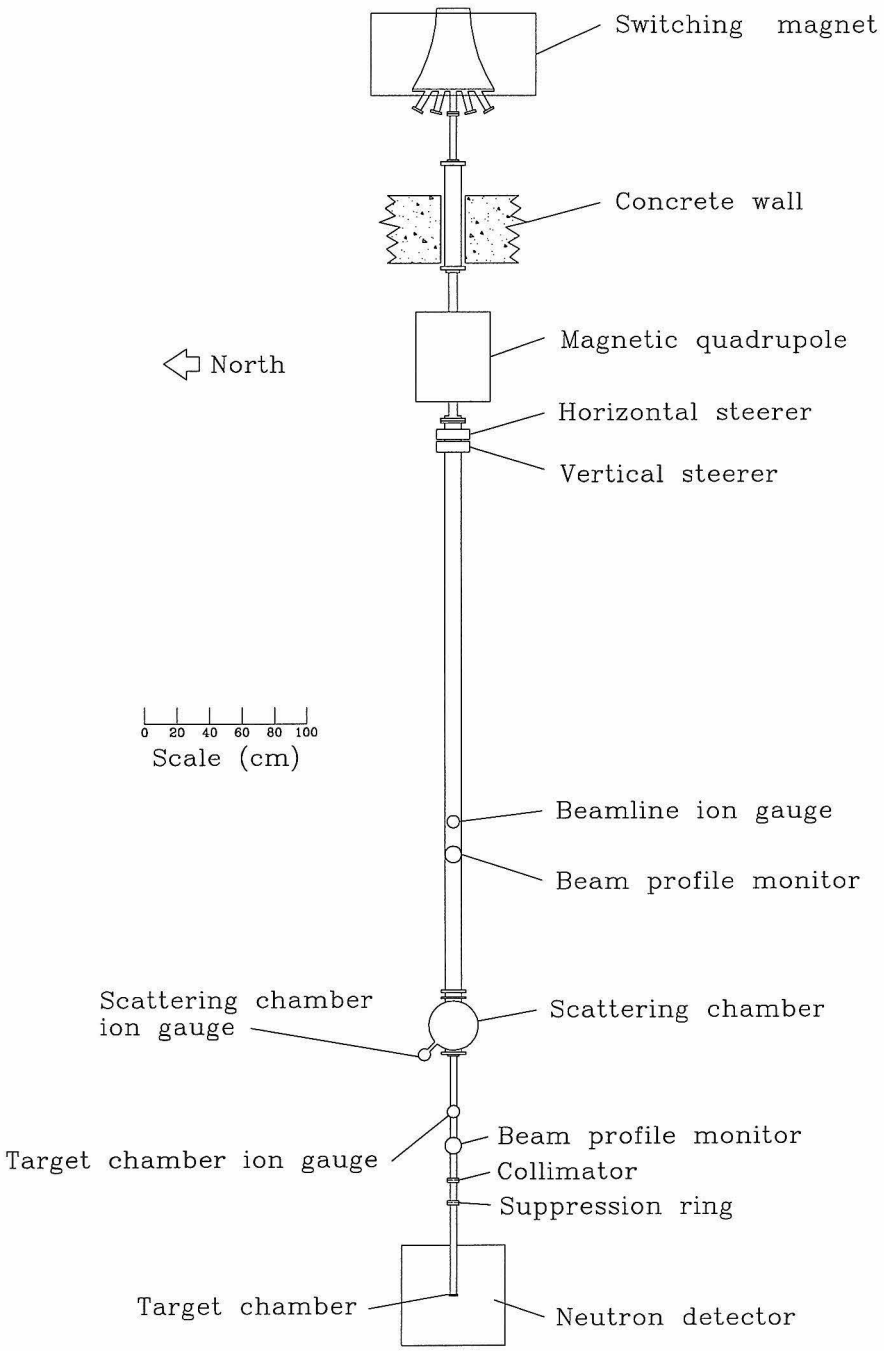

Figure 5.1: The 0° beamline. The turbopump is located directly underneath the scattering chamber. Details of the outer polyethylene and paraffin house surrounding the neutron detector are shown in Figures 6.1 and 6.2.

5.1 90° Target Chamber

The 90° target chamber, so called because the target plane is fixed perpendicular to the incident beam direction, was installed at the end of the 0° beamline, as shown in Figure 5.1. For a good vacuum seal, the target backing is fastened directly to the end of the target chamber by a circular knife-edge vacuum seal. During bombardment, the back of the target was cooled with flowing liquid Freon (1,1,2-trichloro 1,2,2-trifluoroethane). Both the target flange with the knife edge and the Freon-cooling jacket were machined from stainless steel, and the target flange was welded onto stainless steel vacuum tubing of outer diameter 3.81 cm.

This target chamber was aligned after installation by replacing the target and Freon-cooling jacket by a quartz window, and bombarding the quartz with a 100 nA proton beam. The beam-induced fluorescence in the quartz showed the image of the collimator on the target. This image was then centered by adjusting the setscrews positioning the 90° target chamber, ensuring that any beam passing through the collimator could strike only the target and not any other part of the chamber, for accurate beam integration. It was also verified that the beam hit the center of the target when the beam was positioned at the center of the collimator.

The number of incident particles striking the target was determined by beam current integration. The integrator, an ORTEC 439, serial number 428, was calibrated at the usual operating range by a known (3 μA) current source. The leakage current of the target was typically 0.2–0.4 nA. This current is due entirely to the charge carried by the Freon cooling, since it is reduced to less than 1 pA whenever the Freon pump is switched off. The charge collected for each run was corrected for the effect of this small leakage current.

5.2 Target Installation

To install a new target, the beam line was vented with dry nitrogen, and the existing target replaced by the new one. In order to pump out any water or gases that

had been adsorbed onto the walls of the target chamber while the target was being changed, heating tape was wrapped around the collimator, suppression ring, and 90° target chamber, and heated overnight. During the heating, the outside of the target chamber reached approximately 300°C.

When the heating tape was first turned on, the vacuum usually rose to above 10^{-5} torr, falling to 8×10^{-7} torr in the morning. Once the heating was turned off, the vacuum at the target chamber ion gauge was always less than 6×10^{-7} torr.

The valve connections upstream were also heated overnight but only to 75°C, due to the presence of Viton and possibly Buna O-rings, which should only be exposed to maximum optimal temperatures of 150°C and 75–85°C, respectively [OHa89].

Chapter 6 Neutron Detection

The use of moderated proportional counters as neutron detectors has a long history: in 1947, Hanson and McKibben [Han47] used paraffin-moderated BF_3 proportional counters to detect neutrons, and in 1949 Walker [Wal49] used BF_3 tubes with a graphite moderator in order to measure (α, n) cross sections. However, it wasn't until 1957 that Macklin made the first neutron detector [Mac57] in which the graphite moderator, in the shape of a sphere, completely surrounds the neutron source (hence the term "4π detector"). Shortly thereafter, in 1958, Johnson *et al.* [Joh58] made a 4π neutron detector with BF_3 counters in a cube of paraffin, and since then, a variety of moderators, such as graphite [Ske85], paraffin [Mar60], polyethylene [Kun96, Wes82], and oil [Lee80], with varying geometries, have been used for 4π detection.

4π detectors have the advantage of being high in efficiency, in comparison with other systems such as stilbene crystals, and further, do not require integration over angular distributions in order to get the total neutron yield. However, due to the thermalization of the neutrons, almost all information about original energy and angular distributions of the neutrons is lost. Some groups have placed proportional counters at varying radii from the neutron source in an attempt to retrieve some information about neutron energies [Kun96, Wes82]; others have used a spherical geometry with the counters placed radially at the zeros of the Legendre polynomials, in order to get information about angular distributions [Sek76]. Since the neutron detector used in this experiment was built to determine total cross sections, the geometry of the proportional counters was set to maximize the efficiency, rather than the amount of information about the neutron energies or angular distributions.

The advantage of using graphite as a moderator is that the efficiency does not vary rapidly with neutron energy — Macklin's calculations indicated that the efficiency is constant within 1% from 1 keV to 2 MeV. The disadvantage is that the diffusion length for neutrons is on the order of 50 cm, and thus the dimensions of the

graphite have to be quite large (on the order of 1.5 m) to get efficiencies of 10%. The scattering and diffusion lengths of hydrogen atoms are so much smaller than those of carbon that polyethylene or paraffin moderators can be much more compact than the corresponding graphite moderator for the same efficiency. However, the efficiency of a polyethylene- or paraffin-moderated detector is much more dependent on neutron energy than a graphite-moderated detector, requiring Monte Carlo calculations to model adequately the low-energy detection efficiency.

6.1 Description of Polycube

The neutron detector, hereafter referred to as the "polycube," is a 4π detector consisting of 12 ^{3}He-filled proportional counters embedded in a polyethylene moderator. The polyethylene moderator is in the form of a cube, 40 cm on a side, with an 11.5 cm $\times$ 11.0 cm channel through the center for insertion of the beampipe. The polycube is mounted on rails that allow it to be positioned around the target chamber such that the target is at the exact center of the cube. Figures 6.1 and 6.2 show the geometry of the polycube.

Surrounding the 40 cm cube of polyethylene is a 4π layer of cadmium shielding, 0.6 mm thick, which is in turn surrounded by a 4π passive layer of polyethylene and borated paraffin, approximately 10 cm thick, and a 3π passive paraffin wax "house," 25–50 cm thick. The polycube is further located beneath 2.0 meters of concrete and soil at an elevation of 230 meters above sea level [Kel91].

The 12 ^{3}He proportional counters are positioned about the beampipe channel in an ellipse whose vertical semimajor axis is 13.2 cm long, and horizontal semiminor axis is 11.1 cm long, as shown in Figure 6.1. Each proportional counter is 2.5 cm in diameter and 54 cm long, with an active length of 46 cm. The counters are manufactured by Reuter-Stokes, model number RS-P4-0818-202. They are essentially grounded stainless-steel tubes filled with ^{3}He at a pressure of four atmospheres, with an electrically-isolated high-voltage wire running down the axis of the tube. Neutrons which enter the polycube are thermalized in the polyethylene, and then captured in

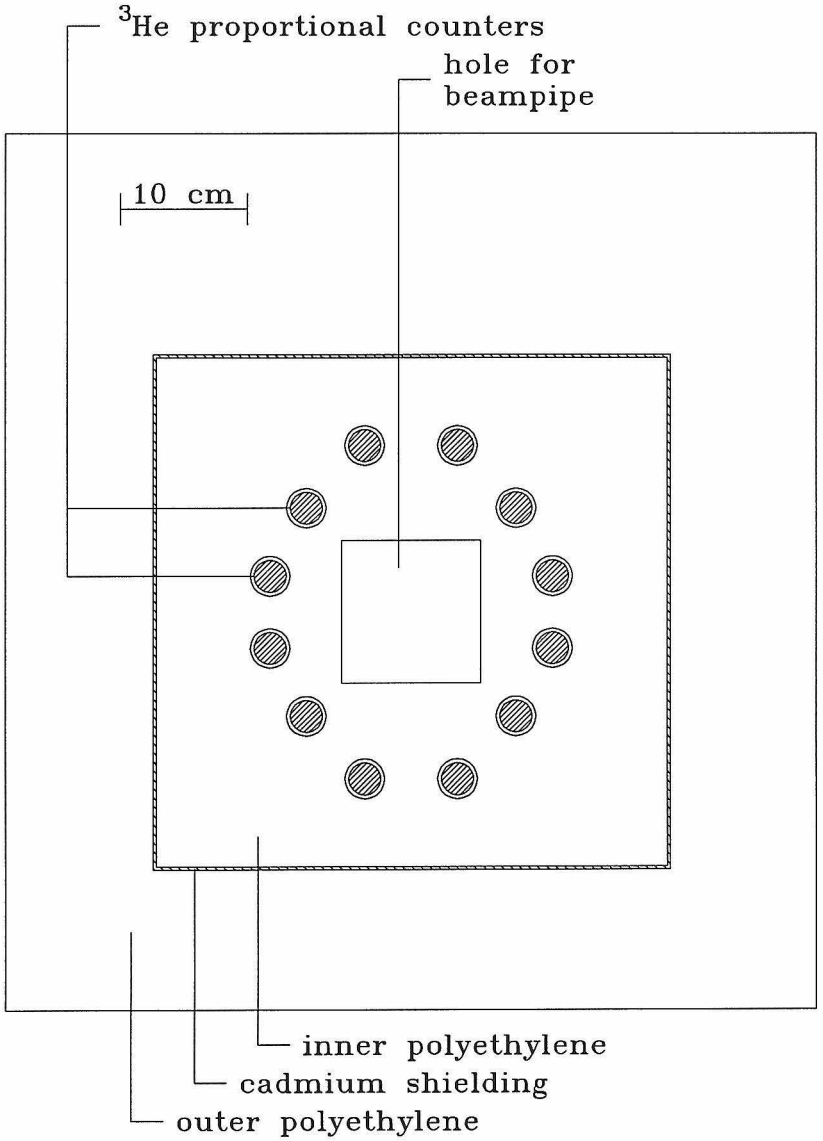

Figure 6.1: Front view of the polycube.

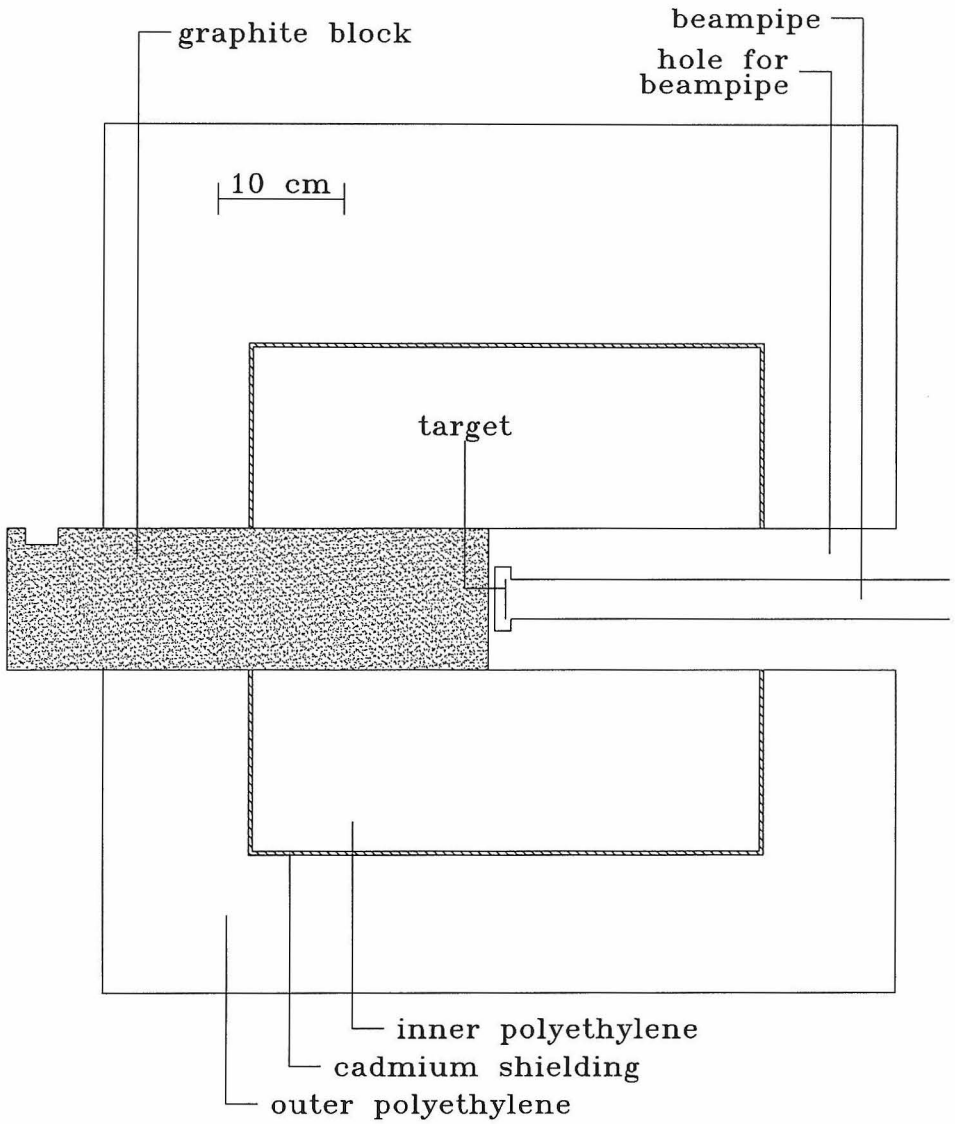

Figure 6.2: Side view of the polycube, including the 90° target chamber and the graphite block. Positions of the proportional counters and details of the target chamber and Freon-cooling system are not shown.

the proportional counters by the $^3\mathrm{He}(n,p)^3\mathrm{H}$ reaction (Q= 764 keV, σ_{th}=5300 b). The charged products from this reaction create showers of electrons which are accelerated to the positive voltage (1752 V) on the central wire. This voltage must be high enough that the electrons gain enough energy between collisions to liberate other electrons, causing amplification of the signal, yet low enough that the avalanche does not saturate and the charge collected is still proportional to the original number of ion pairs, and hence the energy, produced by the nuclear reaction.

The high-voltage line in each proportional counter is monitored by a preamplifier, which provides impedance matching and amplification to the charge pulse on the high-voltage wire caused by these cascading electrons. Each preamplifier delivers its signal to a priority encoder. The priority encoder first amplifies the signal, then compares it to an adjustable threshold, different for each proportional counter. If the signal exceeds this threshold, a pulse is generated which has a height roughly proportional to the number (1–12) assigned to each counter. The output of the priority encoder, therefore, is a series of 12 peaks, with each peak containing the number of pulses generated by the corresponding counter. This output is amplified and sent to a scaler to determine the total yield of neutrons. The output spectrum is also examined periodically in a Tracor-Northern TN-7200 multi-channel analyzer to check for any asymmetries in the number of counts per counter.

Figure 6.3 shows a typical pulse-height spectrum output by a preamplifier. The peak corresponds to the deposition of the full Q-value (764 keV) from the recoiling proton and triton from the $^3\mathrm{He}(n,p)^3\mathrm{H}$ reaction. Since the neutrons are thermalized, the resultant proton and triton come out back-to-back in the laboratory frame, with the proton carrying $\frac{3}{4}$ and the triton $\frac{1}{4}$ of the reaction energy. Should the reaction occur near the wall of the counter, one of the recoiling particles may deposit some or all of its energy in the wall, with a maximum loss when the particle in question is the proton. This leads to the low energy plateau in the spectrum which extends down to $\frac{1}{4}$ of the peak pulse height. The counts below the threshold in the figure are due to electronic noise.

The threshold for each proportional counter is set so as to maximize the signal

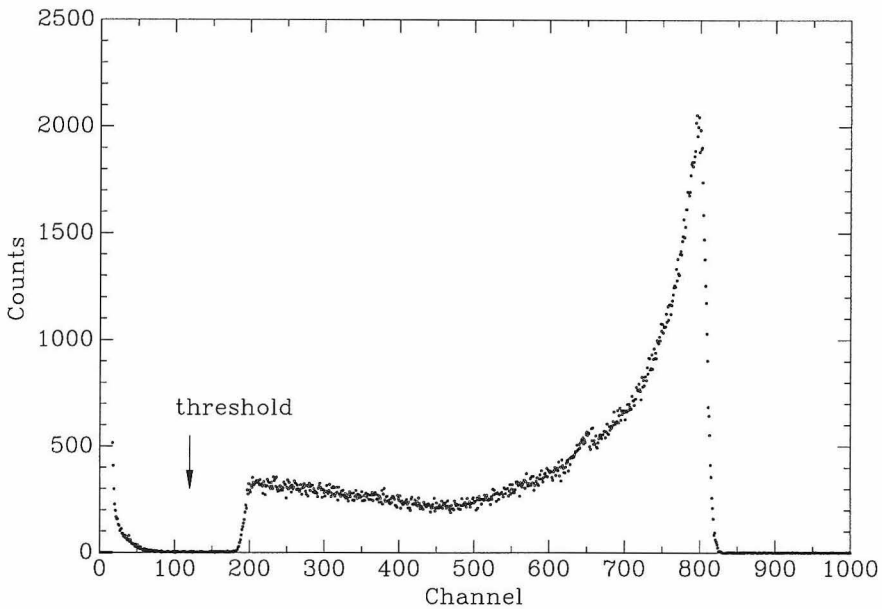

Figure 6.3: A typical pulse-height spectrum from a ^{3}He proportional counter, generated by counting the weak AmBe source (placed in the center of the cube) for 1000.0 s. Events below the threshold are discarded by the priority encoder.

while minimizing counts due to the electronic noise. Clearly, the way to minimize the noise would be to set the threshold right at the end of the low energy plateau; however, any slight downward shift in gain might lead to counts due to neutrons being discarded. Therefore, the threshold is set in the center of the trough between the noise peak and the neutron signal, as shown in Figures 6.3 and 6.4. Experimentally, the threshold is set to $\frac{3}{4}$ of the voltage needed to just barely cut off the lower end of the neutron pulse-height spectrum.

6.2 Background

Figure 6.4 shows a typical background spectrum from one of the ^{3}He proportional counters. In addition to the neutron spectrum expected from the neutrons created by cosmic ray bombardment, the spectrum contains a tail from the electronic noise at low energies and also a continuum extending over 4 MeV. This continuum is most likely due to alpha-emission from traces of uranium and thorium in the stainless

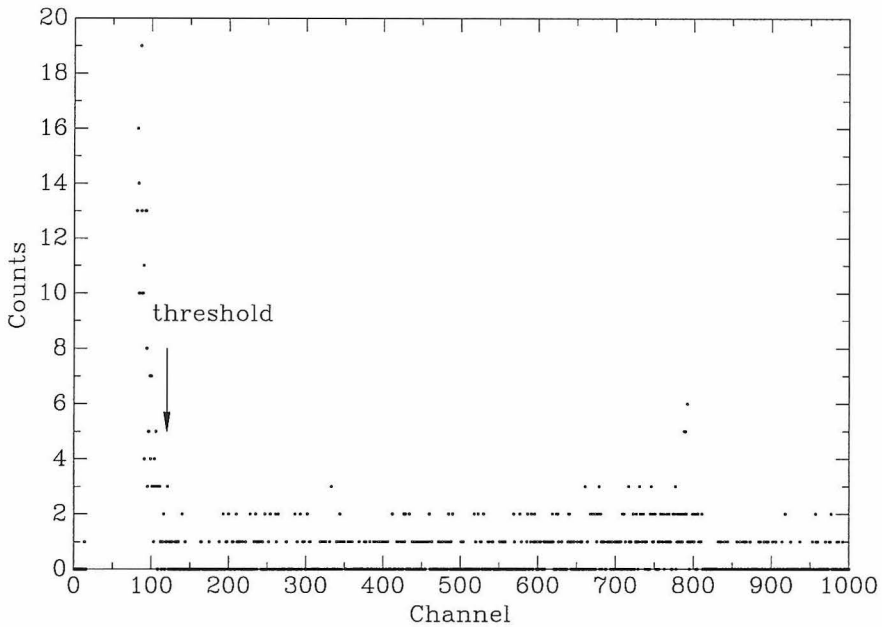

Figure 6.4: Typical background spectrum from one of the ^{3}He proportional counters, generated by counting for 10000.0 s. Events below the threshold are discarded by the priority encoder.

steel walls of each proportional counter. The measured count rate of the detector from this background is typically between 0.12 and 0.16 counts/s, and as my usual experimental count rate is between 500 to 1000 counts/s, this background makes a negligible contribution to the experimental yield.

6.3 Deadtime

Previous work [Kel91] has shown that the polycube is non-paralyzable, *i.e.,* the arrival of a second event during a dead time period does not extend this period of dead time. Therefore, the relationship between the measured count rate c and the measured yield y is [Leo87]

$$y = m(1 - c\tau) \; , \tag{6.1}$$

where τ is the dead time, and m is the true yield. Therefore, a plot of y versus c will be linear, with a slope of $-m\tau$ and a y-intercept of m. This deadtime was

measured experimentally for the polycube using the ^{7}Li(p,n) reaction: a ^{7}Li target was bombarded with increasing beam currents of protons, while measuring both the yield (in counts/μC) and count rate (in counts/s). The extracted deadtime was found to be 1.99(9) μs for 12 tubes. As expected, this result falls between the deadtime between successive pulses in different preamps (1.5 μs) and that of successive pulses in the same preamp ($4 - 8$ μs) [Kel91].

6.4 Monte Carlo Simulations with MCNP

Because the efficiency of the neutron detector is dependent on neutron energy, Monte Carlo calculations were required to model the low energy behavior of the polycube, and determine the detection efficiency as a function of neutron energy. The code MCNP (Monte Carlo N-Particle) [Bri93] was chosen since it is the most extensive code for Monte Carlo neutron transport available.

6.4.1 Overview of MCNP

As quoted from Hendricks and Briesmeister [Hen92], "MCNP is a general purpose Monte Carlo code for calculating the time-dependent continuous-energy transport of neutrons, photons, and/or electrons in three-dimensional geometries." It is used for such applications as reactor design, radiation shielding, accelerator target design, medical physics and radiotherapy, and detector design and analysis. In particular, MCNP has been used to model 4π neutron detectors [Kun96, Hsu94, Mar94, Mar91], with good results from those groups with experimental tests of the MCNP simulations. The code is distributed for Los Alamos by the Radiation Safety Information Computational Center (RSICC) in Oak Ridge, Tennessee, and is continually being updated.

6.4.2 Installation of MCNP

MCNP is written in ANSI standard FORTRAN 77 for compatability with many different computer systems. The version of MCNP used in this work was version 4A, with a patch

supplied by RSICC in order to install the code on a DEC Alpha running OSF/1. The installation was tested by running the 25 test problems included with the package: the output from these test problems had no significant differences in the output from that expected; the only minor changes were due to the differences in the arithmetic processor and different running times on the DEC Alpha.

The neutron physics models employed by MCNP require data libraries that contain cross section and reaction information. The data libraries used for this work were from the ENDF/B-VI compilation [Car93] containing the most up-to-date cross sections for more than one hundred isotopes in the energy range 10^{-5} eV to 20 MeV. This compilation is processed using the NJOY code [Mac82] into a format readable by MCNP, and the resulting libraries, called MCNPDAT6, are supplied with the MCNP package by RSICC. For this work, I used the continuous libraries, in which the cross sections are treated as continuous in energy with linear interpolation between specific energies such that the original evaluations are reproduced within 1%. Unfortunately, the cross sections for cadmium were not included in the MCNPDAT6 libraries, so I used the cross sections from ENDF/B-V instead. The selection of the data libraries was not critical, however, since there were no significant changes in the output generated from either the ENDF/B-VI or ENDF/B-V libraries.

MCNP uses the $S(\alpha, \beta)$ scattering model, including the effects of both chemical binding and crystalline structure, to model the thermal neutron scattering. Libraries of $S(\alpha, \beta)$ data for both graphite and polyethylene at room temperature were included in the MCNP package and were used in the simulations for this work.

As well as offering a wide selection of built-in neutron sources, MCNP allows the user to include a subroutine which generates the energy, starting position, and direction for the initial neutrons from the source. As MCNP is not set up to model the relativistic kinematics of a nuclear reaction, I wrote a subroutine that calculated neutron energies and laboratory angles for a given nuclear reaction and beam energy. The formulae used to calculate the relativistic kinematic quantities are detailed in Section 2.2. Nuclear masses were taken from the compilation of Audi and Wapstra [Aud95]. For those reactions with known angular distributions, $^{7}\mathrm{Li}(p, n)^{7}\mathrm{Be}$ and $t(d, n)^{4}\mathrm{He}$, the

angular distribution tables from the compilation of Drosg and Schwerer [Dro87] were input. All other reactions were assumed to be isotropic in the center of mass frame.

6.4.3 Input Files and Detector Geometry

The detector is completely modeled in the user-specified input file. MCNP allows three-dimensional volumes or cells to be defined in a Cartesian coordinate system. These cells each contain one material at a specified density, and are built up by using Boolean operators to combine basic volumes bounded by simple surfaces. Where possible, the dimensions and densities of each material comprising the detector were measured directly, including the densities of polyethylene and graphite. GE Reuter-Stokes, the manufacturers of the ^{3}He proportional counters, supplied the specifications for these tubes, as shown in Figure 6.5. The pressure of the ^{3}He in the proportional counters was taken to be 4 atm, as per the manufacturer's specifications. No attempt was made to model any differences between individual tubes (whose outputs vary by up to 4%) since the goal was to determine the efficiency of the sum of the 12 tubes.

Those simulations involving a fixed target producing neutrons from an induced nuclear reaction also included the complete geometry of the beampipe, target, and Freon- or water-cooling system. For these measurements, a graphite block was inserted into the beampipe hole, as shown in Figure 6.2, to intercept those neutrons leaving the target at small forward angles, and this block also was included in the simulation.

When first setting up the input file for the polycube, I allowed the dimensions of each material to vary to determine which were critical to model the detector accurately. Fortunately, the critical measurements are all well known: the density of the ^{3}He inside the tubes, the active volumes of the tubes, the dimensions of the inner cube of polyethylene, and the dimensions of the hole for the beampipe and the various other air gaps in the inner polyethylene. Dimensions which are not critical include the exact thickness of the cadmium shielding, the dimensions of the outer polyethylene, and whether the inactive volumes of the proportional counters are filled with ^{3}He or

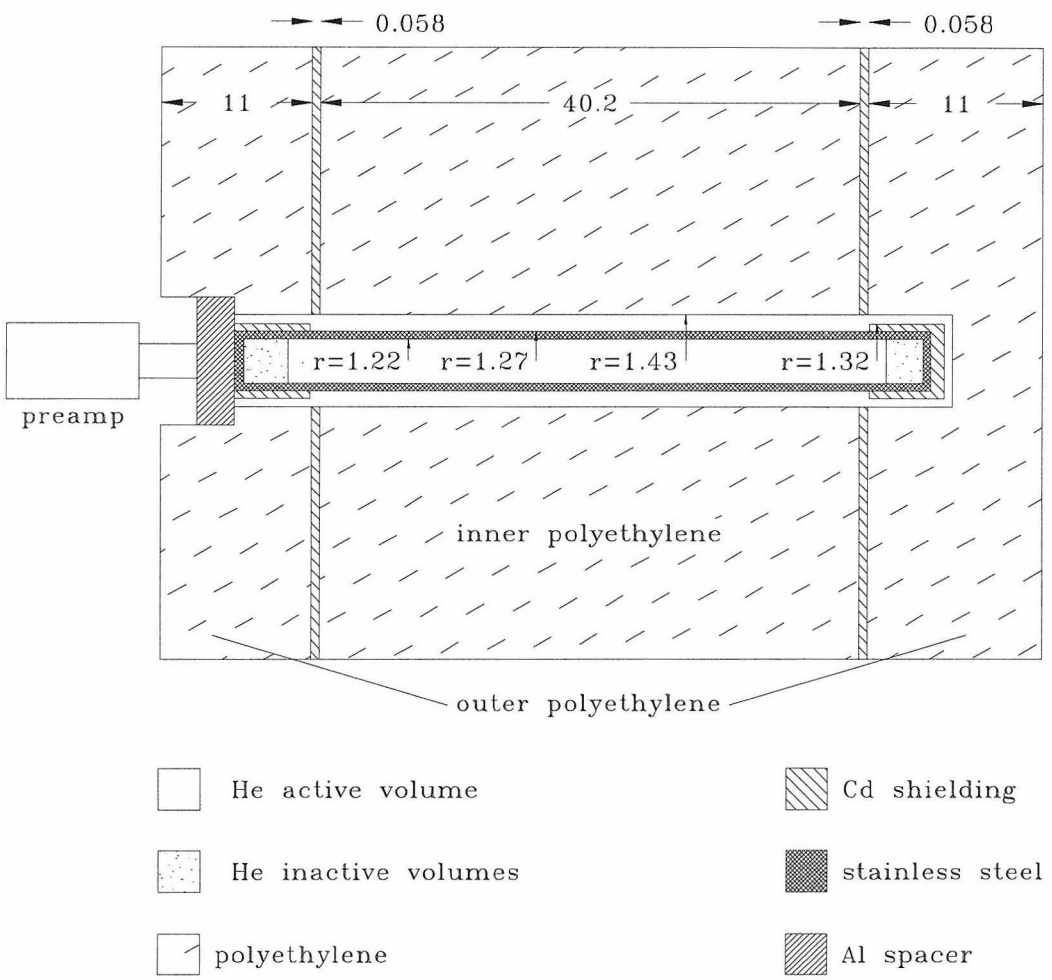

Figure 6.5: Diagram of the specifications of the ^{3}He proportional counters and the geometry of the surrounding materials. All measurements shown in cm. Not to scale.

	10 keV	100 keV	1 MeV	10 MeV
captured by ^{3}He(n,p)	20.8	23.0	22.6	8.9
captured by inner polyethylene cube	56.1	56.0	54.2	26.6
captured by Cd(n,γ)	6.3	6.5	9.9	13.4
captured by outer polyethylene layer	3.0	2.9	3.8	16.6
captured by stainless steel (n,γ)	0.9	1.0	1.0	0.4
escape	8.1	7.4	6.3	23.2
other	4.8	3.2	2.2	10.9

Table 6.1: Fate of neutrons in the polycube. Each column shows the percentage of neutrons either escaping the polycube or captured by a particular material within the cube for a source of monoenergetic, isotropic neutrons. The ^{3}He specified above is the ^{3}He in the active volumes of the counters, and the stainless steel is the steel of the proportional counter casing. The neutrons captured by the inactive volumes of ^{3}He, the graphite block, and the materials of the beampipe (*i.e.,* the stainless steel, Freon cooling, and Cu target backing) are included in "other."

304 stainless steel. As the detector efficiency was not highly dependent on the exact dimensions of the outer layers of polyethylene, it was extremely unlikely that any neutrons that made it outside this polyethylene layer would be reflected back inside the cube, and therefore the geometry of the paraffin "house" surrounding the cube was not included.

Simulations were run to determine whether the neutrons not captured by the ^{3}He escaped from the cube or were captured by other materials in the polycube. Table 6.1 shows the results of these simulations. Clearly the dominant factors are the capture of neutrons by the inner polyethylene cube and the active volumes of ^{3}He, which support the results of the simulations determining the critical dimensions of the polycube.

`MCNP` allows the geometry of the input files to be checked by a "voiding" procedure: all nuclear physics reactions are "turned off" and the neutrons allowed to propagate through the simulation geometry to see if any get lost either in gaps in the geometry (*i.e.,* a region without a specified material) or an area where two cells overlap. All input files were checked using this procedure and found to contain no voids, and were also examined using `MCNP`'s plotting package.

6.4.4 MCNP Output

The results from MCNP are in the form of tallies: MCNP tracks specified particles through the input geometry by sampling possible random walks and then from these tally histories, computes a score of user-specified quantities. For this work, the tally which calculates the number of (n, p) reactions in the cells containing ^{3}He was calculated, and as the standard MCNP tallies are normalized to one starting particle, this tally by definition equals the efficiency for the detector.

The final tally calculated by MCNP then represents an average of the contributions from the many histories sampled during the simulation. To ensure that the statistical error associated with the tally represents the true confidence interval, MCNP calculates several quantities that monitor the behavior of the tally and ensure that it converges toward the final result.

One such quantity is the relative error R. Let x_i be the tally for the ith history, $\bar{x}$ be the mean of these tallies, and N be the total number of histories run. The relative error R for the mean $\bar{x}$ is then given by

$$R(\bar{x}) \equiv \frac{s_{\bar{x}}}{\bar{x}} , \tag{6.2}$$

where $s_{\bar{x}}$ is the variance of the mean,

$$s_{\bar{x}}^2 = \frac{\Sigma(x_i - \bar{x})^2}{N(N-1)} . \tag{6.3}$$

It is recommended that the relative error be less than 0.10 for reliable confidence intervals to be generated. For most runs, either 100,000 or 400,000 events were generated, and the resulting R in all instances was much less than 0.01.

Another such quantity is the figure of merit FOM. As the computer time T needed for a simulation should be directly proportional to N while the relative error R should be proportional to $\frac{1}{\sqrt{N}}$, the figure of merit, defined as

$$FOM \equiv \frac{1}{R^2 T} , \tag{6.4}$$

should be approximately constant during the simulation.

MCNP makes a total of ten statistical checks on each tally run during the simulation, such as checking that fluctuations in the mean be random over time, that the relative error be both less than 0.10 and have a decrease rate of approximately $\frac{1}{\sqrt{N}}$, and that the figure of merit be roughly constant throughout the last half of the simulation. Only simulations which passed these ten statistical checks were used in this work.

MCNP also allows a choice of variance reduction techniques: certain cutoff values for time, lower neutron energy, and neutron weights may be chosen to minimize computation times. I employed a neutron energy cutoff of 10^{-5} eV, to determine whether the lower energy range of the cross section libraries was too high, but as typically only 20 of 100,000 neutrons were thermalized to below 10^{-5} eV before capture or escape, I deemed the energy range sufficient. Otherwise, no other variance reduction techniques were employed: only the program default values written into MCNP were used.

6.4.5 Validation of MCNP Efficiencies

Two stationary sources and two nuclear reactions were used to test the results from MCNP. The quoted errors in the MCNP results are the variances in the histories $s_{\bar{x}}$ (*i.e.*, purely statistical errors), and do not include any overall normalization uncertainties.

The ^{252}Cf source

The ^{252}Cf source, manufactured by Isotope Products Laboratories, serial number C418, is a "point" source encased in a 304 stainless steel cylinder which is pointed at one end. The center of the source was determined to be 5.4(5) mm from the pointed end by slit-scanning it with a GeLi detector to determine the position of the source of γ-rays emanating from a small isotopic contamination of ^{249}Cf.

The strength was determined to within 3% in 1978 by comparison with a ^{252}Cf source whose calibration is traceable to the National Institute of Standards and Technology (NIST). Since this time, the amount of ^{250}Cf ($t_{1/2}$ = 13.08 years), originally

negligible, has become important, yielding 8.3(6)% of the neutrons on April 2,1997. (The assertion that the Cf in this source is not pure ^{252}Cf is established by my observation of 388.2- and 333.4-keV γ rays from the source, which are found in the decay of ^{249}Cf to its daughter, ^{245}Cm [Fir96].) The amount of ^{250}Cf was measured by tracing the decay curve of the measured neutron yield for the polycube from 1989 to 1997, and fitting this curve to the decays of the two isotopes present. The original fraction of the neutron yield coming from the ^{250}Cf from this analysis was $1.91(14) \times 10^{-3}$, and the source strength on April 2, 1997 was 260(7) neutrons/s. With this information incorporated into the source strength, the measured efficiency of the neutron detector for the ^{252}Cf source was 0.196(6). This efficiency was measured with the source taped to the beampipe and the graphite block in place, for 11 of the 12 tubes active.

Although the ^{252}Cf source has multiple neutrons per fission which are emitted simultaneously, the mean lifetime of a neutron in the polycube (78 μs) [Kel91] is sufficiently large with respect to the detector deadtime (2 μs) that the loss of counts due to this effect was neglected.

The distribution of neutron energies used by `MCNP` to model the ^{252}Cf spectrum was a Watt spectrum with $T_W = 1.175$ MeV and $E_W = 0.359$ MeV [Fro90]. The mean neutron energy from a ^{252}Cf source is 2.35 MeV. The rejection method, described by Press et al. [Pre86], was used to generate the neutron energies from the given spectrum more efficiently. The geometry of the source capsule was also included in the simulation, and the resulting `MCNP` efficiency was 0.1927(15), which shows excellent agreement with the experimental value.

The AmBe source

Two ^{241}Am-Be neutron sources were used in the calibration of the polycube, a 1 Ci ^{241}Am-Be source and a 10 mCi source. These sources are both in the form of a pellet, which contains the amount of ^{241}AmO necessary for the desired activity, distributed in 4.62 g of metallic Be for the strong source and 2.10 g for the weak source. This mixture is compacted in a press into a cylindrical capsule, then encased in a double-walled stainless steel capsule (Amersham X.3 and X.2 capsules for the strong and

weak source, respectively). The fact that there is a large amount of beryllium present in the capsules influences the energy spectrum of the neutrons: the $^{9}\mathrm{Be}(n, 2n)$ reaction causes the number of neutrons originally generated by the $^{9}\mathrm{Be}(\alpha, n)^{12}\mathrm{C}$ reaction to multiply, and the neutrons generated by $^{9}\mathrm{Be}(n, 2n)$ are also lower in energy than the original neutron.

The 1 Ci source had been calibrated by NIST to within 1.7% (2.75×10^{6} n/s on March 12, 1993), which is too strong to be measured directly in the center of the cube. A comparison was therefore made between the 1 Ci source and the 10 mCi source to determine the strength of the latter. If the two sources had been constructed with the same amount of beryllium, the comparison would have been very straightforward; however, the spectrum of the outgoing neutrons is dependent on the amount of Be in the pellet as described above, and so `MCNP` was used to model the efficiency of the cube for the two sources in the comparison geometry. To get the measured count rate for the strong source to be less than 10,000 counts/s, the front face of polyethylene was taken off the polycube and all but one proportional counter removed. Each source was then placed in an empty hole roughly opposite this counter and the count rate measured. The strength of the weak source from this comparison was found to be $2.57(9) \times 10^{3}$ neutrons/s on March 20, 1997. The weak source was then placed in the center of the polycube in the usual counting geometry, and the efficiency of the cube was found to be 0.155(6).

The spectrum of AmBe neutron energies for the `MCNP` simulation was generated from the spectrum of Geiger and van der Zwan [Gei75]. This spectrum is calculated from the distribution of α-particles from $^{241}\mathrm{Am}$ and the cross section of the $^{9}\mathrm{Be}(\alpha, n)^{12}\mathrm{C}$ reaction, and has an uncertainty of $\pm 5\%$ for neutrons above 2.5 MeV in energy, rising to $\pm 10\%$ for neutrons below 2 MeV. The mean energy of AmBe neutrons with this spectrum is 4.46 MeV. This spectrum does not include the effects of the $^{9}\mathrm{Be}(n, 2n)$ reaction, which is important for sources like this one which has large excess of beryllium. The geometry of the source capsule, namely that of the beryllium and the stainless steel capsule, was therefore input into `MCNP`, to incorporate the effect of $^{9}\mathrm{Be}(n, 2n)$ reaction in the simulation. (Simulations run without the

beryllium present resulted in efficiencies on the order of 4% lower than efficiencies calculated with the effects of the beryllium.) Since the efficiency desired was the efficiency for the number of neutrons coming from the AmBe source (the total number of neutrons generated by both the $^9\mathrm{Be}(\alpha, n)^{12}\mathrm{C}$ and the $^9\mathrm{Be}(n, 2n)$ reactions), the tally of $^3\mathrm{He}(n, p)$ reactions output by MCNP was corrected by the calculated multiplicity of neutrons. The MCNP efficiency for the weak source was found to be 0.1500(14), and this is within the 1σ error for the measured efficiency of 0.155(6).

The $t(d, n)^4$He reaction

A tritium target of known thickness [Bru94] was made and the efficiency for six tubes measured for a beam energy of $\sim$ 96 keV (and a consequent average neutron energy of $\sim$ 14.1 MeV). From the known reaction yield [Dro87], the efficiency was found to be 0.0468(14). The MCNP efficiency was 0.0481(2), and the two show good agreement.

The $^7\mathrm{Li}(p, n)^7$Be reaction

Because of the difficulty in determining the thickness of ^{7}Li targets, no attempt was made to determine the absolute efficiency of the cube for the $^7\mathrm{Li}(p, n)^7\mathrm{Be}$ reaction. However, since the efficiency of the polycube varies highly for low energy neutrons, as shown in Section 6.4.6, the efficiency for neutrons from the $^7\mathrm{Li}(p, n)^7\mathrm{Be}$ reaction will change from 0.214(16) at threshold to 0.238(17) at 2.1 MeV, an 11% difference, and thus the excitation function (yield *vs.* energy curve) will not be simply proportional to the cross section curve. I therefore measured the excitation function for a thin LiF target to see if the MCNP results could reproduce the shape of the cross section curve from the excitation function: for a thin target, the yield is given by equation 2.22 and thus when the yield is divided by the efficiency, the result should be proportional to the cross section.

This analysis was done for my thin target data, and the result is shown in Figure 6.6. The $^7\mathrm{Li}(p, n)^7\mathrm{Be}$ cross sections are the values measured by Gibbons and Macklin [Gib59], as reported in Table IV of Liskien and Paulsen [Lis75]. Since the MCNP efficiency is constant to within 4% for beam energies above 2.1 MeV, my results

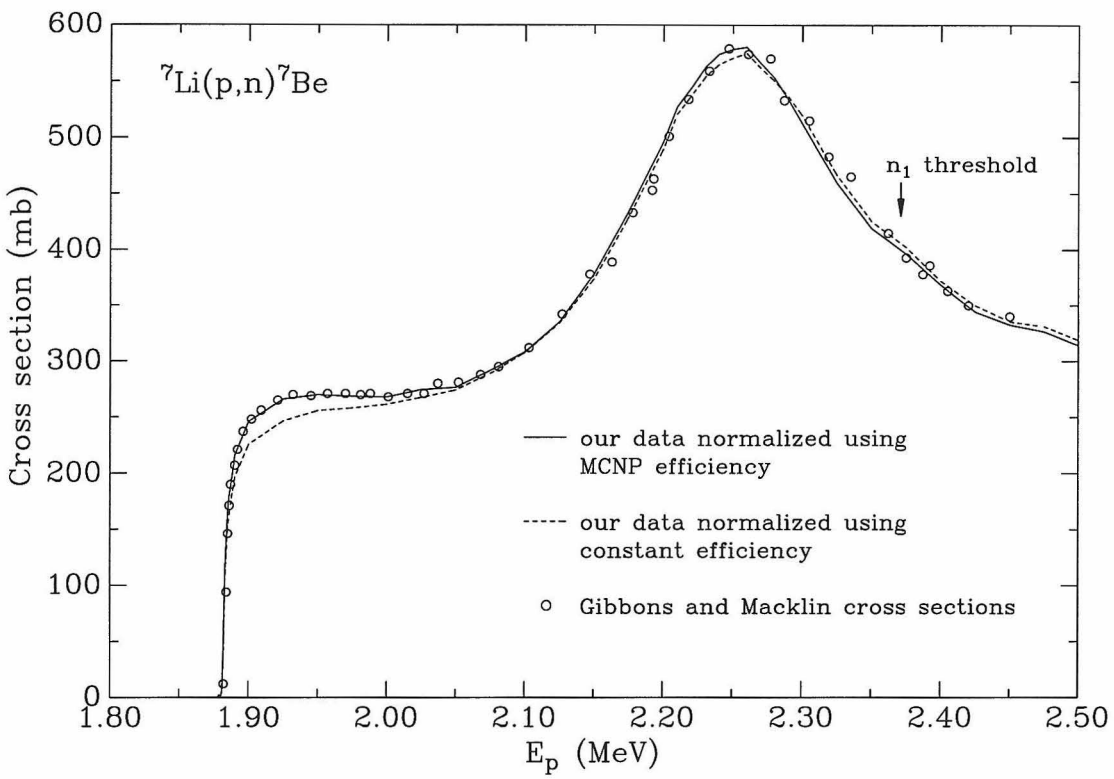

Figure 6.6: The ^{7}Li$(p,n)^7$Be yield divided by the detector efficiency *vs.*beam energy, normalized to the Gibbons and Macklin [Gib59] cross sections. Note that the shape of the cross section curve is reproduced far more accurately by the MCNP efficiency than by a constant efficiency. For readability of the graph, my data points are not shown, only the straight lines connecting the points. The statistical errors on my data points are less than 1%.

	$\overline{E}_n$ (MeV)	Experimental	MCNP	Difference
^{252}Cf	2.35	0.196(6)	0.1927(15)	1.7%
AmBe	4.46	0.155(6)	0.1500(14)	3.3%
$t(d,n)^4$He	14.1	0.0468(14)	0.0481(2)	2.8%

Table 6.2: Results of MCNP validation. The quoted error in the experimental value includes both statistical and systematic effects, while the quoted error in the MCNP results is the variance of the final tally, and does not include any normalization uncertainties. From these results, I estimate the normalization uncertainty in the MCNP efficiencies to be 3%.

were normalized such that the average deviation of my yield divided by the MCNP efficiency from the Gibbons and Macklin cross sections was zero for $E_p \geq 2.1$ MeV. My results using a constant efficiency were normalized to the same region.

As can be seen from the graph, MCNP replicates the shape of the curve quite well, with an absolute average deviation of 1.6% from the Gibbons and Macklin cross sections and a maximum deviation of 5.0%, for $E_p \geq 1.887$ MeV. For those few points below 1.887 MeV, the deviations grow much larger, but there is a large uncertainty associated with these yields (not shown in the graph), since as the cross section is dropping rapidly in this region, small changes in the beam energy will lead to large changes in the yield.

The results using a constant efficiency do not agree as well with the cross sections as those using the MCNP efficiency: below 2.1 MeV, the average deviation increases monotonically, with an average deviation of 7% for $1.90 \leq E_p \leq 1.95$ MeV.

Summary of Validation

Table 6.2 shows a summary of the MCNP validations. From these results, I estimate the overall normalization uncertainty in the MCNP efficiencies to be 3% for simulations for which either the angular distribution is known to be isotropic, or for which known angular distributions have been included in source subroutine. This uncertainty can easily be attributed to uncertainties in the MCNP input data such as the transport and reaction cross sections, and uncertainties associated with the physical

and mathematical models used during the calculation.

To determine the error associated with nuclear reactions in which the angular distribution is anisotropic but has not been measured experimentally, I examined the angular dependence of the polycube efficiency for monoenergetic neutrons. Figure 6.7 shows the results of this study. As can be seen from the figure, the efficiency for 100 keV and 1 MeV neutrons is roughly constant below 140° degrees, and as the solid angle intercepted by neutrons with an angle greater than 140° is small (for an isotropic distribution, only 10% of the neutrons have starting angles greater than 140°, and for nuclear reactions close to threshold the kinematics strongly favor small starting angles), I estimate that the uncertainty contributed by a lack of angular distributions is on the order of 3%, for a total overall normalization uncertainly on the MCNP efficiency of 4%.

6.4.6 Results of the MCNP Simulations

MCNP was then used to generate the efficiencies for a number of neutron sources and reactions.

MCNP efficiency for a monoenergetic neutron source

MCNP was used to calculate the efficiency *vs.* energy for a monoenergetic, isotropic source of neutrons, and the results are plotted in Figure 6.8. The structure in the curve above 2.0 MeV is due to resonances in the $^{12}C(n,n)$ elastic scattering cross section.

From 0.1 MeV to 1.2 MeV, the efficiency varies by 6%, which is somewhat higher than the findings of Marion *et al.* [Mar60], who claim that the efficiency of their paraffin-moderated 4π detector is constant within 3% from 0.1 keV to 1.2 MeV. This discrepancy is most likely due to the fact that the polycube has only one ring of detectors while their detector had two rings at different radii — the distance between the two rings tends to flatten the efficiency curve for their detector, as shown in Figure 3 of their article.

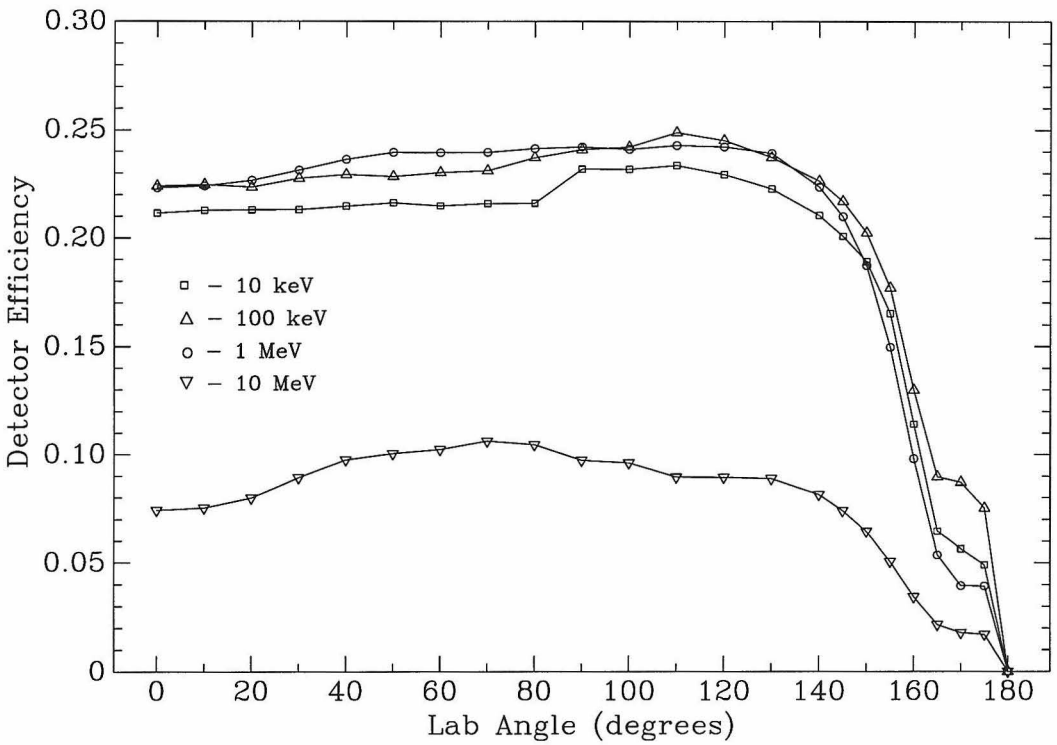

Figure 6.7: Angular dependence of the polycube efficiency for monoenergetic neutrons for a given angle θ relative to the beampipe axis. The lines connect the points in order to guide the eye. The error bars are smaller than the data points. Above 140°, the efficiency drops dramatically because the neutrons' straight-line trajectory has a progressively shorter pathlength through the inner polyethylene until at 165°, it no longer intercepts the inner polyethylene at all. Between 165° and 175°, the neutrons may still be scattered back into the inner polyethylene by the stainless steel of the beampipe, but at a greatly reduced efficiency. Above 175°, the neutrons escape the polycube entirely.

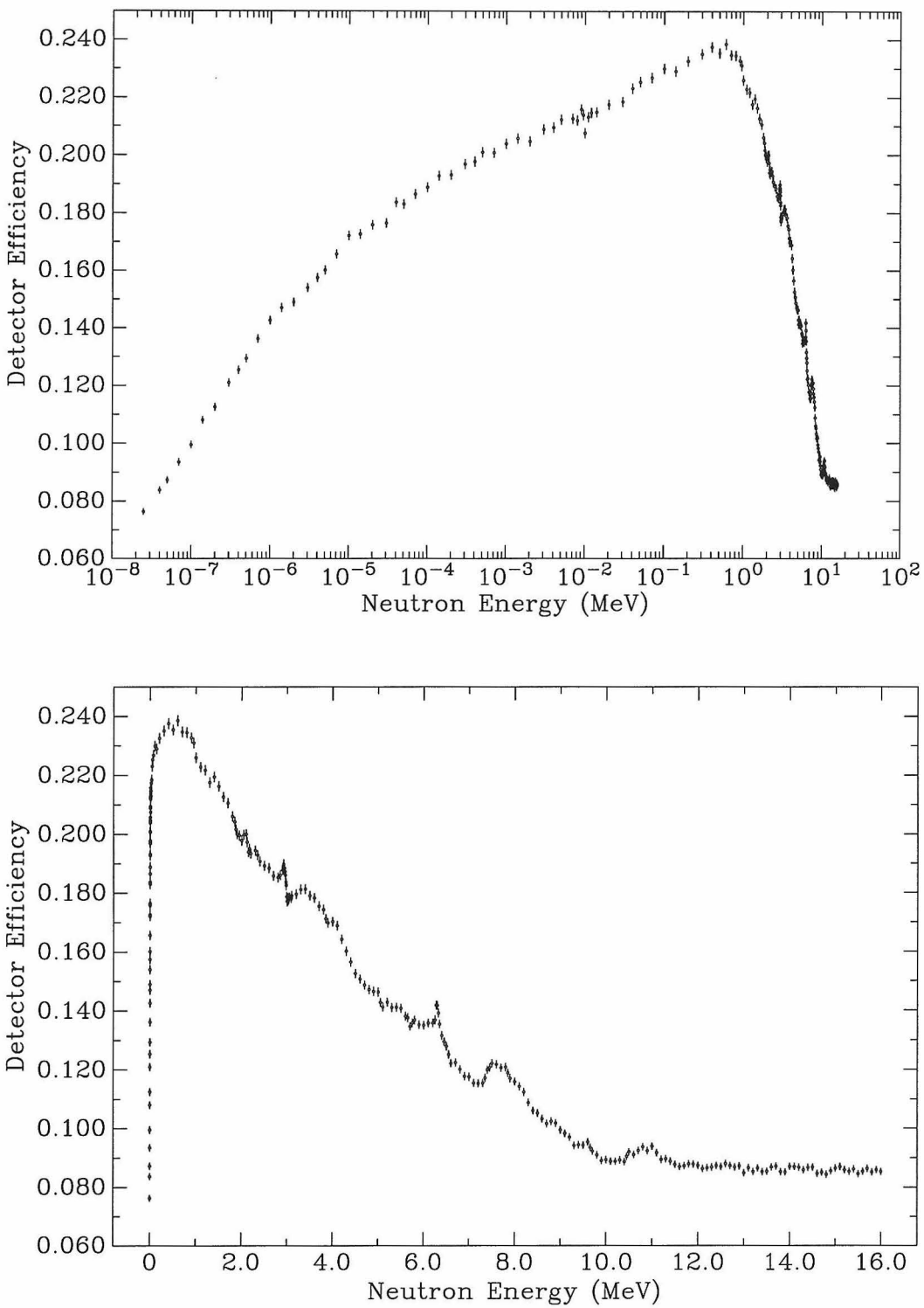

Figure 6.8: The MCNP efficiency *vs.* neutron energy for monoenergetic, isotropic neutrons. This simulation includes the geometry of the 90° target holder, the Cu target backing, and the graphite block.

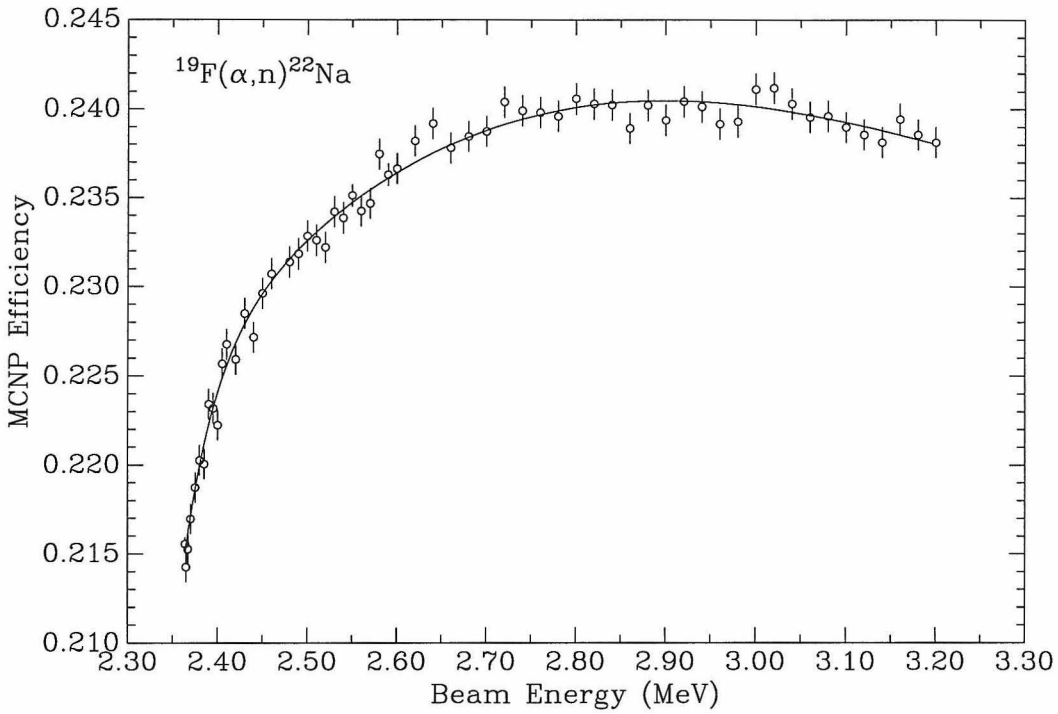

Figure 6.9: Plot of the MCNP efficiency *vs.* beam energy for the $^{19}\mathrm{F}(\alpha, n)^{22}\mathrm{Na}$ reaction. The solid curve is a fit to the data using an exponential function plus a cubic polynomial.

MCNP efficiency for $^{19}\mathrm{F}(\alpha,n)^{22}\mathrm{Na}$

MCNP was used to calculate the efficiency *vs.* bombarding energy for $^{19}\mathrm{F}(\alpha, n)^{22}\mathrm{Na}$ and the results are plotted in Figure 6.9. The solid curve is a fit to the data using an exponential function plus a cubic polynomial. This fit was used as the efficiency in all further calculations, to smooth out the effect of random fluctuations in the MCNP results.

As the n_1 threshold is at 3.07 MeV and the contribution to the neutron yield from n_1 neutrons just above that threshold is expected to be low, only the efficiencies from $^{19}\mathrm{F}(\alpha, n_0)^{22}\mathrm{Na}$ were calculated. As there are no angular distribution measurements available for $^{19}\mathrm{F}(\alpha, n)^{22}\mathrm{Na}$, the normalization uncertainty in the MCNP efficiency is 4%.

MCNP was also used to model the detection efficiency for neutrons from the reactions $^{13}\mathrm{C}(\alpha, n)^{16}\mathrm{O}$, $^{18}\mathrm{O}(\alpha, n)^{21}\mathrm{Ne}$, and $^{11}\mathrm{B}(\alpha, n)^{14}\mathrm{N}$, due to the presence of these

contaminants on the target. Since the n_1 threshold for $^{18}O(\alpha, n)^{21}Ne$ is 1.28 MeV, and there is no information about the ratio of n_1 to n_0 neutrons as a function of energy, I calculated the efficiency for both $^{18}O(\alpha, n_0)^{21}Ne$ and $^{18}O(\alpha, n_1)^{21}Ne$ and took the average. The n_1 thresholds for $^{13}C(\alpha, n)^{16}O$ and $^{11}B(\alpha, n)^{14}N$ are 5.01 and 2.94 MeV respectively, so only the n_0 efficiencies were calculated for those reactions.

MCNP efficiency for $^{22}Ne(p,n)^{22}Na$

MCNP was used to calculate the efficiency *vs.* energy for $^{22}Ne(p, n)^{22}Na$ and the results are plotted in Figure 6.10. The top plot of the figure shows the calculated efficiencies for the n_0 neutrons and the corresponding fit to the data using an exponential plus a polynomial. Because the relative contributions to the total neutron yield from the many neutron groups (n_{0-4}) are unknown, there is a large uncertainty in the efficiency above the n_1 threshold. The total neutron efficiency above the n_1 threshold was therefore chosen as an average of the efficiencies of the available neutron groups. This total neutron efficiency is shown in the bottom graph of Figure 6.10 as a solid curve, while the fits to the individual neutron groups are shown as dotted lines. The normalization uncertainty of this final efficiency is 4% below 4.6 MeV due to the lack of experimentally determined angular distributions, increasing to 6.5% at a beam energy of 5.5 MeV.

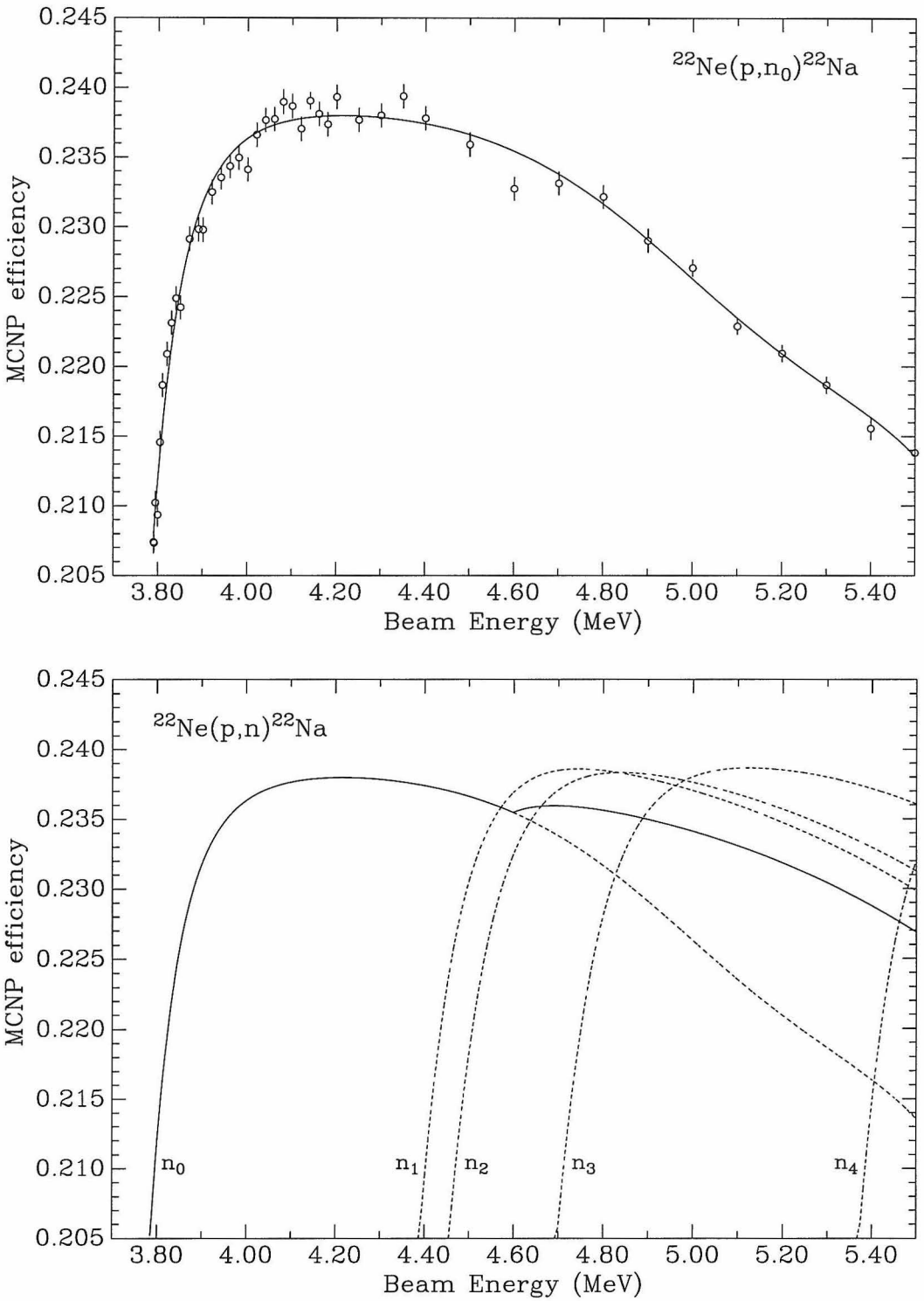

Figure 6.10: Plot of the MCNP efficiency *vs.* beam energy for the $^{22}\mathrm{Ne}(p,n)^{22}\mathrm{Na}$ reaction. The top plot shows the calculated efficiencies for the n_0 neutron group and the corresponding fit. The bottom plot shows all of the fits to the individual neutron groups as dotted lines, with the total neutron efficiency as a solid line.

Chapter 7 Gamma Ray Detection

7.1 The BGO Detector

For thickness determinations of the fluorine targets used in the $^{19}F(\alpha, n)^{22}Na$ experiment, the 6.13-MeV γ rays from the 340-keV resonance in $^{19}F(p, \alpha\gamma)^{16}O$ were detected using a BGO detector (manufactured by Bicron, model 2M2BGO/2, serial number AK-533) with a fitted preamplifier (model P-14, serial number AI-582). The signals were then fed to an ORTEC 571 amplifier and stored in a Tracor Northern TN-7200 multichannel analyzer.

For all of the $^{19}F(p, \alpha\gamma)^{16}O$ measurements, the targets were mounted on the 0° beamline, with the same collimation and suppression geometry as described in Chapter 5. The BGO detector was then placed downstream from the target, coaxially with the target and beampipe. When measuring the target yield from the 340-keV resonance in $^{19}F(p, \alpha\gamma)^{16}O$, the front face of the metal casing surrounding the BGO was placed 10.2 cm from the target; in this geometry, the efficiency of the detector is 0.0061(4) for the spectral region from 4 to 6.5 MeV [Hah95].

For the $^{22}Ne(p, \gamma)^{23}Na$ measurements, for which only relative yields were desired, the face of the casing surrounding the BGO was placed 3.37 cm from the target. In all other respects, the same geometry was used as for the $^{19}F(p, \alpha\gamma)^{16}O$ measurements.

7.2 The Ge Detector

For the thickness determination of the thicker ^{22}Ne implanted target used in the $^{22}Ne(p, n)^{22}Na$ experiment, the 440-keV γ rays from $^{22}Ne(p, \gamma)^{23}Na$ were detected using a Ge detector (manufactured by ORTEC, model GLP 36360/13, serial number 26-E101). The signals were then stored in a Tracor Northern TN-7200 multichannel analyzer.

For this thickness measurement, the target was mounted on the 0° beamline with the same collimation and suppression geometry as described in Chapter 5. The Ge detector was placed downstream at 55° with respect to the beampipe. The distance between the front face of the casing surrounding the Ge was placed $\sim$ 3.8 cm from the target. The detector efficiency was calibrated by replacing the target with a ^{152}Eu source in the same geometry. The ^{152}Eu source strength is known to 3% and is traceable to NIST; the efficiency of the detector with this geometry was found to be 0.00120(4) for the 444.0-keV γ rays from ^{152}Eu. Since the two γ rays of interest are so similar in energy (440 keV for the ^{22}Ne$(p,\gamma)^{23}$Na reaction and 444.0 keV for the ^{152}Eu source), no correction was made for this minor change in energy.

Part III

$^{19}\mathrm{F}(\alpha, n)^{22}\mathrm{Na}$

Chapter 8 Experimental Procedures

8.1 Target Preparation

Previous experiments measuring the $^{19}F(\alpha, n)^{22}Na$ cross section used targets of various fluorides, CaF_2, PbF_2 and SrF_2, evaporated onto target backings. I chose to use CaF_2 as my target material (because of the comparatively low atomic number, and consequently low stopping power, of Ca with respect to Pb or Sr), with a Cu backing, with a desired target thickness of 5-10 keV for the target used to scan the entire range of the excitation function. In order to minimize the background, a target low in both carbon and oxygen was desired, due to the large $^{13}C(\alpha, n)^{16}O$ and $^{18}O(\alpha, n)^{21}Ne$ cross sections.

The first targets for this experiment were made using a conventional evaporator with an oil diffusion pump. However, the residual oil in the vacuum from the pump left an unacceptable amount of carbon on the target ($> 10^{14}$ ^{13}C atoms/cm^2), and it was clear that another method of target preparation was needed.

The apparatus constructed by Brune and Kavanagh to make tritium targets [Bru94] was then used. A diagram of the apparatus is shown in Figure 8.1. Essentially, the apparatus consists of a quartz tube which is held under vacuum by an ion pump. The evaporation boat and the target backing are held in place by cylindrical quartz pieces slightly smaller in diameter than the tube, as shown in the figure. These inner quartz pieces have holes ground through them in order to increase the pumping speed. The evaporation boat and target backing may be heated using a 3-turn RF induction heater centered on either the boat or target backing.

The evaporation boat was made from Ta, and the shape of the boat is designed, as shown in Figure 8.2, such that the hemispherical dimple is positioned in the center of the quartz tube, and that this dimple becomes the hottest point on the boat when the boat is heated by the induction heater. New boats were thoroughly outgassed

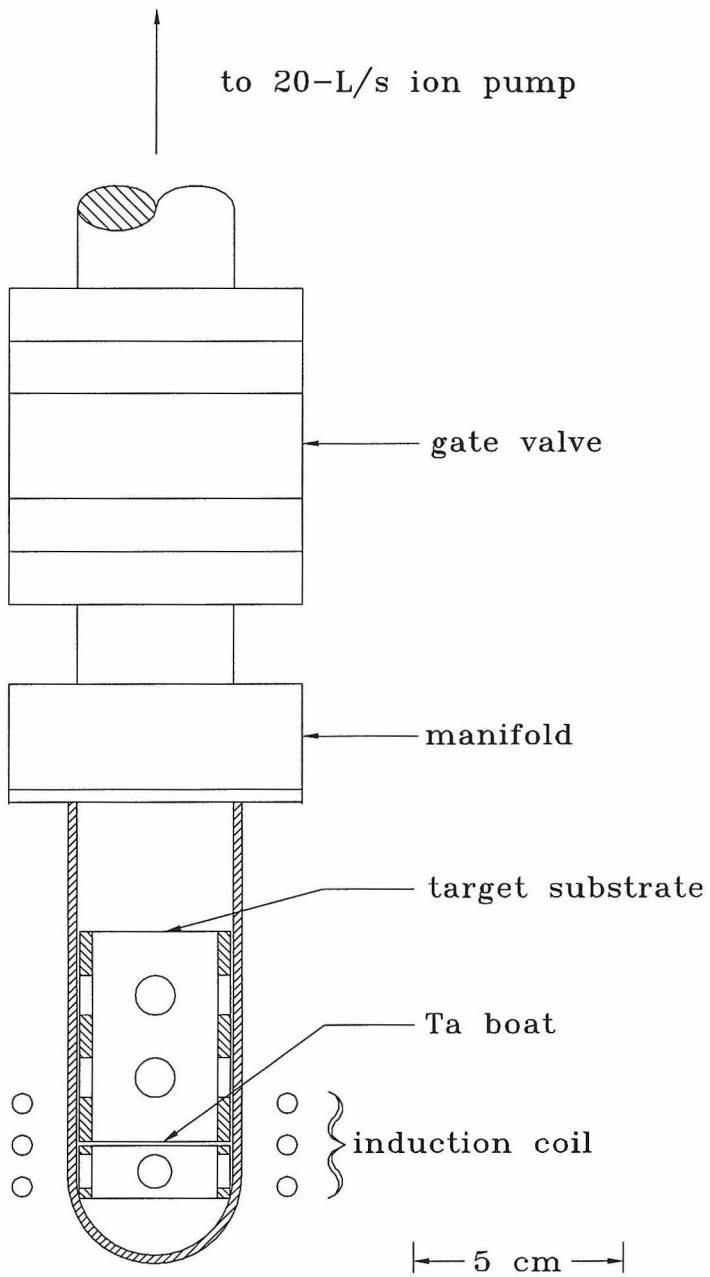

Figure 8.1: Side view of the target-production apparatus. Also connected to the manifold, but not shown, is a Convectron gauge and a port leading to the vent and the mechanical pump.

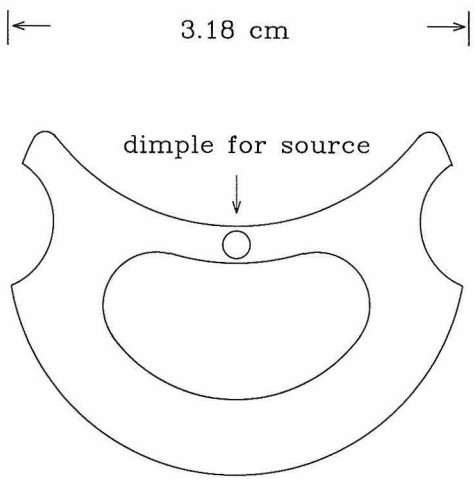

Figure 8.2: Top view of the Ta evaporation boats. The CaF_2 crystal is placed in the hemispherical dimple at the center.

for several minutes in vacuum at temperatures higher than that required for CaF_2 evaporation.

The target backing material used was oxygen-free copper, machined into disks 3.170 cm in diameter and 0.072 cm thick. The disks were first washed with detergent, and then to ensure that no machine oil was left in any scratches on the surface of the copper, each disk was etched in a 50:50 mixture of nitric acid and deionized water down to a thickness of 0.064 cm. The disks were then rinsed in deionized water and mounted inside the target production apparatus.

The CaF_2 evaporation source for the target used in this experiment was a single 201-μg crystal of optical grade CaF_2. The crystal was kept inside the boat while the boat was loaded into the apparatus by the surface tension of one drop of high-purity water placed in the evaporation boat dimple. This water would then evaporate as the quartz tube was evacuated.

Before evaporation, the evaporation boat was heated to red heat and the Cu target backing was outgassed by heating to orange heat for 30 seconds. The system was then allowed to pump and cool overnight for good vacuum.

To make a target, the evaporation boat was heated slowly until the CaF_2 crystal was observed to melt. The system was then left to cool for an hour and then the

target was transferred to the target room and mounted on the 0° beamline by the procedure described in Section 5.2.

8.2 Target Thickness Determination

The target thickness was determined using the 340-keV resonance of the $^{19}F(p,\alpha\gamma)^{16}O$ reaction. The yield of this resonance was measured using a BGO crystal, as described in Section 7.1, and fitted with an asymmetric Breit-Wigner curve. The thickness was then calculated using equation 2.25 and an $(\omega\gamma)_r$ of 22.3(8) eV in the center-of-mass frame, as measured by Becker *et al.* [Bec82].* The normalization uncertainty of the results is estimated to be 7.0%, due almost entirely to the 6% in the BGO efficiency and the 3.6% error in the strength of the resonance.

The initial thickness was 4.9(3) $\times$ 10^{16} ^{19}F atoms/cm^2, or 3.2(2) μg/cm^2. As I found that the target deteriorated under bombardment, the target thickness was remeasured periodically throughout the experiment. The final target-thickness data are shown in Figure 8.3, corresponding to a target thickness of 3.9(3) $\times$ 10^{16} ^{19}F atoms/cm^2, a loss of 27(3)%. However, since the beam was rastered over the target, the deterioration was fairly uniform – when the beam was steered to the edges of the target, the average change in the yield was less than 10%. For the data analysis, the target deterioration was assumed to be linear with accumulated charge.

8.3 Target Contamination

Due to their large (α, n) cross sections, the three major contaminants in this experiment are ^{13}C, ^{11}B, and ^{18}O. The amount of ^{13}C on each target was determined by measuring the yield from the 1.053-MeV resonance in $^{13}C(\alpha,n)^{16}O$. The yield curve was fitted to one or more Breit-Wigner peaks and the thickness calculated using equation 2.25 and an $(\omega\gamma)_r$ of 11.9(6) eV in the center-of-mass frame as measured by

*I did not use the $(\omega\gamma)_r$ given by Croft *et al.* [Cro91], as I was unable to reproduce their value of 23.7(10) eV – the value I calculated for $(\omega\gamma)_r$ from the thick target yield given in their paper was 21.4 eV.

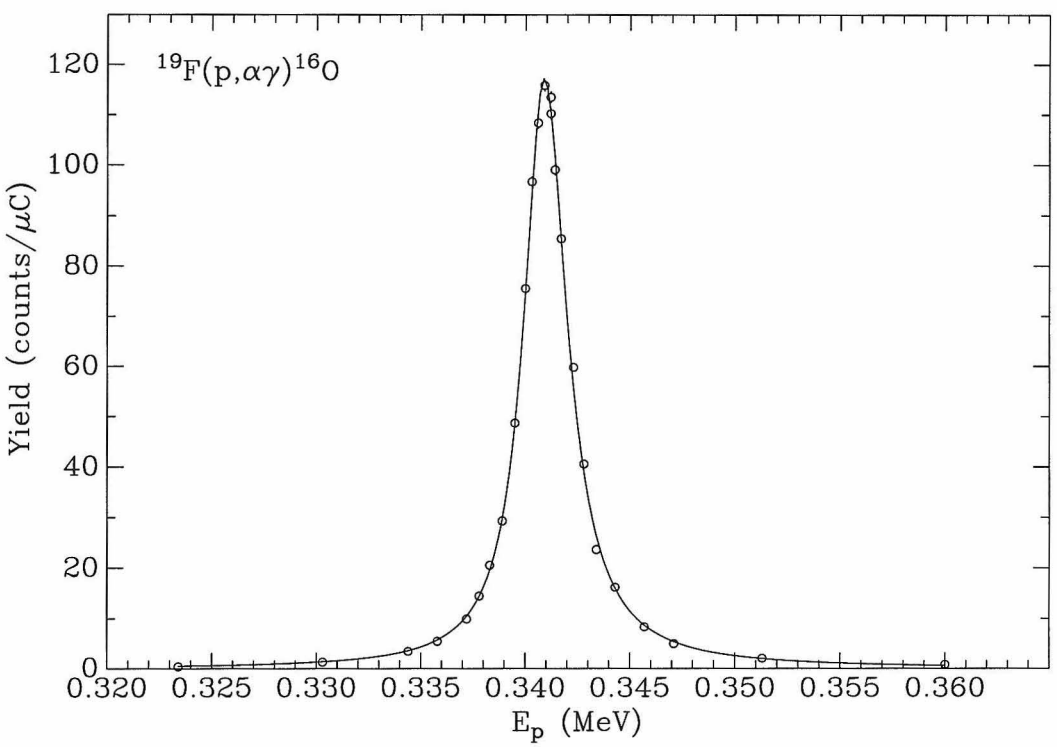

Figure 8.3: Typical $^{19}\mathrm{F}(p,\alpha\gamma)^{16}\mathrm{O}$ excitation function for the 3.2-μg/cm^2 CaF_2 target. The solid curve is the fit to the data with an asymmetric Breit-Wigner function (two truncated Breit-Wigners joined at their peak), no background, and was used to determine the target thickness. The statistical errors are smaller than the size of the data points.

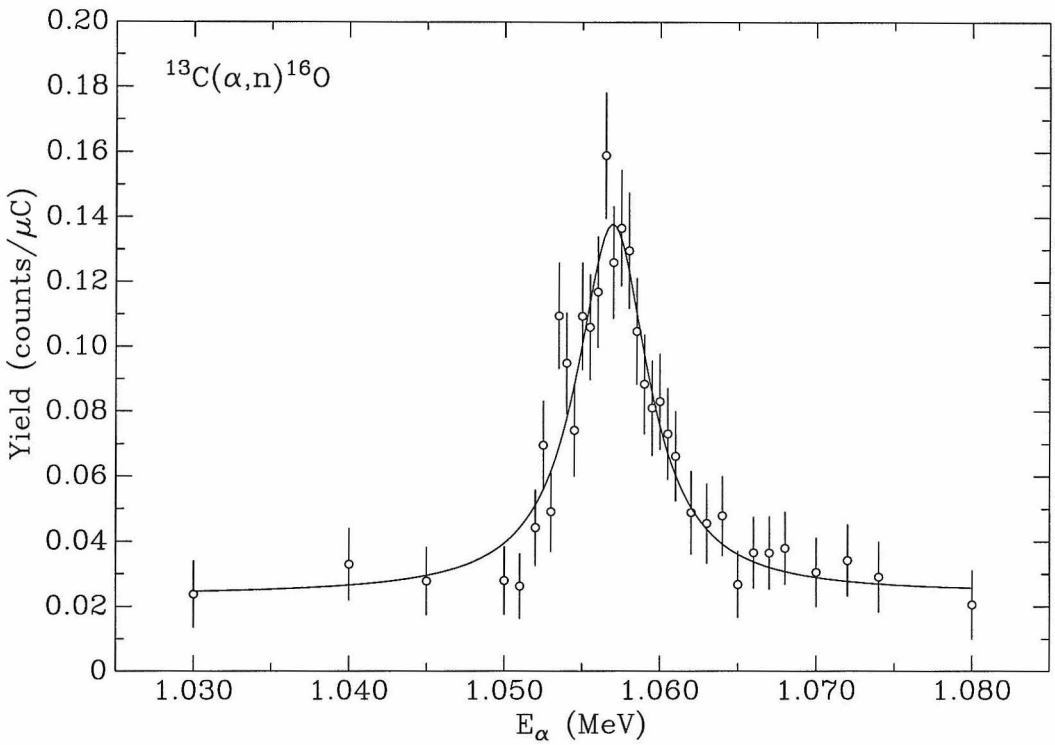

Figure 8.4: $^{13}C(\alpha, n)^{16}O$ excitation function for the 3.2-μg/cm^2 CaF_2 target. The solid curve is the fit to the data of a Breit-Wigner function, and was used to determine the target thickness. The error bars represent the statistical errors. From the fit to the data, the amount of ^{13}C on the target at this point is $3.3(5) \times 10^{13}$ atoms/cm^2.

Brune *et al.* [Bru93].

The amount of ^{13}C contamination was remeasured periodically, and found to vary with time, from a high of $6.7(14)\times10^{13}$ ^{13}C atoms/cm^2 initially, to a low of $2.5(5)\times10^{13}$ atoms/cm^2. The errors include a normalization error of 6.5% due to the error in the detector efficiency and the strength of the resonance, but the greatest source of uncertainty is the error in the fit. Figure 8.4 shows the final ^{13}C determination. From the fit to the data as shown by the solid curve, the measured ^{13}C thickness at this point was $3.3(5) \times 10^{13}$ ^{13}C atoms/cm^2. From studies using copper disks, I found that there seem to be two sources of carbon deposition: carbon deposited in the target layer during evaporation, and a surface layer of carbon due to residual oil vapor from the vacuum system laid down when the target is mounted in the 90° target chamber. As the amount of carbon did not increase during data-taking, but rather decreased,

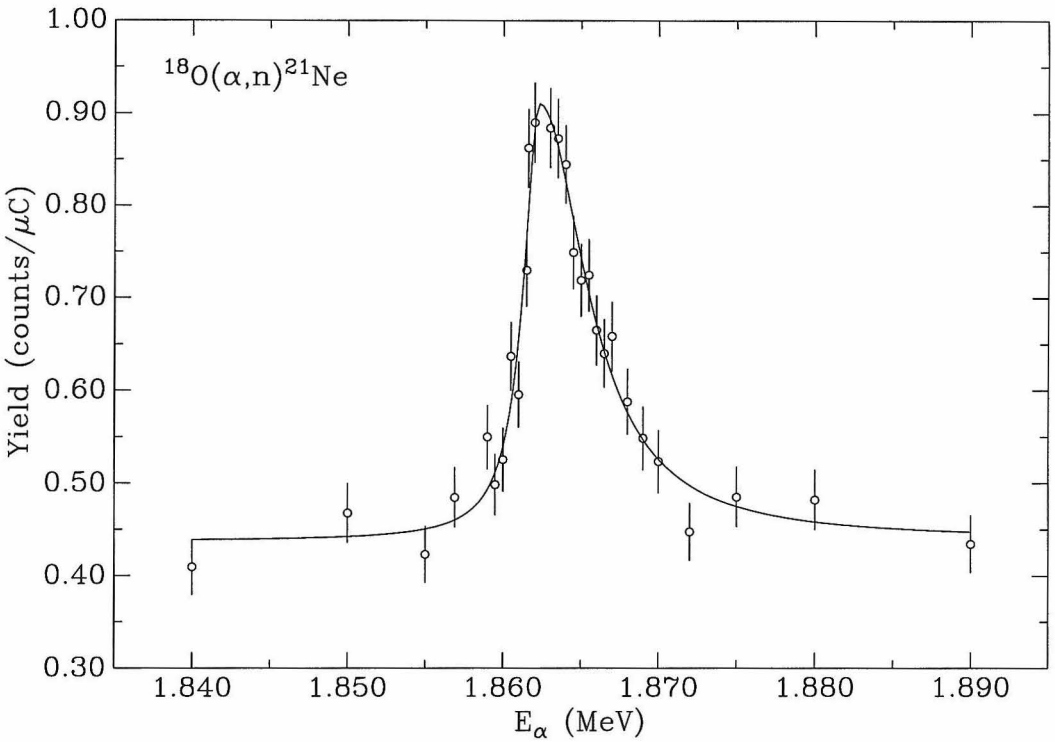

Figure 8.5: $^{18}O(\alpha, n)^{21}Ne$ excitation function for the 3.2-μg/cm^2 CaF_2 target. The solid curve is the fit to the data of a Breit-Wigner function, and is used to determine the target thickness. The error bars represent the statistical errors.

beam-induced deposition of carbon on the target did not appear to be significant.

The amount of ^{18}O on the target was found using the same method as for ^{13}C: the 1.864-MeV resonance was used, with an $(\omega\gamma)_r$ deduced from the cross section curve measured by Bair and Haas [Bai73]. The uncertainty in the result includes a normalization error of 26%, due almost entirely to the normalization uncertainty in the $^{18}O(\alpha, n)^{21}Ne$ cross section. The initial yield of this resonance is shown in Figure 8.5, corresponding to a thickness of $2.4(7) \times 10^{13}$ ^{18}O atoms/cm^2. The $^{18}O(\alpha, n)^{21}Ne$ yield was also measured at the end of the yield measurements, and the thickness of $^{18}O$was found to be $4.2(11) \times 10^{13}$ atoms/cm^2.

Similarly, the amount of ^{11}B on the target was found using the 1507.2-keV resonance in $^{11}B(\alpha, n)^{14}N$, with an $(\omega\gamma)_r$ of 0.57(3) keV [Wan91]. The amount of ^{11}B was found to be $2.6(6) \times 10^{13}$ atoms/cm^2.

8.4 Yield Measurements

The neutron yields were measured for $2.28 \leq E_\alpha \leq 3.10$ MeV. The yields were first corrected for the deadtime of the detector; this correction was less than 0.5% for all points. The background was then subtracted, and found to be less than 2.4% for all yields, and less than 0.5% for yields with $E_\alpha > 2.5$ MeV. The integrated charge was corrected for leakage current, and in all cases the correction was less than 0.06%.

The amount of yield due to the target contamination was then subtracted. The amount of neutron yield due to each contaminant was calculated using equation 2.22, the results of Section 8.3, and the MCNP efficiencies. The cross sections for $^{13}C(\alpha, n)^{16}O$ and $^{18}O(\alpha, n)^{21}Ne$ were taken from Bair and Haas [Bai73], and for $^{11}B(\alpha, n)^{14}N$ were estimated from Wang *et al.* [Wan91]. As the amount of ^{13}C was found to vary during the yield measurements, the ^{13}C thickness for each day's data set was chosen such that the yield below the $^{19}F(\alpha, n)^{22}Na$ threshold was zero at its lowest point, once the entire contamination subtraction was complete. Since for $E_\alpha > 2.5$ MeV the fluorine cross section dominates the yield, the subtraction of the yield due to these contaminants was only performed below 2.5 MeV.

For $E_\alpha > 2.5$ MeV, the only effect of the contamination was the presence of three $^{18}O(\alpha, n)^{21}Ne$ resonances. These resonances were fitted, and the strengths calculated from the fit were checked to ensure that they agreed with resonance strengths derived from Bair and Willard [Bai62]. The resonances were then subtracted.

Figure 8.6 shows the neutron yield for the 3.2-μg/cm^2 target before and after the described contamination subtraction. The top diagram shows the yield below 2.5 MeV, where there is an additional systematic error of less than 0.6 counts/μC in addition to the statistical errors shown for each point. The bottom plot shows the yield over the entire range of the data; the resonances denoted with arrows are those due to ^{18}O.

Although the amount of ^{17}O on the target can be calculated from the amount of ^{18}O and the relative natural abundances of these isotopes in oxygen, the neutron yield from this reaction was found to be insignificant, and therefore no correction for

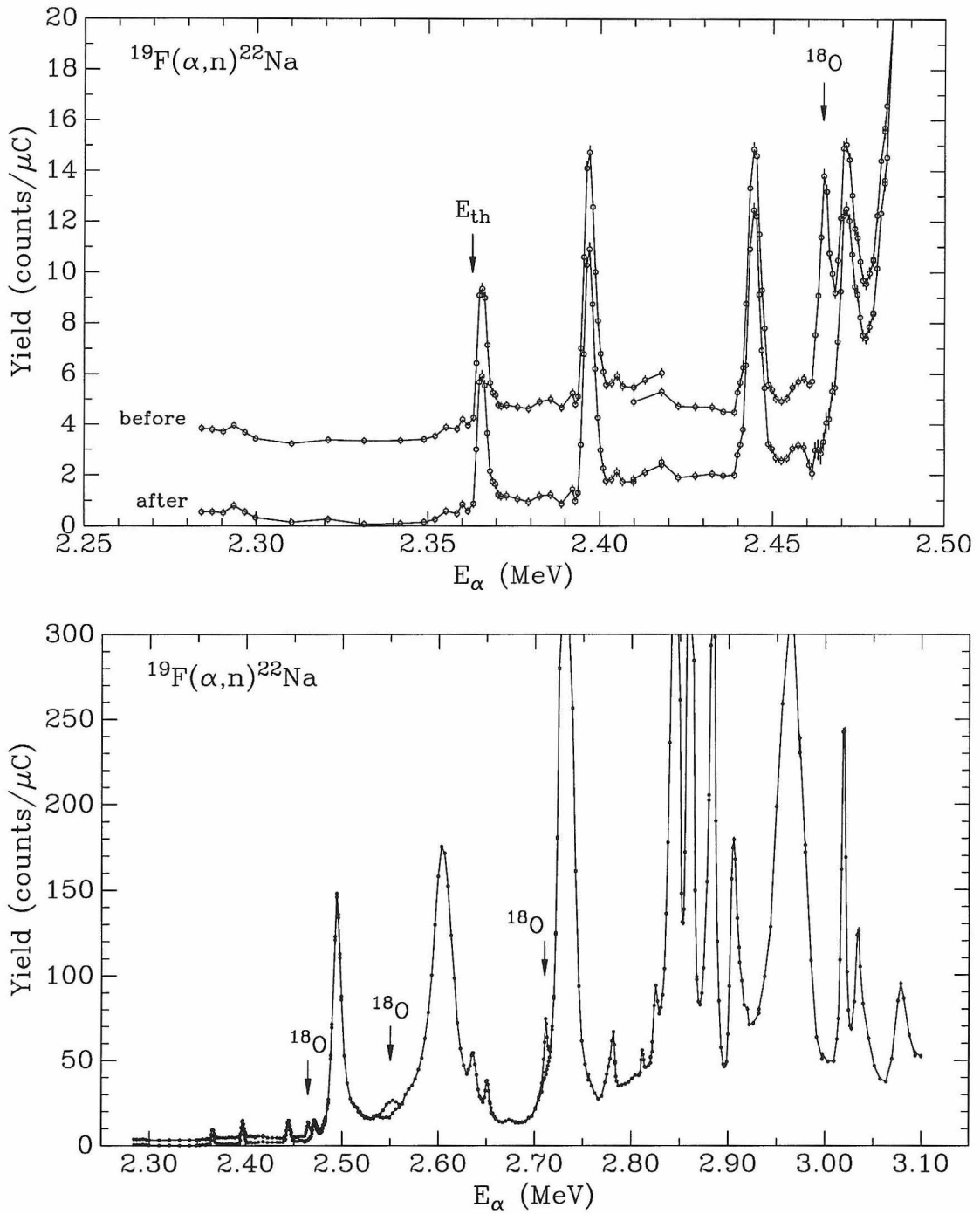

Figure 8.6: Yield from $^{19}\mathrm{F}(\alpha, n)^{22}\mathrm{Na}$ before and after subtraction of the effects of $^{13}\mathrm{C}$, $^{18}\mathrm{O}$, and $^{11}\mathrm{B}$ contamination. In addition to the statistical errors shown in the plot, there is an additional systematic error of < 0.6 counts/μC for points below 2.5 MeV due to the subtraction.

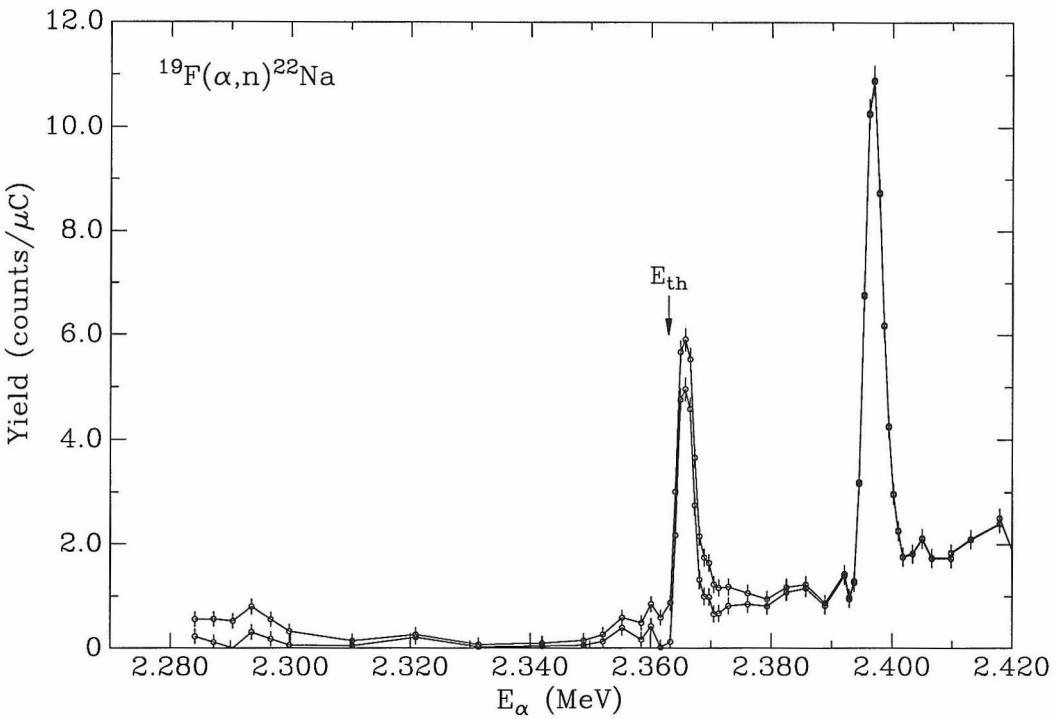

Figure 8.7: Yield from $^{19}F(\alpha, n)^{22}Na$ before and after subtraction of the effects of the unknown contaminant. In addition to the statistical errors shown in the plot, there is still the additional systematic error of < 0.6 counts/μC for points below 2.5 MeV due to the previous contamination subtraction.

this contamination was made. Similarly, no test was made for any beryllium on the target: as the cross section of $^{9}Be(\alpha, n)^{12}C$ below 3.0 MeV has its maximum value at 2.3 MeV, and as the yield at that point could be entirely accounted for by the presence of ^{13}C, ^{18}O, and ^{11}B, any contribution to the neutron yield by $^{9}Be(\alpha, n)^{12}C$ above the $^{19}F(\alpha, n)^{22}Na$ threshold would also be insignificant.

Even after the effects of the known contaminants, ^{13}C, ^{11}B, and ^{18}O, had been subtracted, there was still some neutron yield below 2.30 MeV and just at threshold that was not equal to zero within the 1σ statistical error, as can be seen from the top plot in Figure 8.6. Studies with a copper blank from 2.25 to 2.45 MeV replicated this yield, but gave no clues to its origin. Using the yields from the copper blank for normalization, these resonances were subtracted from the neutron yield for the 3.2-μg/cm^2 CaF_2 target, and the results are shown in Figure 8.7. No further resonance

above the $^{19}\mathrm{F}(\alpha, n)^{22}\mathrm{Na}$ threshold was seen in the yield from the copper blank.

Chapter 9 Data Analysis and Results

9.1 Calculation of Cross Sections

The $^{19}F(\alpha,n)^{22}Na$ cross section was calculated from the yield using equation 2.22 and the MCNP efficiency. The overall normalization uncertainty in the cross section is 8.1%, due to the 7.0% error in the target thickness and the 4% MCNP normalization uncertainty. The final cross section is plotted in Figure 9.1. The various resonances in the cross section were fitted and the resonance parameters extracted, using equation 2.25. Typical fits to the resonances are shown in Figure 9.2, and the extracted resonance parameters are shown in Table 9.1.

The principle of detailed balance was then used to calculate the $^{22}Na(n,\alpha)^{19}F$ cross section from the $^{19}F(\alpha,n)^{22}Na$ cross section, using equation 2.30, and the results are plotted in Figure 9.3. (It is an artifact of the detailed balance analysis that cross sections for energies below threshold in the forward channel change sign.) Resonance strengths for these resonances may be calculated from Table 9.1 using equation 2.32: by substituting in the spins of the various particles, the ratio of resonance strengths for the $^{22}Na(n,\alpha)^{19}F$ reaction to the $^{19}F(\alpha,n)^{22}Na$ reaction is just $\frac{1}{7}$.

9.1.1 Comparison with Existing Data

Figure 9.4 shows the $^{19}F(\alpha,n)^{22}Na$ total cross sections measured by Balakrishnan *et al.* [Bal78] and the differential cross sections for the n_0 ground state neutron group measured by van der Zwan and Geiger [Zwa77] against my data. From the top graph it may be seen that the Balakrishnan data have problems with normalization and experimental resolution. In addition, they have misidentified the peaks at 2.60 and 2.67 MeV as being due to $^{13}C(\alpha,n)^{16}O$ and $^{19}F(\alpha,n)^{22}Na$, respectively, while from both my data and the van der Zwan differential cross sections, it is clear that the

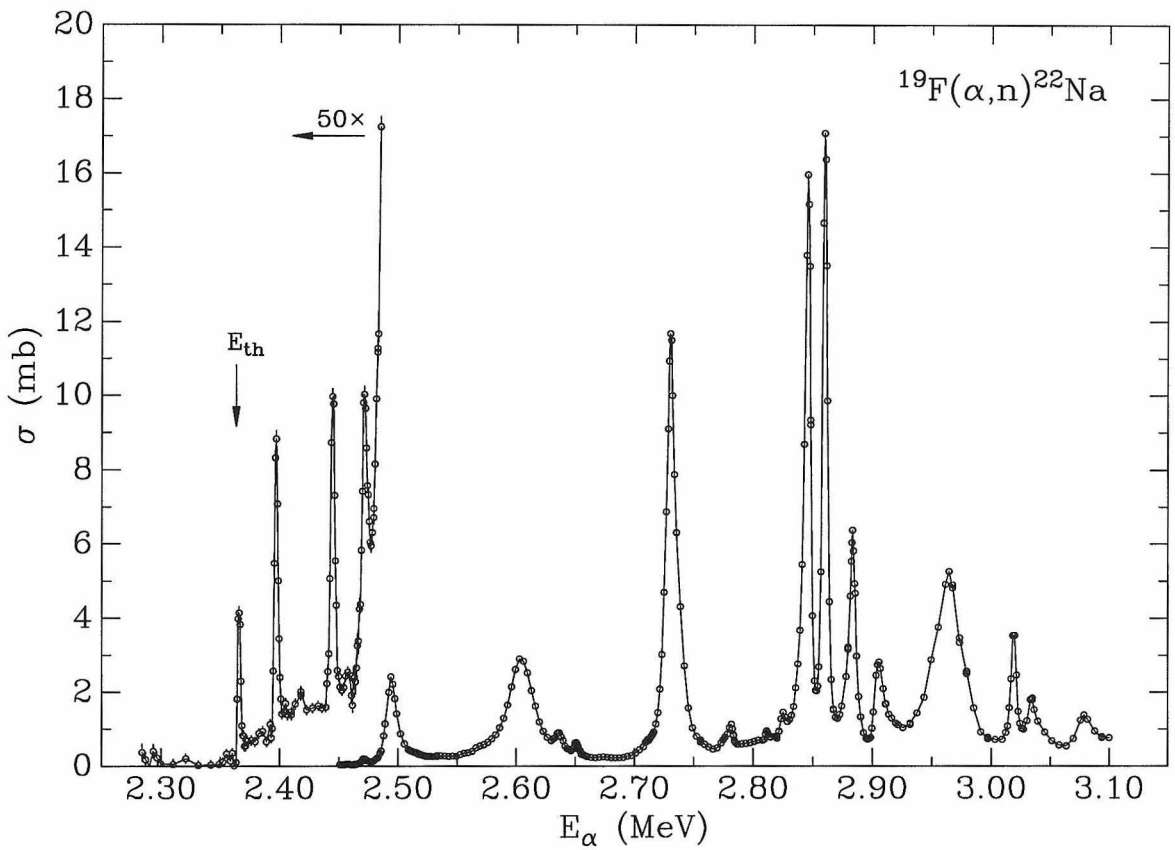

Figure 9.1: Cross section for $^{19}\mathrm{F}(\alpha, n)^{22}\mathrm{Na}$. Note the change in scale below 2.48 MeV. The error bars shown are the statistical errors. There is an additional systematic error of < 0.01 mb below 2.5 MeV. The normalization uncertainty for all data points is 8.1%.

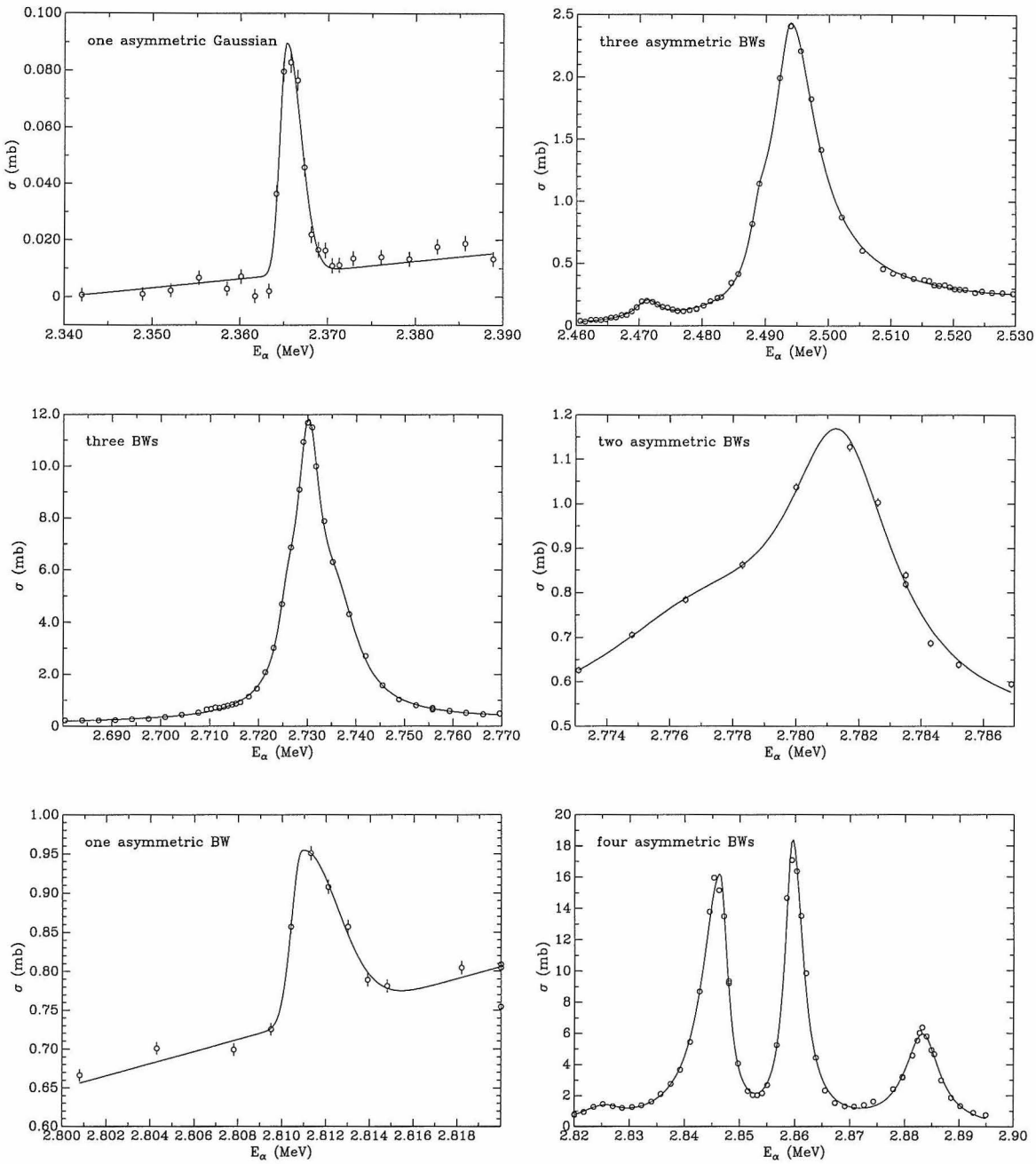

Figure 9.2: Some typical fits to the resonances in the cross section for $^{19}\mathrm{F}(\alpha, n)^{22}\mathrm{Na}$. All resonances were fitted with a combination of Breit-Wigner (BW) or Gaussian functions with linear background. Those peaks denoted as asymmetric were fitted with two truncated Breit-Wigner or Gaussian functions joined at their peaks.

E_{lab} (keV)	$\Gamma_{c.m.}$ (keV)	$(\omega\gamma)_{c.m.}$ (eV)	E_x (MeV)	
2364.4 (1)	2.93 (6)	0.38 (6)	12.4186 (10)	(a)
2396.4 (1)	2.82 (8)	0.73 (2)	12.4450 (10)	
2444.6 (1)	3.37 (6)	0.94 (2)	12.4848 (10)	
2471.3 (1)	3.63 (15)	1.30 (6)	12.5069 (10)	
2489.3 (1)	13.1 (3)	21.6 (8)	12.5218 (10)	
2494.0 (1)	6.23 (8)	28.8 (5)	12.5257 (10)	
2604.4 (1)	20.48 (12)	157.8 (11)	12.6169 (11)	
2636.0 (1)	6.32 (17)	7.8 (2)	12.6430 (11)	
2650.6 (1)	3.65 (10)	3.38 (11)	12.6550 (11)	
2673.7 (6)	7. (2)	0.8 (3)	12.6741 (12)	
2725.9 (1)	3.58 (10)	19.5 (7)	12.7172 (11)	
2730.1 (1)	4.91 (4)	132.1 (13)	12.7207 (11)	
2736.0 (1)	9.24 (7)	97.2 (12)	12.7256 (11)	
2776.9 (3)	6.7 (7)	4.4 (5)	12.7594 (12)	
2781.4 (1)	3.42 (13)	5.9 (3)	12.7631 (12)	
2810.9 (1)	2.05 (15)	0.89 (8)	12.7875 (12)	
2825.2 (1)	7.76 (19)	21.3 (6)	12.7993 (12)	
2846.4 (1)	4.71 (1)	222.3 (7)	12.8168 (12)	
2859.5 (1)	3.31 (1)	178.2 (6)	12.8276 (12)	
2883.3 (1)	6.35 (3)	112.2 (6)	12.8473 (12)	
2904.2 (1)	7.42 (8)	49.2 (6)	12.8645 (12)	
2964.7 (1)	23.15 (16)	346. (3)	12.9145 (12)	
3018.9 (1)	3.94 (5)	40.5 (6)	12.9593 (12)	
3033.9 (1)	4.9 (2)	17.1 (10)	12.9717 (13)	
3041.5 (5)	11.2 (14)	16. (2)	12.9780 (13)	
3077.3 (2)	9.2 (6)	22.8 (15)	13.0075 (13)	

(a) average of three measurements from the same target

Table 9.1: Table of resonance parameters for $^{19}\mathrm{F}(\alpha, n)^{22}\mathrm{Na}$. The laboratory energy and associated error are the values returned by the fit; there is an additional 0.05% uncertainty due to the energy calibration. The true resonance energy will be smaller than the laboratory energy by approximately half the target thickness (3.1(3) keV at 2.36 MeV). The quoted $\Gamma_{c.m.}$ is the observed width, which includes contributions from the target thickness and straggling; the true Γ will be smaller. The error quoted in $(\omega\gamma)_{c.m.}$ is the error returned by the fit; there is an additional normalization error of 8.1% from the cross section. E_x is the excitation energy in the compound nucleus, $^{23}\mathrm{Na}$. The error quoted in E_x is the total error from my data, including both the statistical and systematic errors, but not including the error in the nuclear masses.

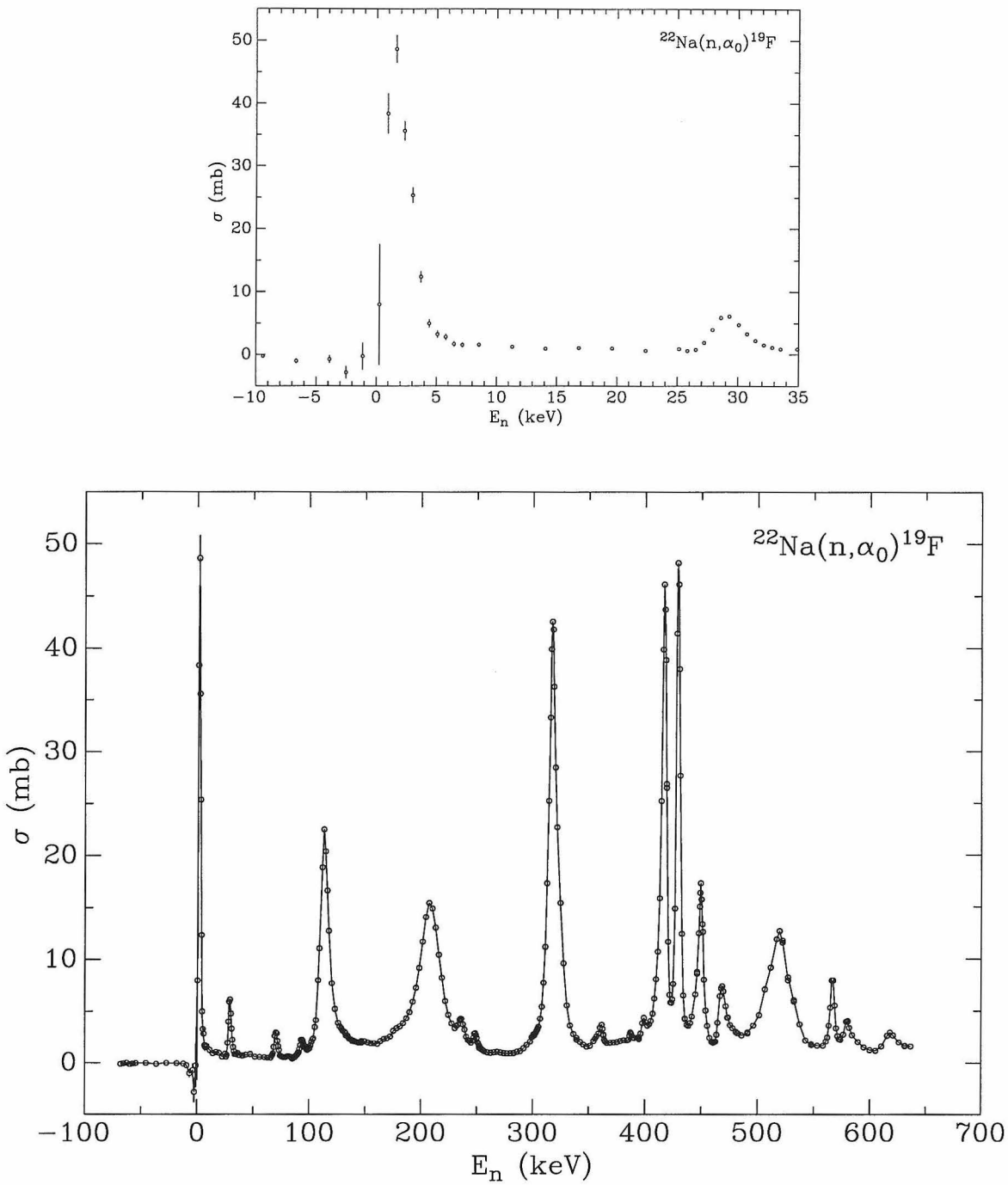

Figure 9.3: Cross sections for $^{22}\mathrm{Na}(n,\alpha_0)^{19}\mathrm{F}$. The top plot is the same data but magnified about E_n=0. The error bars represent the statistical errors.

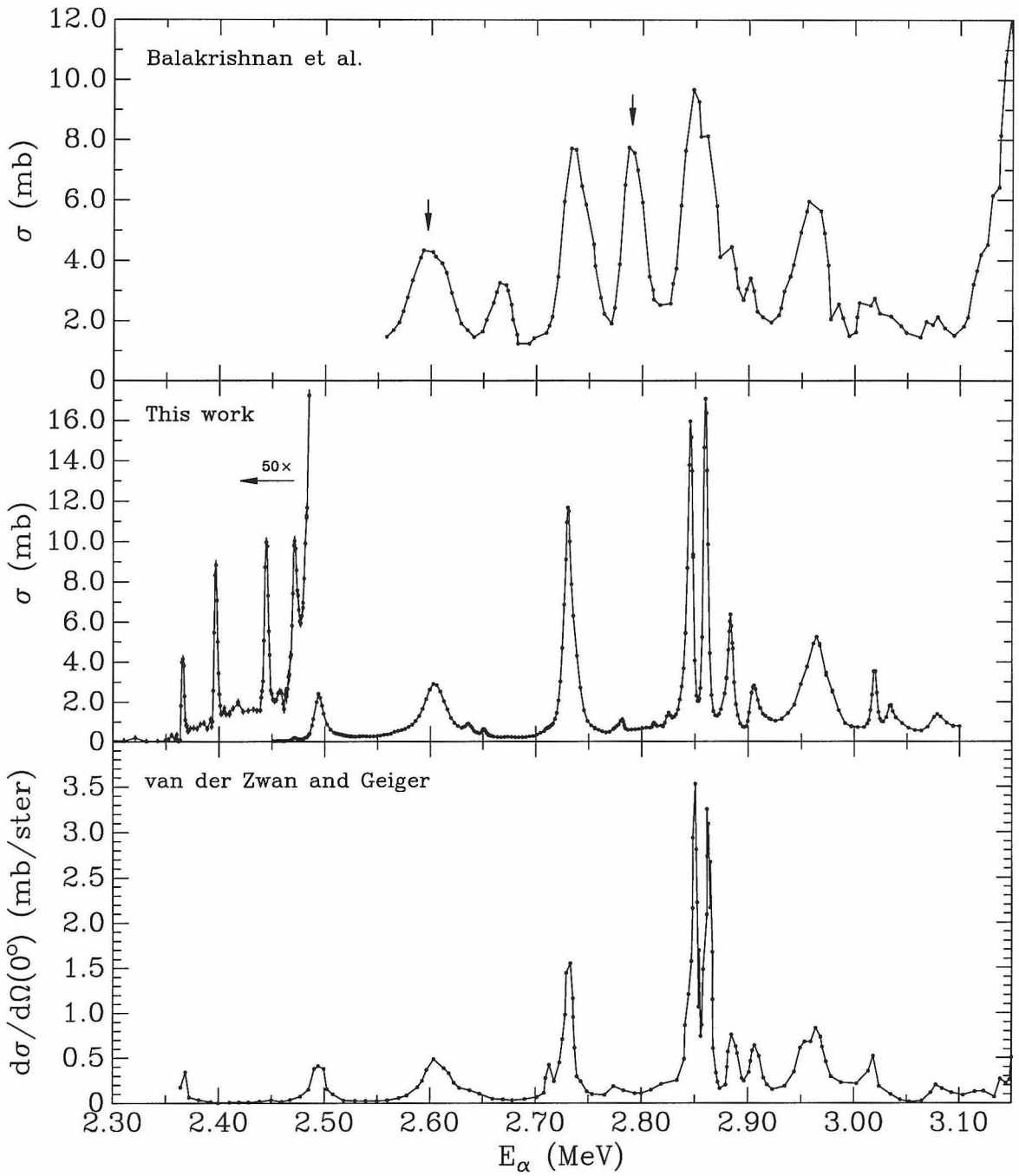

Figure 9.4: Comparison between my data and total cross sections measured by Balakrishnan *et al.*, and the 0° differential cross sections measured by van der Zwan and Geiger. Balakrishnan *et al.* state that their data contain contributions from $^{13}C(\alpha, n)^{16}O$ and identify the peaks marked with arrows as being due to ^{13}C.

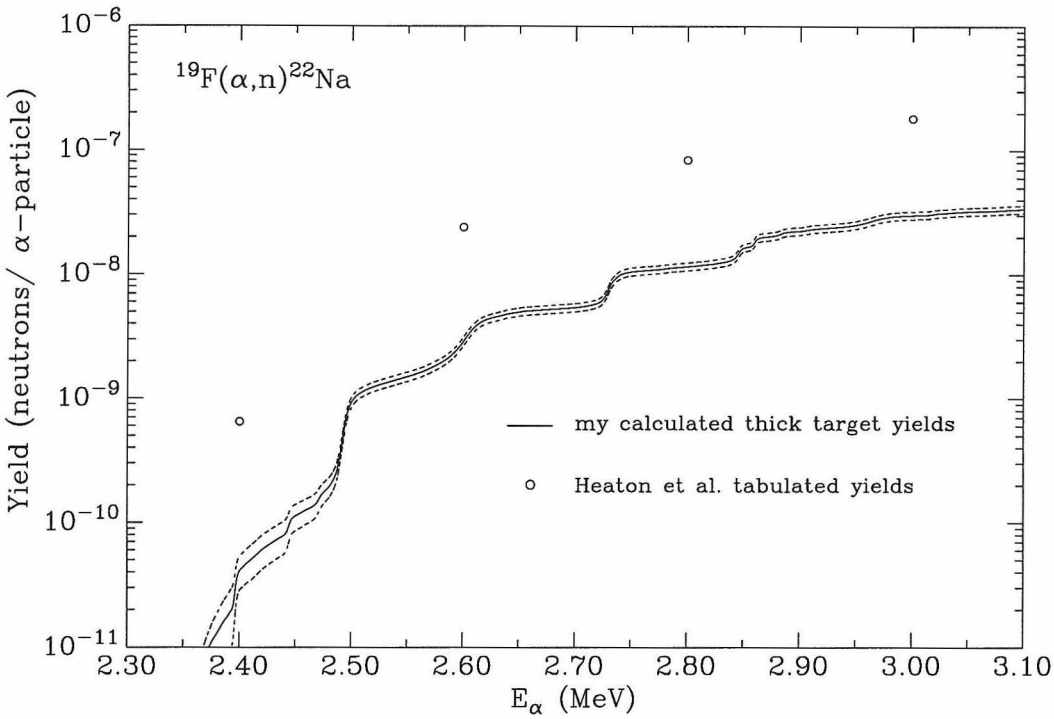

Figure 9.5: Thick target yields for $^{19}\mathrm{F}(\alpha, n)^{22}\mathrm{Na}$ for a pure fluorine target. The solid curve represents the thick target yields calculated from my cross sections and the dotted lines represent the associated error bars.

former is due to $^{19}\mathrm{F}(\alpha, n)^{22}\mathrm{Na}$, while the latter is due to $^{13}\mathrm{C}$ contamination.

As the van der Zwan and Geiger data are differential cross sections, no direct comparisons of peak height are appropriate. However, there is a good correspondence in energies for resonances observed in the total cross section and at 0°.

9.1.2 Thick Target Yields

The thick target yield for a pure fluorine target was calculated from my cross sections using equation 2.24 and Ziegler's formula for the stopping power of fluorine [Zie77] and is shown in Figure 9.5, plotted against the thick target yields tabulated by Heaton *et al.* [Hea89]. The two thick target yields disagree by a factor of 16 and 6 at 2.4 and 3.0 MeV, respectively. However, the yields tabulated by Heaton are based on the cross sections derived by Norman *et al.* [Nor84], which range from 3.5 to 10.0 MeV,

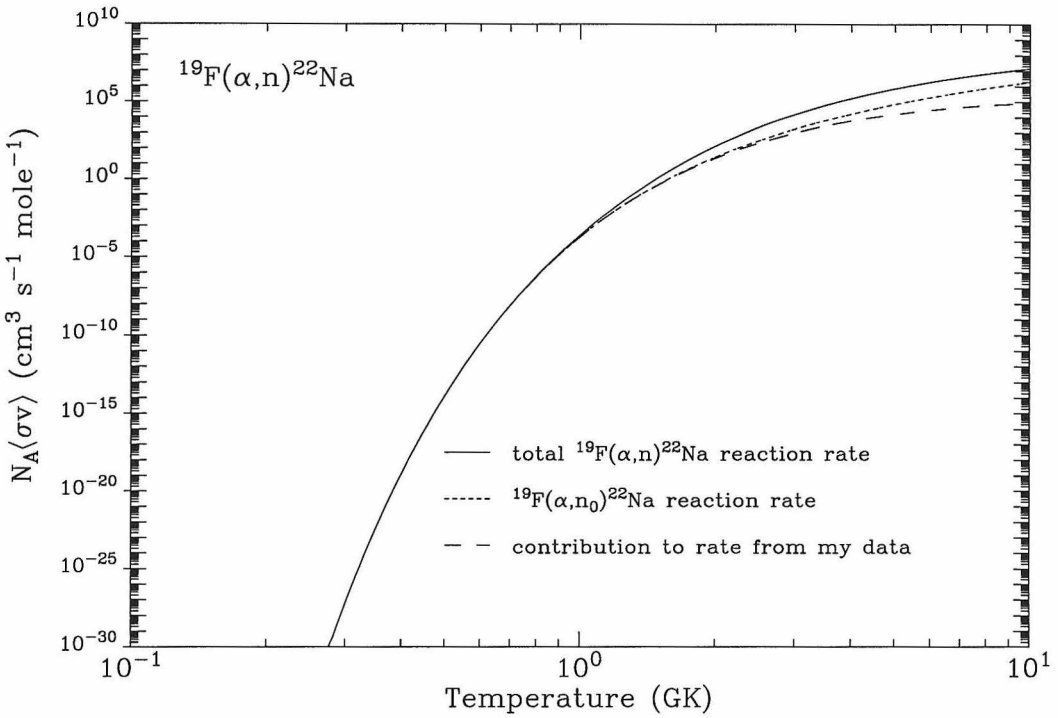

Figure 9.6: Reaction rate for $^{19}\mathrm{F}(\alpha, n)^{22}\mathrm{Na}$. The normalization uncertainty for my contribution to the reaction rate is 8.1%.

so it should not be surprising if their calculations do not reflect the cross section accurately below the range of the Norman data. According to the Balakrishnan cross sections [Bal78], the cross section drops from 25 mb at the resonance at 3.3 MeV to less than 2 mb at 3.1 MeV, and extrapolating from higher cross sections may not adequately reflect this fall-off.

9.2 Calculation of Reaction Rates

The reaction rate $N_A\langle\sigma v\rangle$ was calculated from equation 2.27 by numerically integrating the cross section as plotted in Figure 9.1. Above the range of my data, $E_\alpha > 3.10$ MeV, the cross section was assumed to be linear, with a slope and y-intercept that represent the average rise of the Balakrishnan data above 3.1 MeV. The reaction rates resulting from this integration are plotted in Figure 9.6. As can be seen from the graph, the cross sections within my range of energies account for 95% of the

reaction rate below 0.78 GK and 50% below 1.3 GK.

As the $^{19}\mathrm{F}(\alpha, n_1)^{22}\mathrm{Na}$ threshold is at 3.07 MeV, the above approximation to extend the range of the cross sections beyond my data gives the total $^{19}\mathrm{F}(\alpha, n)^{22}\mathrm{Na}$ cross section and reaction rate. To determine the reaction rate for $^{19}\mathrm{F}(\alpha, n_0)^{22}\mathrm{Na}$ alone, for the purposes of detailed balance, it is assumed that only $\frac{1}{3}$ of the estimated cross section above 3.1 MeV is due to n_0 neutrons. The resulting $^{19}\mathrm{F}(\alpha, n_0)^{22}\mathrm{Na}$ reaction rate is also shown in Figure 9.6. As can be seen from the graph, the cross sections within my range of energies account for 95% of the reaction rate below 1.4 GK and 50% below 3.2 GK.

The reaction rate was then fitted to within 1% for $0.01 < T < 10.$ GK by the analytical expression

$$\begin{aligned} N_{\mathrm{A}}\langle\sigma v\rangle_{\alpha,n} \;=\; & \frac{2317.}{T^{1/2}} \exp\left(-\frac{22.6174}{T^{1/3}}\right) \times \left(-1.0 + 169.7\,T - 23.67\,T^2 + 1.003\,T^3\right) \\ & +7.702 \times 10^3\, T^{-3/2} \exp\left(-\frac{22.6734}{T}\right) \\ & +2.669 \times 10^6\, T^{-3/2} \exp\left(-\frac{24.2359}{T}\right) \\ & +2.443 \times 10^7\, T^{-3/2} \exp\left(-\frac{26.7610}{T}\right) \\ & +A\, T^{-1/2} \exp\left(-\frac{29.7110}{T^{1/3}}\right) \times \left(1.0 + B\,T + C\,T^2\right) \;, \end{aligned} \tag{9.1}$$

where T is the temperature in GK. The first term represents the contribution from a smoothly varying cross section, while the next three terms represent resonances in the cross section from my region of energies. The last term represents the contribution from the approximation extending the range of the cross section above my energies. For the total $^{19}\mathrm{F}(\alpha, n)^{22}\mathrm{Na}$ reaction rate, the values of the constants A, B, and C are 4.015×10^8, 8.370×10^{-2}, and 3.369×10^{-3}, respectively. For the $^{19}\mathrm{F}(\alpha, n_0)^{22}\mathrm{Na}$ reaction rate these constants are 3.520×10^6, 1.879, and 0.1242, respectively. This analytical expression then has an overall uncertainty of 7.1%, including the normalization uncertainty in the cross sections and the error in the analytical fit.

From equation 2.31, the reaction rate for the inverse reaction may be calculated

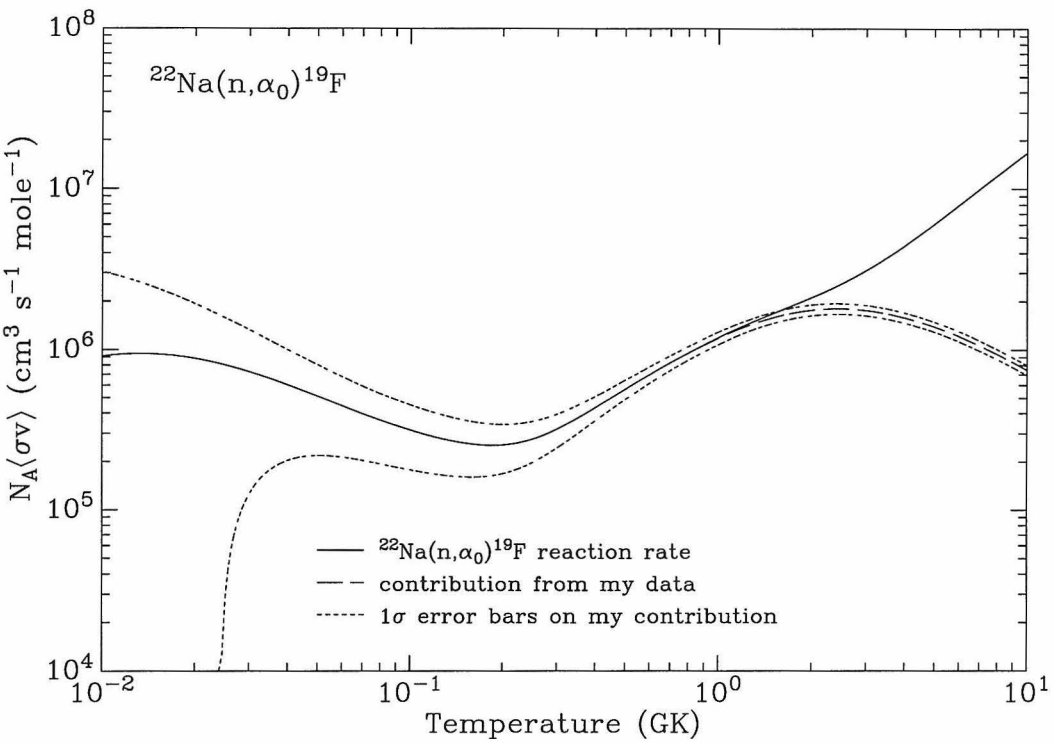

Figure 9.7: Reaction rate for $^{22}\mathrm{Na}(n,\alpha_0)^{19}\mathrm{F}$. The 1σ error for my contribution to the reaction rate includes all statistical and systematic errors in the cross section.

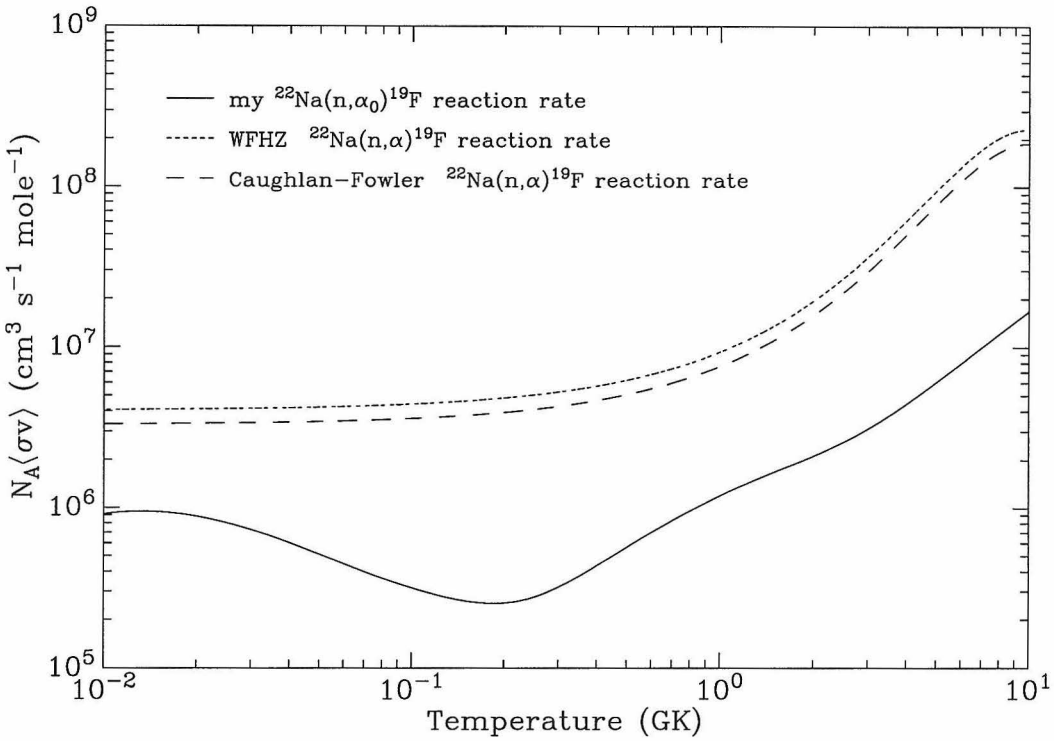

Figure 9.8: Comparison of experimental reaction rate with the Hauser-Feshbach rates calculated by Woosley, Fowler, Holmes, and Zimmerman (WFHZ) and Caughlan and Fowler.

from the relation

$$N_{\rm A}\langle\sigma v\rangle_{n,\alpha_0} = 0.906218\ \exp\left(\frac{22.64854}{T}\right)\ N_{\rm A}\langle\sigma v\rangle_{\alpha,n_0}\ . \tag{9.2}$$

Thus, the rate for ^{22}Na$(n,\alpha_0)^{19}$F may be calculated from equations 9.1 and 9.2, and is plotted in Figure 9.7.

9.2.1 Comparison with Hauser-Feshbach Calculations

In Figure 9.8, the reaction rate derived from my data is plotted against the semiempirical reaction rates calculated from Hauser-Feshbach models by Woosley *et al.* [Woo78] and Caughlan and Fowler [Cau88]. The latter two rates have the same functional form and differ only by a multiplicative constant. My rate is lower than the Hauser-Feshbach rates by a factor of 4 at low temperatures (0.01 GK) and a factor of 20

at higher temperatures (10 GK), but this is only to be expected since the Hauser-Feshbach rates include contributions from the (n, α_1) and (n, α_2) reactions which are known to be important [Koe97]. Improved Hauser Feshbach calculations which incorporate my experimental measurements would likely reduce the uncertainty associated with the total $^{22}\mathrm{Na}(n, \alpha_0)^{19}\mathrm{F}$ rate, which was estimated to be a factor of about two or three by Woosley *et al.* [Woo78].

Part IV

$^{22}\mathrm{Ne}(p,n)^{22}\mathrm{Na}$

Chapter 10 Experimental Procedures

10.1 Target Preparation

The ^{22}Ne targets used in this experiment were prepared by Stefan Schmidt at the Dynamitron–Tandem–Laboratorium, Ruhr-Universität Bochum, Germany, with the method described by Seuthe *et al.* [Seu87].

Briefly, the targets were made by implanting a ^{22}Ne beam into Ta backings. The ^{22}Ne beam was made by magnetically analyzing a natural neon beam, and passing it through a Ta collimator. The beam was then focussed onto the target backing through a circular collimator 1 cm in diameter. Magnetic steerers located ~2 meters upstream from the target rastered the ion beam over the backings. Previous tests [Seu87] have shown that the distribution of implanted ions is "nearly homogeneous" over the area of implantation.

To get a target thickness on the order of 5 keV for a 3 MeV proton beam, the implantation energies for the two targets were chosen to be 15 and 30 keV. The final dose received by the target implanted at 15 keV was 86 mC, while the other target received a dose of 320 mC. The resulting stoichiometry was on the order of one ^{22}Ne atom per four Ta atoms, which is much less than the ratio of 1:2 previously achieved [Seu87]. Ta backings were used for these targets because although Ta is known to have a non-negligible (p, n) background, Ne-implanted Ta targets have been well characterized [Seu87, Sel67]. The target backings were machined into disks 3.170 cm in diameter and 0.038 cm thick. The disks were first washed with detergent and rinsed, and then to ensure that no impurities remained on the surface, each disk was etched in a bath of 2:1:1 HNO_3:HF:H_2O. The disks were then outgassed in a conventional evaporator, and shipped to Bochum for implantation.

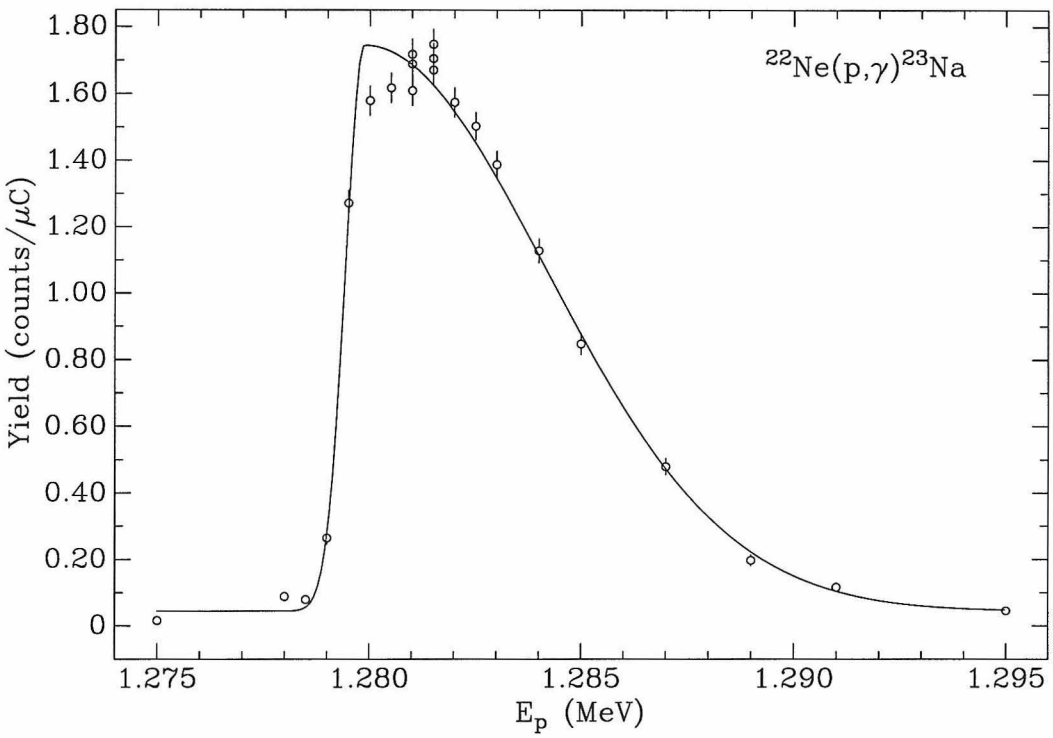

Figure 10.1: Excitation function for ^{22}Ne$(p,\gamma)^{23}$Na with the thicker ^{22}Ne target. The solid line is a fit to the data with an asymmetric Gaussian function (two truncated Gaussians joined at their peaks) and constant background. The error bars shown are the statistical errors. Although the Gaussian clearly does not fit the curve properly at the peak, the peak area calculated from the fit agrees with the area calculated by numerical integration within 0.5%.

10.2 Target Thickness Determination

The target thickness was determined using two different methods: detecting the γ rays from the ^{22}Ne$(p,\gamma)^{23}$Na reaction, and detecting the neutrons from the ^{22}Ne$(\alpha,n)^{25}$Mg reaction.

For the method using the ^{22}Ne$(p,\gamma)^{23}$Na reaction, the 440-keV γ rays from the 1280.2(5)-keV resonance were detected. The yield of this resonance for the thicker ^{22}Ne target was measured using a Ge crystal, as described in Section 7.2, and fitted with an asymmetric Gaussian curve, as shown in Figure 10.1. The thickness was then calculated using equation 2.25 and an $(\omega\gamma)_r$ of 21(2) eV in the center-of-mass frame and a fraction of 0.527 for the yield of transition from the 440 keV state to the ground

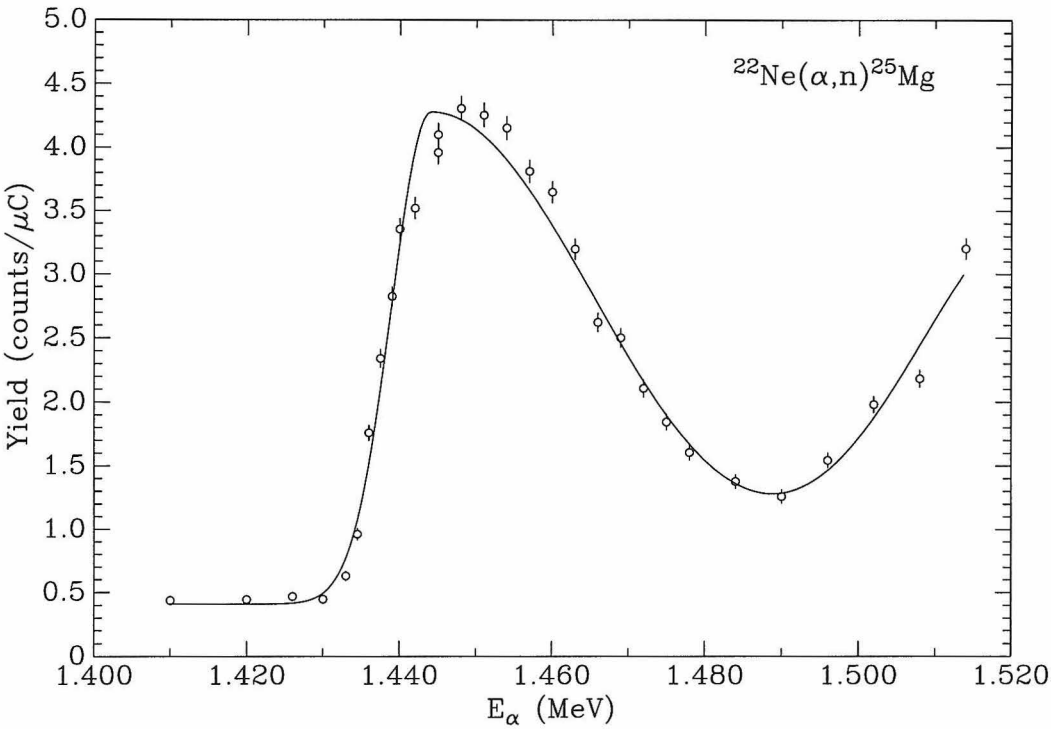

Figure 10.2: Excitation function for ^{22}Ne$(\alpha, n)^{25}$Mg with the thicker ^{22}Ne target. The data were fitted with two asymmetric Gaussians; the parameters of the second were determined from the strength of the adjoining ^{22}Ne$(\alpha, n)^{25}$Mg resonance.

state, as measured by Keinonen *et al.* [Kei77]. The initial thickness of the thicker ^{22}Ne target was found by this method to be $6.7(7) \times 10^{16}$ ^{22}Ne atoms/cm^2.

The neutron yield of the thicker ^{22}Ne target for the 1434(3)-keV resonance of the ^{22}Ne$(\alpha, n)^{25}$Mg reaction was then measured using the polycube. The resulting excitation function was fitted with asymmetric Gaussian curves, as shown in Figure 10.2. The thickness was then calculated using equation 2.25, an $(\omega\gamma)_r$ of 1.11(12) eV in the center-of-mass frame as measured by Drotleff *et al.* [Dro93], and an efficiency of 0.235(7) calculated by MCNP. The ^{22}Ne$(\alpha, n)^{25}$Mg result is a thickness of $6.8(8) \times 10^{16}$ ^{22}Ne atoms/cm^2, which agrees well with the thickness derived from the ^{22}Ne$(p, \gamma)^{23}$Na measurement.

The weighted mean of the target thickness determined using these two reactions is $6.7(5) \times 10^{16}$ ^{22}Ne atoms/cm^2.

The ^{22}Ne$(p, \gamma)^{23}$Na yield of the 1280.2(5)-keV resonance for this target was then

measured by a BGO crystal at 0°, as described in Section 7.1, before and after the yield measurements in order to determine if there were any significant target loss. The areas under the resonance before and after the proton bombardment showed a target loss of 4.7(1.4)%. In the data analysis, this target deterioration was corrected for, and assumed to be linear with accumulated charge.

This same resonance was measured in the same geometry for the thinner ^{22}Ne target, so that its thickness could be determined from the thickness of the thicker ^{22}Ne target. The areal density for the thinner ^{22}Ne target thus calculated was $3.2(2) \times 10^{16}$ ^{22}Ne atoms/cm^2.

10.3 Yield Measurements

The neutron yields were measured for $3.70 \leq E_p \leq 5.40$ MeV using the thicker ^{22}Ne target. The yields were first corrected for the detector deadtime; this correction was less than 0.8% for all points. The room background was then subtracted, and found to be less than 0.3% for all yields. The integrated charge was corrected for leakage current, and in all cases the correction was less than 2%.

It was discovered after these data had been taken that the high voltage power supply for the proportional counters in the polycube was faulty. A new power supply was installed, and the efficiency of the polycube checked using the ^{252}Cf source. The yield for the peak at 4.22 MeV was then remeasured and the area under the peak found to be 1.22(5) times the previously measured area, including the effects of target deterioration. The neutron yields involving the faulty power supply were then multiplied by this factor to correct for the change in efficiency in the polycube caused by the lowered voltage. The resulting yields are shown in the top graph of Figure 10.3.

Neutron yields from the thinner ^{22}Ne target were measured for resonances at five energies whose width was comparable with the thickness of the thicker ^{22}Ne target. As these data were not taken with the faulty power supply, and the measured area under the peak at 4.22 MeV was repeatable with measurements done once the efficiency of

the polycube had been rechecked, no renormalization was necessary.

10.3.1 Target Contamination

Unfortunately, the target yield was found to be non-zero below the $^{22}Ne(p,n)^{22}Na$ threshold, and this yield was too large to be due to the presence of ^{13}C and ^{18}O alone. Studies with a tantalum blank taken from the same batch of Ta that was used for the target backings showed that there was a significant yield from the target backing over the entire range of experimental energies, as shown in the top plot of Figure 10.3. As no structure is seen in the yield from the Ta blank, this suggests that the contaminant is distributed throughout the backing. Although the absence of resonances in the yield from the backing made it impossible to identify the contaminant(s), the fact that the yield was still non-zero below 1800 keV rules out all isotopes whose thresholds exceed 1800 keV. The most likely candidates for the contaminant(s) are ^{37}Cl, ^{51}V, and ^{55}Mn, vanadium being more probable as it is in the same column of the periodic table as Ta; however, in spite of their low abundances, it is impossible to rule out other isotopes such as ^{48}Ca, ^{49}Ti, and ^{57}Fe which have equally low thresholds.

The yield from the backing also contains a contribution from neutrons created by the beam striking the tantalum collimator. Fluctuations in the fraction of the beam hitting the collimator versus the fraction striking the target caused a non-repeatability in the observed yield which exceeded 1σ statistical error. To account for the resultant uncertainty in the yields, the statistical errors were multiplied by a factor of 3. Since the fluctuations varied only slowly with time, they had little effect on the yields for individual resonances, so the original statistical errors were used for the fits to the cross section resonances in Section 11.1.

The background due to the unknown contaminant(s) in the Ta backing was then subtracted from the raw yield from the thicker ^{22}Ne target. Although the yields below threshold do agree with zero within the statistical and systematic error bars, they do appear to be systematically high. The results of this contamination subtraction are shown in the bottom graph of Figure 10.3.

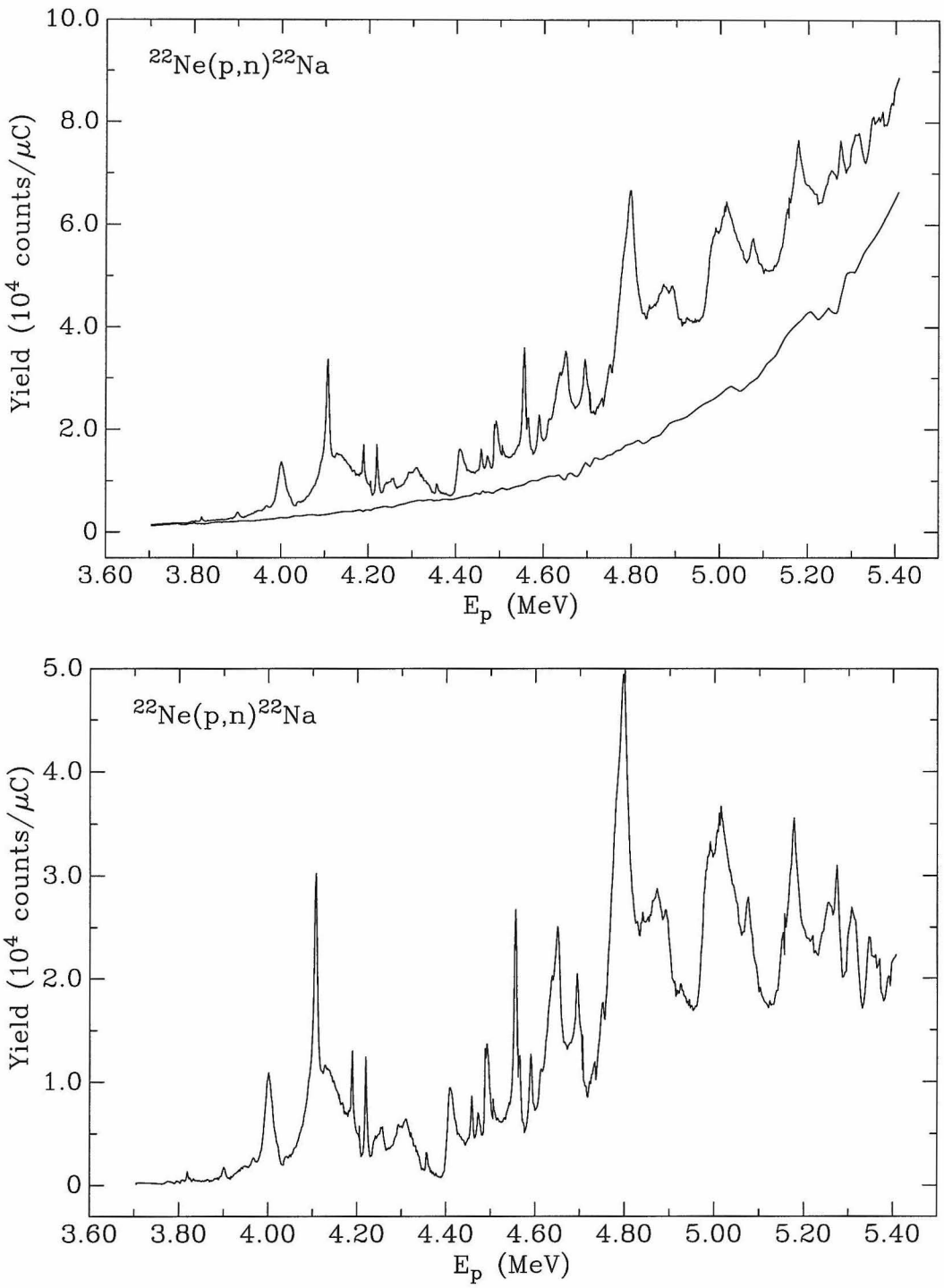

Figure 10.3: The top graph shows the neutron yield from the thicker ^{22}Ne target, with the yield from the Ta blank plotted underneath. For readability, the data points themselves are not plotted, only lines connecting the points. The bottom graph shows the neutron yield from the same target after the yield from the contamination of the Ta blank has been subtracted.

Chapter 11 Data Analysis and Results

11.1 Calculation of Cross Sections

The $^{22}Ne(p,n)^{22}Na$ cross section was calculated from the yield using equation 2.22 and the MCNP efficiency. The overall normalization uncertainty in the cross section, due to uncertainties in the target thickness determination and MCNP normalization, is 8.6% below 4.6 MeV, rising to 9.8% at 5.4 MeV. The final cross section derived from the thicker ^{22}Ne target data is plotted in Figure 11.1.

The various resonances in the cross section were fitted and the resonance parameters extracted, using equation 2.25. No attempt was made to fit the multiple resonances in the energy range 4.23-4.34 MeV and above 4.83 MeV. Typical fits to the resonances from the thicker ^{22}Ne target data are shown in Figure 11.2, while the resonances from the thinner ^{22}Ne target are shown in Figure 11.3. The extracted parameters are tabulated in Table 11.1. The parameters derived from the thin target data were used, where available, for resonances in which the observed width was comparable with the thickness of the thicker ^{22}Ne target ($\sim$ 3.1 keV at 3.8 MeV), otherwise the weighted average from the two targets was used. For the resonances at 4222.7 and 4458.5 keV, the ratio of strengths from the thinner target to the thicker target was 1.10(5) and 0.97(2), respectively.

The principle of detailed balance, using equation 2.30, was then used to calculate the $^{22}Na(n,p_0)^{22}Ne$ cross section from the $^{22}Ne(p,n)^{22}Na$ cross section below the n_1 threshold, and the results are plotted in Figure 11.4. It is an artifact of the detailed balance analysis that cross sections for energies below threshold in the forward frame change sign. As the Koehler and O'Brien $^{22}Na(n,p_0)^{22}Ne$ cross sections have a maximum energy of 420 keV, there is no region of overlap.

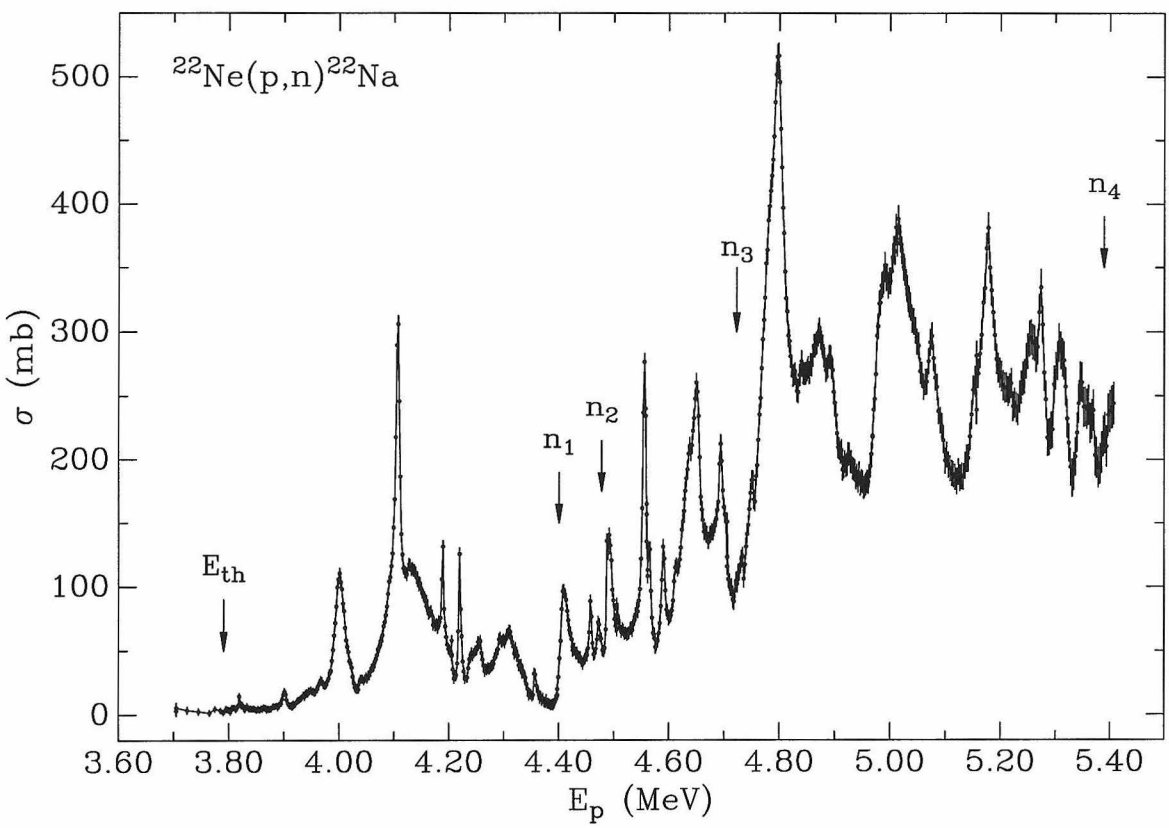

Figure 11.1: Total cross section for ^{22}Ne$(p,n)^{22}$Na calculated from the yields of the thicker ^{22}Ne target. The threshold energy and the n_{1-4} neutron thresholds are denoted by arrows. The error bars shown are the statistical errors. The normalization uncertainty for data points below 4.6 MeV is 8.6%, increasing to 9.8% at 5.5 MeV.

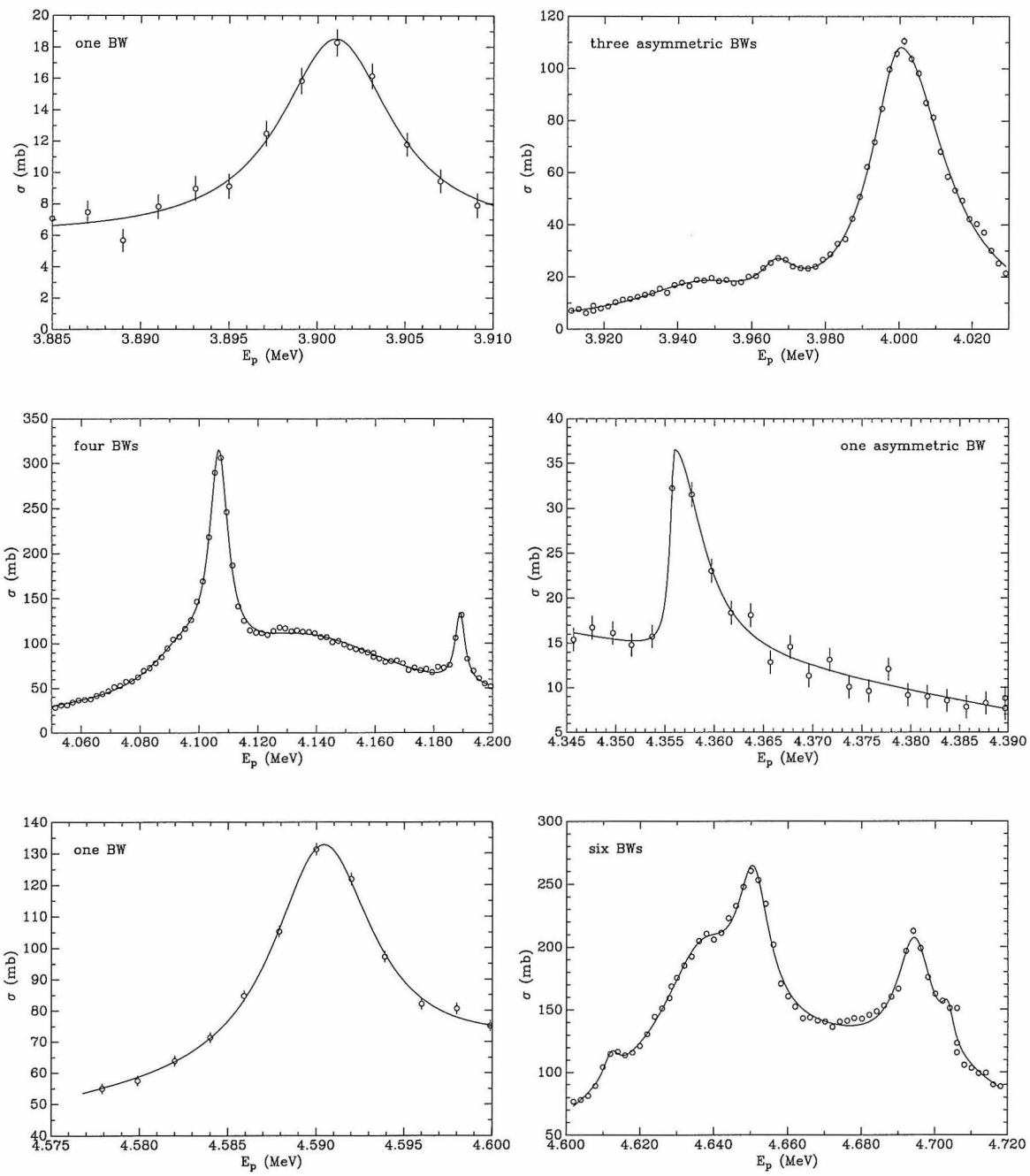

Figure 11.2: Some typical fits to the resonances in the ^{22}Ne$(p,n)^{22}$Na cross section derived from the thicker ^{22}Ne target data. All resonances were fitted with a combination of Breit-Wigner (BW) or Gaussian functions with a linear background. Those peaks denoted as asymmetric were fitted with two truncated Breit-Wigner or Gaussian functions joined at their peaks.

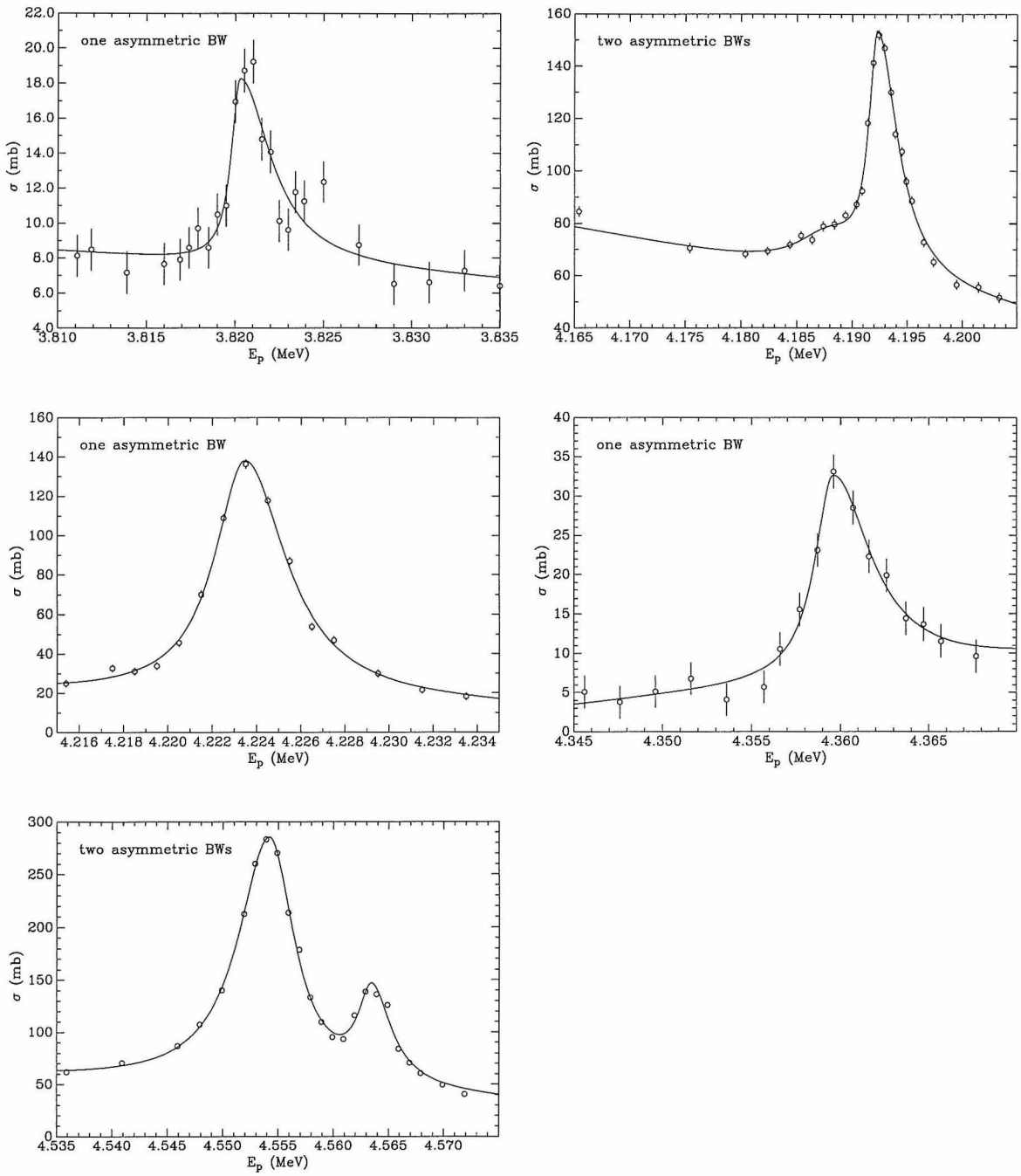

Figure 11.3: Fits to the resonances in the $^{22}\mathrm{Ne}(p,n)^{22}\mathrm{Na}$ cross section derived from the thinner ^{22}Ne target data.

E_{lab} (keV)		$\Gamma_{c.m.}$ (keV)		$(\omega\gamma)_{c.m.}$ (keV)		E_x (MeV)		
3820.3	(2)	2.6	(3)	0.031	(4)	12.446	(4)	(a,c)
3901.0	(2)	7.3	(8)	0.109	(14)	12.522	(4)	(c)
3945.7	(13)	36.	(5)	0.51	(8)	12.565	(4)	
3966.7	(7)	11.4	(18)	0.16	(3)	12.585	(4)	(c)
4000.3	(2)	23.3	(3)	2.94	(5)	12.617	(4)	(c)
4094.3	(6)	24.8	(14)	1.19	(8)	12.707	(4)	
4106.7	(1)	7.20	(12)	2.01	(4)	12.719	(4)	(c)
4136.4	(4)	76.8	(16)	8.15	(19)	12.748	(4)	
4188.0	(6)	7.4	(9)	0.14	(2)	12.798	(4)	(a,c)
4192.3	(1)	3.01	(9)	0.345	(12)	12.802	(4)	(a)
4222.7	(1)	3.91	(10)	0.556	(13)	12.830	(4)	(b,c)
4359.6	(3)	3.7	(5)	0.125	(18)	12.962	(4)	(a,c)
4407.4	(1)	18.8	(4)	2.17	(5)	13.007	(4)	(c)
4458.5	(2)	4.9	(3)	0.35	(3)	13.056	(4)	
4472.6	(3)	7.7	(6)	0.36	(4)	13.069	(4)	
4491.1	(1)	11.0	(3)	1.58	(5)	13.087	(4)	
4555.6	(1)	6.29	(6)	1.99	(2)	13.149	(4)	(b)
4563.5	(1)	3.46	(16)	0.42	(2)	13.157	(4)	(a)
4590.4	(1)	6.6	(3)	0.67	(4)	13.182	(4)	
4612.3	(3)	4.8	(8)	0.14	(3)	13.203	(4)	
4636.5	(3)	23.7	(11)	2.87	(15)	13.226	(4)	
4650.7	(1)	10.1	(4)	1.58	(8)	13.239	(4)	
4694.5	(1)	11.2	(4)	1.52	(7)	13.281	(4)	
4703.6	(2)	3.8	(6)	0.15	(3)	13.290	(5)	
4777.8	(3)	21.9	(7)	3.86	(16)	13.361	(5)	
4797.0	(1)	24.4	(4)	10.82	(19)	13.379	(5)	

(a) from fit to the thinner ^{22}Ne target data
(b) values are weighted averages from the two targets
(c) has corresponding resonance in $^{19}\mathrm{F}(\alpha, n)^{22}\mathrm{Na}$

Table 11.1: Table of resonance parameters for $^{22}\mathrm{Ne}(p, n)^{22}\mathrm{Na}$. The laboratory energy and associated error are the values returned by the fit; there is an additional 0.1% uncertainty due to the energy calibration. The true resonance energy will be smaller than the laboratory energy by approximately half the target thickness (1.48(11) and 3.1(2) keV at 3.8 MeV for the two targets). The quoted $\Gamma_{c.m.}$ is the observed width, which includes contributions from the target thickness and straggling; the true Γ will be smaller. The error quoted in $(\omega\gamma)_{c.m.}$ is the error returned by the fit; there is an additional normalization error from the cross section, which is 8.6% below 4.6 MeV, rising to 9.8% at 5.4 MeV. E_x is the excitation energy in the compound nucleus, ^{23}Na. The error quoted in E_x is the total error from my data, including both the statistical and systematic errors, but not including the error in the nuclear masses.

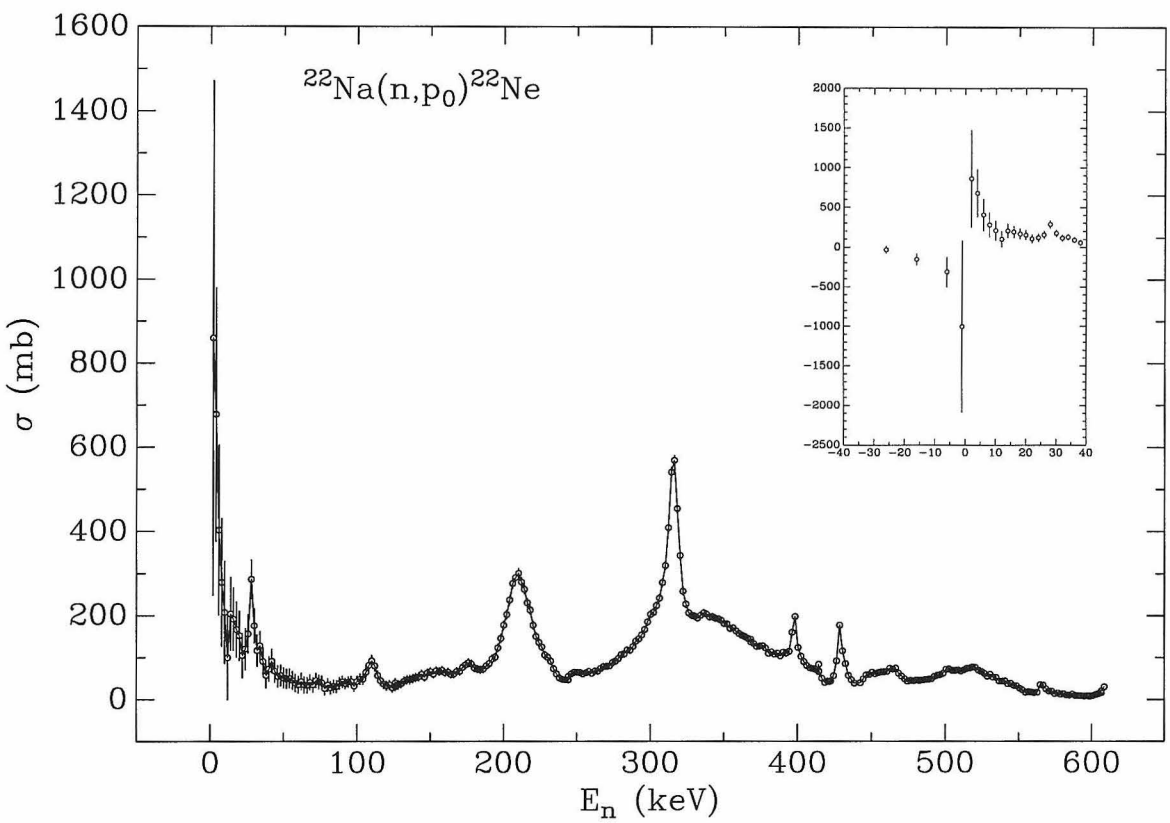

Figure 11.4: Cross sections for $^{22}\mathrm{Na}(n, p_0)^{22}\mathrm{Ne}$. The figure shows the cross sections above $E_n = 0$, while the inset plots the cross sections expanded about $E_n = 0$. The error bars represent the statistical errors.

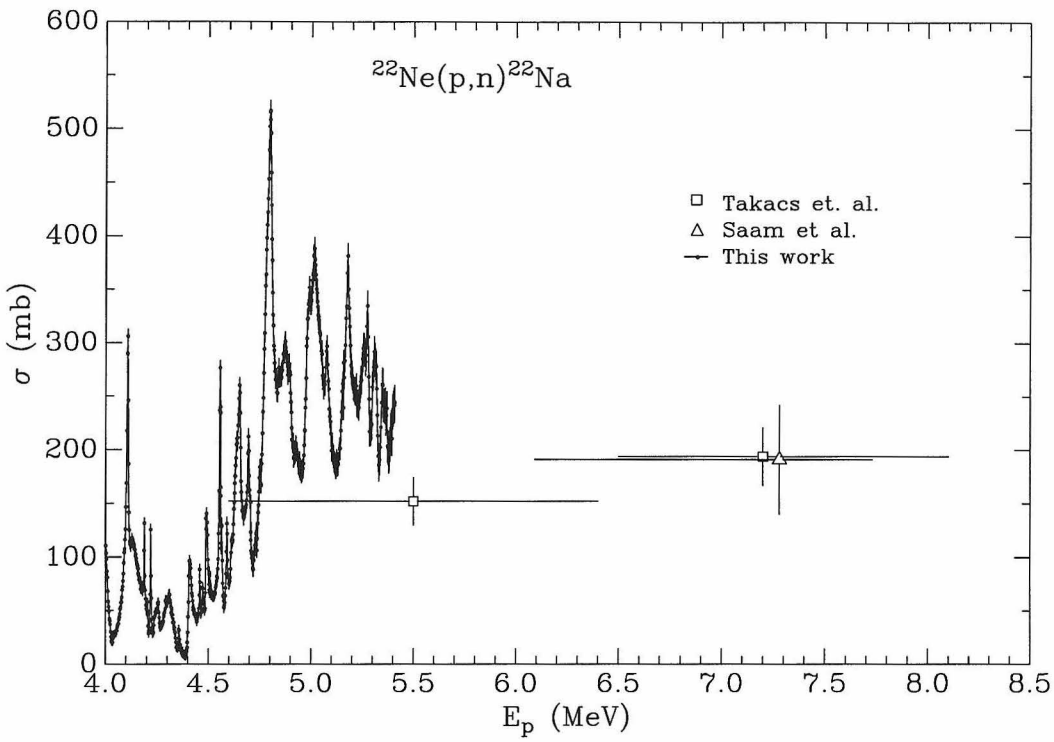

Figure 11.5: Comparison of my cross sections with those measured by Saam *et al.* and Takás *et al.*

11.1.1 Comparison with Existing Data

Figure 11.5 shows the existing data below 8.5 MeV plotted against my cross sections. The large error bars on the measurements by Saam *et al.* [Saa89] and Takács *et al.* [Tak96] are due to the fact that their experiments used gas targets, which have large uncertainties associated with determining the stopping power of the beam in their targets, straggling, beam current integration, and effective target thickness.

11.2 Calculation of Reaction Rates

The reaction rate $N_A\langle\sigma v\rangle$ was calculated from equation 2.27 by numerically integrating the cross section as plotted in Figure 11.1. Above the range of my data, the cross section was extended using the data measured by Takács *et al.* [Tak96], but as the cross section below 5.4 MeV accounts for 100.% of the reaction rate at 10 GK,

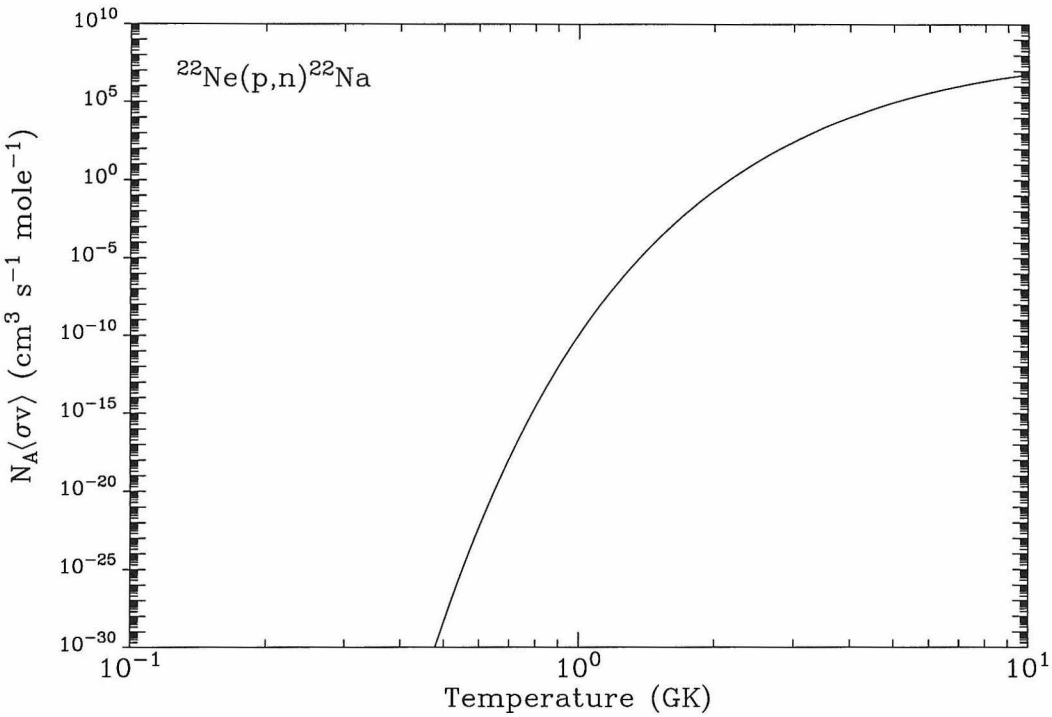

Figure 11.6: Reaction rate for $^{22}\mathrm{Ne}(p,n)^{22}\mathrm{Na}$.

this extension was unnecessary. The reaction rates resulting from this integration are plotted in Figure 11.6.

The reaction rate was then fitted to within 2% for $0.1 < T < 10$ GK by the analytical expression

$$\begin{aligned} N_{\mathrm{A}}\langle\sigma v\rangle_{p,n} &= \frac{2.094\times10^{8}}{T^{1/2}}\exp\left(-\frac{43.1845}{T^{1/3}}\right)\times\left(1.0+1.277\,T-6.963\times10^{-2}\,T^{2}\right) \\ &\quad +9.760\times10^{6}\,T^{-3/2}\exp\left(-\frac{42.1254}{T}\right) \\ &\quad +4.372\times10^{7}\,T^{-3/2}\exp\left(-\frac{42.4104}{T}\right)\ , \end{aligned} \tag{11.1}$$

where T is the temperature in GK. The first term represents the contribution from a slowly varying cross section, while the next two terms represent resonances in the cross section.

From equation 2.31, the reaction rate for the inverse reaction may be calculated

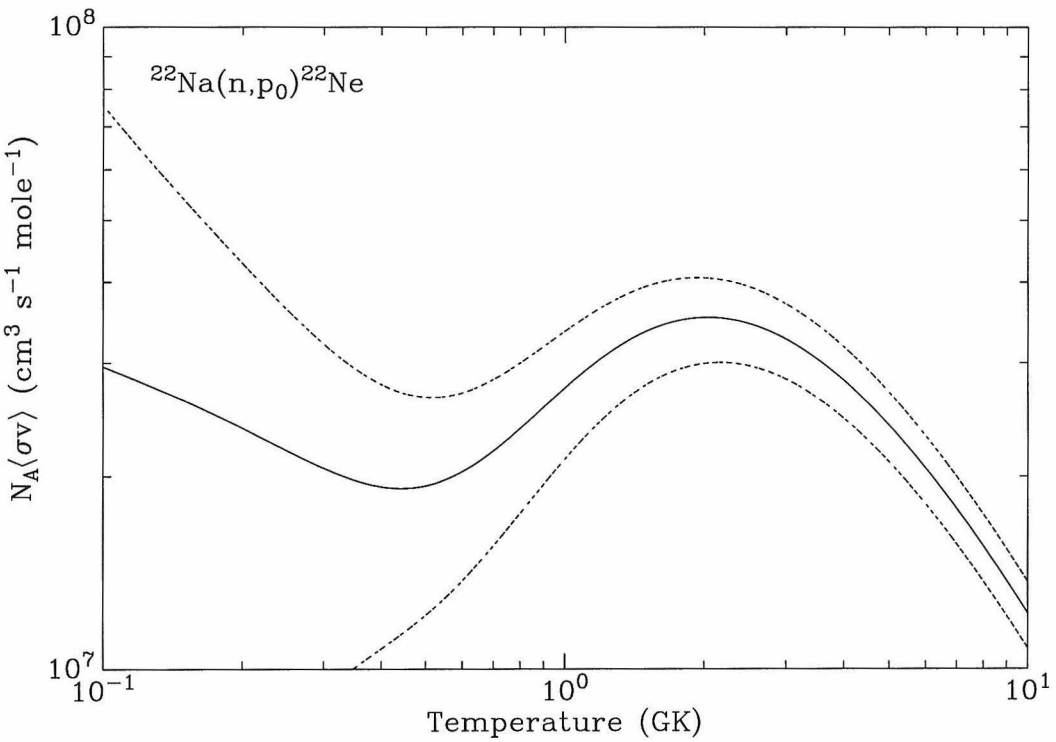

Figure 11.7: Lower limit for the $^{22}\mathrm{Na}(n, p_0)^{22}\mathrm{Ne}$ reaction rate, calculated from my $^{22}\mathrm{Ne}(p, n)^{22}\mathrm{Na}$ cross sections below the n_1 threshold.

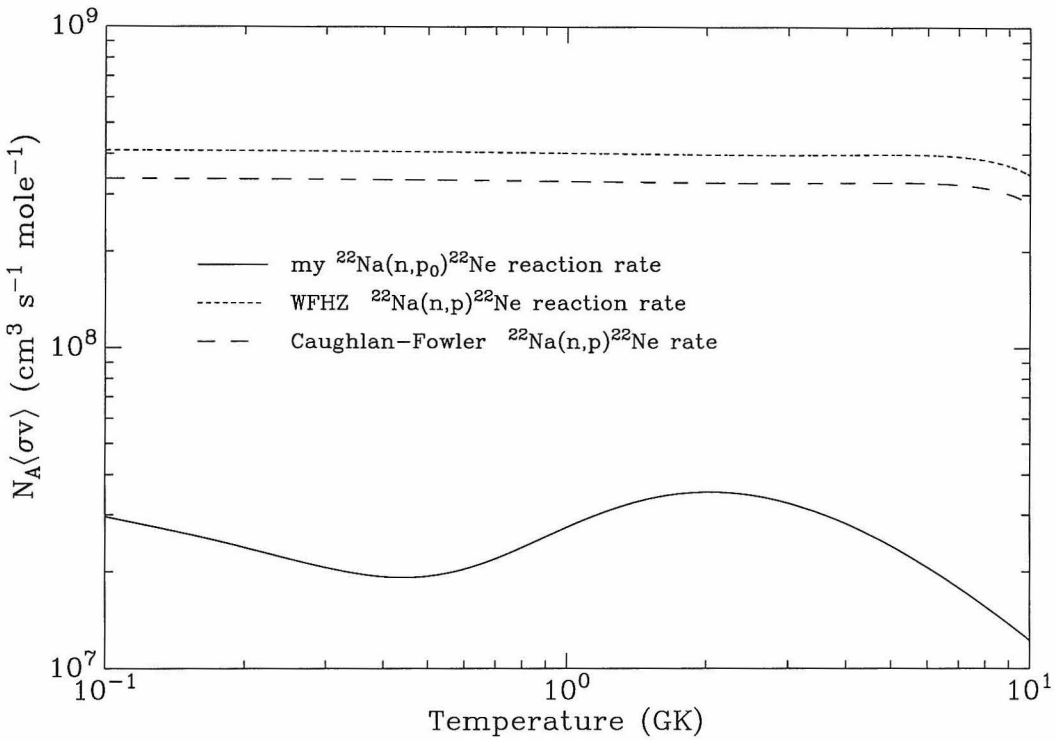

Figure 11.8: Comparison of my lower limit for the $^{22}\mathrm{Na}(n,p_0)^{22}\mathrm{Ne}$ reaction rate with the Hauser-Feshbach rates calculated by Woosley, Fowler, Holmes, and Zimmerman (WFHZ) and Caughlan and Fowler.

from the relation

$$N_\mathrm{A}\langle\sigma v\rangle_{n,p_0} = 0.142538\ \exp\left(\frac{42.06148}{T}\right)\ N_\mathrm{A}\langle\sigma v\rangle_{p,n_0}\ . \tag{11.2}$$

However, since the ratio of n_1 to n_0 neutrons above the n_1 threshold has never been measured, I am unable to do a complete calculation for the $^{22}\mathrm{Na}(n,p_0)^{22}\mathrm{Ne}$ reaction rate. Instead, I integrated the cross sections for $^{22}\mathrm{Ne}(p,n)^{22}\mathrm{Na}$ below the n_1 threshold using equation 2.27 and 11.2 in order to determine the contribution to the rate from the cross sections within that range of energies, thus establishing a lower limit to the reaction rate. The resulting rate is plotted in Figure 11.7.

11.2.1 Comparison with Hauser-Feshbach Calculations

In Figure 11.8, the lower limit to the reaction rate derived from my data is plotted against the semiempirical rates calculated from Hauser-Feshbach models by Woosley *et al.* [Woo78] and Caughlan and Fowler [Cau88]. The latter two rates have the same functional form and differ only by a multiplicative constant. It should be noted that the theoretical rates are for ^{22}Na$(n,p)^{22}$Ne and will therefore include contributions from the (n,p_1) cross sections, while my rate is for ^{22}Na$(n,p_0)^{22}$Ne alone.

11.2.2 Comparison with Experimental Rates

There is an experimental ^{22}Na$(n,p)^{22}$Ne reaction rate available for $10^{-6} < T < 0.3$ GK, calculated by Koehler and O'Brien[Koe88] from their (n,p_0) and (n,p_1) cross section measurements. They do state that the rate at the "highest temperatures" is an extrapolation of the fit to energies higher than their measurements. At $T = 0.1$ GK, their rate is approximately 1.4×10^8 moles cm^{-3} s^{-1}, while at $T = 0.3$ GK, their rate is about 7.5×10^7 moles cm^{-3} s^{-1}. The fact that their rate is much higher than my lower limit in the region of overlap is consistent with their finding from their cross sections that the rate is dominated by the p_1 channel. They find that the Hauser-Feshbach rates calculated by Woosley *et al.* in this energy range to be a factor of 5 higher than their measured rate, and for temperatures below about 4×10^{-3} GK, the Hauser-Feshbach rates are a factor of 10 too low.

Part V

Conclusions

Chapter 12 The $^{19}F(\alpha, n)^{22}Na$ Reaction

The cross sections for $^{19}F(\alpha, n)^{22}Na$ have been measured for $2.3 < E_\alpha < 3.1$ MeV, with a systematic uncertainty estimated to be 8.1%. The positions and widths of the observed resonances in $^{19}F(\alpha, n)^{22}Na$ agree well with those in the the 0° cross sections measured by van der Zwan and Geiger [Zwa77]. My cross sections, however, are much smaller than those measured by Balakrishnan *et al.* [Bal78], and the discrepancy may be due in part to that experiment's poor resolution and problems with target contamination.

Using the principle of detailed balance, the cross sections for $^{22}Na(n, \alpha_0)^{19}F$ were calculated from $0.26 < E_n < 640$ keV. No other (n, α_0) data are available for this energy range.

The resulting reaction rates for $^{19}F(\alpha, n_0)^{22}Na$, $^{19}F(\alpha, n)^{22}Na$, and $^{22}Na(n, \alpha_0)^{19}F$ were calculated from the cross sections by numerical integration. The rates calculated from the cross sections measured in this experiment alone account for $> 95\%$ of the rate at the temperatures of interest in the nucleosynthesis of ^{22}Na in supernovae (0.8 GK), and for 100.% of the rate at the temperatures of interest in novae (< 0.3 GK). Comparison of the $^{22}Na(n, \alpha_0)^{19}F$ reaction rate with Hauser-Feshbach calculations by Woosley *et al.* [Woo78] and Caughlan and Fowler [Cau88] for the $^{22}Na(n, \alpha)^{19}F$ rate show my rate to be low by a factor of 4 at low temperatures (0.01 GK) and a factor of 20 at higher temperatures (10 GK), but this might be expected since the Hauser-Feshbach rates include contributions from the (n, α_1) and (n, α_2) reactions which are known to be important. Improved Hauser-Feshbach calculations incorporating my experimental measurements would likely reduce the uncertainty associated with the total $^{22}Na(n, \alpha)^{19}F$ rate, which is currently estimated to be a factor of about two or three.

Improvements on the $^{19}F(\alpha, n)^{22}Na$ cross section measurement could be expected for the data near threshold (< 2.5 MeV), were it possible to reduce the amount of

contamination on the target. A remeasurement of the cross sections above the limit of this experiment, to improve on the Balakrishnan data, would be helpful to pin down the reaction rate above 1.0 GK. For the $^{22}\mathrm{Na}(n,\alpha_0)^{19}\mathrm{F}$ cross section and rate, it would be useful to measure the ratio of the n_1 to n_0 neutrons above the n_1 neutron threshold at 3.07 MeV.

Chapter 13 The ^{22}Ne$(p,n)^{22}$Na Reaction

The cross sections for ^{22}Ne$(p,n)^{22}$Na were measured for $3.7 < E_p < 5.4$ MeV, with a systematic uncertainty of 8.6 to 9.8%. Apart from one data point at 5.5(9) MeV measured by Takács *et al.* [Tak96], no cross sections have been measured in this energy range. In the region where the data overlap, my cross sections are higher than the Takács measurement.

Using the principle of detailed balance, the cross sections for ^{22}Na$(n,p_0)^{22}$Ne were calculated from $1.9 < E_n < 600$ keV. No other (n,p_0) data are available for this energy range.

The resulting reaction rate for ^{22}Ne$(p,n)^{22}$Na was calculated from the entire data set, and the ^{22}Na$(n,p_0)^{22}$Ne rate calculated for energies below the n_1 threshold. Again, these rates are lower, as expected, than the Hauser-Feshbach rates calculated by Woosley *et al.* [Woo78] and Caughlan and Fowler [Cau88], since the latter include contributions from the (n,p_1) reaction.

The ^{22}Ne$(p,n)^{22}$Na cross section measurements could certainly be improved by investigating different backings for the implanted targets to limit the (p,n) background from contamination. Measurements of the ratio of the various neutron groups as a function of energy would greatly reduce the uncertainty in the detector efficiency and allow the ^{22}Na$(n,p_0)^{22}$Ne cross sections to be calculated for a larger energy range. Lastly, Hauser-Feshbach calculations which include the effects of the measured ^{22}Na$(n,p_0)^{22}$Ne resonances would likely reduce the uncertainty currently associated with the ^{22}Na$(n,p_0)^{22}$Ne reaction rate.

Bibliography

[Aud95] G. Audi and A.H. Wapstra, Nucl. Phys. **A595** (1995) 409.

[Bai79] J.K. Bair and J. Gomez del Campo, Nucl. Sci. Eng. **71** (1979) 18.

[Bai73] J.K. Bair and F.X. Haas, Phys. Rev. C **7** (1973) 1356.

[Bai62] J.K. Bair and H.B. Willard, Phys. Rev. **128** (1962) 299.

[Bat59] R. Batchelor and J.H. Towle, Proc. Phys. Soc. 73 (1959) 307.

[Bec82] H.W. Becker, W.E. Kieser, C. Rolfs, H.P. Trautvetter, and M. Wiescher, Z. Phys. A **305** (1982) 319.

[Bal78] M. Balakrishnan, S. Kailas, and M.K. Mehta, Pramana **10** (1978) 329.

[Bri93] J.F. Briesmeister, ed., "MCNP – A General Monte Carlo N-Particle Transport Code, Version 4A," LA-12625-M, Los Alamos National Laboratory (1993).

[Bru94] C.R. Brune and R.W. Kavanagh, Nucl. Inst. Meth. **A343** (1994) 415, C.R. Brune, Ph.D. thesis, California Institute of Technology, 1994.

[Bru93] C.R. Brune, I. Licot, and R.W. Kavanagh, Phys. Rev. C **48** (1993) 3119.

[Car93] A.D. Carlson, W.P. Poenitz, G.M. Hale, R.W. Peelle, D.C. Dodder, C.Y. Fu, and W. Mannhart, National Institute of Standards and Technology Report NISTIR 4177 (May, 1993).

[Cau88] G.R. Caughlan and W.A. Fowler, Atomic Data Nucl. Data Tables **40** (1988) 283.

[Cla92] D.D. Clayton, Science **258** (1992) 970.

[Cla82] D.D. Clayton, in Essays in Nuclear Astrophysics, ed. C.A. Barnes, D.D. Clayton, and D.N. Schramm, Cambridge University Press (USA, 1982), pages 410-413.

[Cla75] D.D. Clayton, Astrophys. J. **198** (1975) 151.

[Coc95] A. Coc, R. Mochkovitch, Y. Oberto, J.-P. Thibaud, and E. Vangioni-Flam, Astron. Astrophys. **299** (1995) 479.

[Cro91] S. Croft, Nucl. Inst. Meth. **A307** (1991) 353.

[Ded62] K. Dedrick, Rev. Mod. Phys. **34** (1962) 429.

[Die97] R. Diehl, A. Iyudin, U. Oberlack, V. Schönfelder, H. Bloemen, C. Dupraz, W. Hermsen, J. Knödlseder, J. Ryan, and C. Winkler, Nucl. Phys. **A621** (1997) 79c.

[Dro87] M. Drosg and O. Schwerer, "Production of Monoenergetic Neutrons between 0.1 and 23 MeV," Handbook on Nuclear Activation Data, International Atomic Energy Agency, Vienna, 1987.

[Dro93] H.W. Drotleff, A. Denker, H. Knee, M. Soiné, G. Wolf, J.W. Hammer, U. Greife, C. Rolfs, and H.P. Trautvetter, Astrophys. J. **414** (1993) 735.

[End90] P.M. Endt, Nucl. Phys. A **521** (1990) 1.

[Ehe73] R. Ehehalt, Y. Shida, C. Signorini, and H. Morinaga, Il Nuovo Cimento **15** (1973) 209.

[Ehe71] R. Ehehalt, H. Morinaga, and Y. Shida, Z. Naturforsch **26** (1971) 590.

[Fir96] R.B. Firestone and V.S. Shirley, eds., Table of Isotopes, 8th edition, John Wiley & Sons (USA, 1996), volume II.

[Fow67] W.A. Fowler, G.R. Caughlan, and B.A. Zimmerman, Annu. Rev. Astron. Astrophys. **5** (1967) 525.

[Fre64] R.M. Freeman and G.S. Mani, Nucl. Phys. **51** (1964) 593.

[Fro90] F.H. Fröhner, Nucl. Sci. Eng. **106** (1990) 345.

[Gal90] R. Gallino, M. Busso, G. Picchio, and C.M. Raiteri, Nature **348** (1990) 298.

[Gei75] K.W. Geiger and L. van der Zwan, Nucl. Inst. Meth. **131** (1975) 315.

[Gib59] J.H. Gibbons and R.L. Macklin, Phys. Rev. **114** (1959) 571.

[Gle82] Yu.M. Gledenov, J. Kvitek, S. Marinova, Yu.P. Popov, J. Rigol, and V.I. Salatski, Z. Phys. A **308** (1982) 57.

[Hah95] K.I. Hahn, C.R. Brune, and R.W. Kavanagh, Phys. Rev. C **51** (1995) 1624; K.I. Hahn, personal communication.

[Han47] A.O. Hanson and J.L. McKibben, Phys. Rev. **72** (1947) 673.

[Hea89] R. Heaton, H. Lee. P. Skensved, and B.C. Robertson, Nucl. Inst. Meth. **A276** (1989) 529.

[Hen92] J.S. Hendricks and J.F. Briesmeister, IEEE Trans. Nucl. Sci. **39** (1992) 1035.

[Hol95] P. Holden and M.M. Woolfson, Earth, Moon and Planets **69** (1995) 201.

[Hsu94] H.H. Hsu, K.R. Alvar, and D.G. Vasilik, IEEE Trans. Nucl. Sci. **41** (1994) 938.

[Iyu95] A.F. Iyudin, K. Bennett, H. Bloemen, R. Diehl, W. Hermsen, G.G. Lichti, D. Morris, J. Ryan, V. Schönfelder, H. Steinle, A. Strong, M. Varendorff, and C. Winkler, Astron. Astrophys. **300** (1995) 422.

[Jac75] J.D. Jackson, Classical Electrodynamics, 2nd edition, John Wiley & Sons (USA, 1975), problem 11.20, page 568.

[Joh58] C.H. Johnson, A. Galonsky, and J.P. Ulrich, Phys. Rev. **109** (1958) 1243.

[Jos97] J. José and M. Hernanz, Nuclear Physics **A621** (1997) 491c.

[Kei77] J. Keinonen, M. Riihonen, and A. Anttila, Phys. Rev. C **15** (1977) 579.

[Kel91] S.E. Kellogg, personal communication.

[Koe97] P.E. Koehler, personal communication.

[Koe88] P.E. Koehler and H.A. O'Brien, Phys. Rev. C **38** (1988) 2019.

[Kun96] R. Kunz, S. Barth, A. Denker, H.W. Drotleff, J.W. Hammer, H. Knee, and A. Mayer, Phys. Rev. C **53** (1996) 2486.

[Kvi81] J. Kvitek, V. Hnatowicz, J. Červená, and J. Vacík, Z. Phys. A **299** (1981) 187.

[Lee76] T. Lee, D.A. Papanastassiou, and G.J. Wasserburg, Geophys. Res. Lett. **3** (1976) 109.

[Lee80] E.W. Lees, B.H. Patrick, and E.M. Bowey, Nucl. Inst. Meth. **171** (1980) 29.

[Leo87] W.R. Leo, Techniques for Nuclear and Particle Physics Experiments, Springer-Verlag (Germany, 1987), page 115.

[Lew90] R.S. Lewis, S. Amari, and E. Anders, Nature **348** (1990) 293.

[Lis75] H. Liskien and A. Paulsen, At. Data Nucl. Data Tables **15** (1975) 57.

[Maa78] J.W. Maas, A.J.C.D. Holvast, A. Baghus, H.J.M. Aarts, and P.M. Endt, Nucl. Phys. **A301** (1978) 213. The nine resonances used were those at 1530.03(15), 1951.6(3), 1966.46(19), 2323.1(2), 2378.3(2), 2435.1(3), 2632.9(3), 2865.8(3), and 2994.4(3) keV.

[Mac82] R.E. MacFarlane, D.W. Muir, and R.M. Boicourt, "The NJOY Nuclear Data Processing System, Volume I: User's Manual," LA-9303-M, Vol. I, (ENDF-324) (May 1982).

[Mac57] R.L. Macklin, Nucl. Inst. Meth. **1** (1957) 335.

[Mah82] W. Mahoney, J.C. Ling, A.S. Jacobson, and R.E. Lingenfelter, Astrophys. J. **262** (1982) 742.

[Mar94] V. Mares and H. Schraube, Nucl. Inst. Meth. **A337** (1994) 461.

[Mar91] V. Mares, G. Schraube, and H. Schraube, Nucl. Inst. Meth. **A307** (1991) 398.

[Mar60] J.B. Marion, R.J.A. Levesque, C.A. Ludemann, and R.W. Detenbeck, Nucl. Inst. Meth. **8** (1960) 297.

[Nat98] NNDC Online Data Service, National Nuclear Data Center, Brookhaven National Laboratory, `QCALC` program, available via ⟨URL: `telnet://NNDC@bnlnd2.dne.bnl.gov/`⟩, accessed April 16, 1998.

[Nie77] F. Niederer and P. Eberhardt, Meteoritics **12** (1977) 327.

[Nor84] E.R. Norman, T.E. Chupp, K.T. Lesko, P.J. Grant, and G. Woodruff, Phys. Rev. C **30** (1984) 30.

[OHa89] J.F. O'Hanlon, A User's Guide to Vacuum Technology, 2nd edition, John Wiley & Sons (U.S.A, 1989), page 312.

[Pre86] W.H. Press, B.P. Flannery, S.A. Teukolsky, and W.T. Vetterling, Numerical Recipes: The Art of Scientific Computing, Cambridge University Press (USA, 1986), pages 203-204.

[Rey60] J. Reynolds, Phys. Rev. Lett. **4** (1960) 8.

[Saa89] B. Saam, M. Skalsey, and J. Van House, Phys. Rev. C **40** (1989) R1563.

[Sai90] T. Saitoh and Y. Kawada, Nucl. Inst. Meth. **A369** (1996) 503.

[Seg77] E. Segrè, Nuclei and Particles, 2nd edition, Benjamin/Cummings Publishing Company, Inc. (USA, 1977), page 510.

[Sek76] K.K. Sekharan, H. Laumer, B.D. Kern, and F. Gabbard, Nucl. Inst. Meth. **133** (1976) 253.

[Sel67] E. Selin, S.E. Arnell, and O. Almén, Nucl. Inst. Meth. **56** (1967) 218.

[Seu87] S. Seuthe, H.W. Becker, A. Krauss, A. Redder, C. Rolfs, U. Schröder, H.P. Trautvetter, K. Wolke, S. Wüstenbecker, R.W. Kavanagh, and F.B. Waanders, Nucl. Inst. Meth. **A260** (1987) 33.

[She54] R. Sherr, C.W. Li, and R.F. Christy, Phys. Rev. **96** (1954) 1258.

[Ske85] R.T. Skelton, Ph.D. thesis, California Institute of Technology, 1985.

[Sta97] S. Starrfield, J.W. Truran, M. Wiescher, W.M. Sparks, Nuclear Physics **A621** (1997) 495c.

[Sta93] S. Starrfield, J.W. Truran, M. Politano, W.M. Sparks, I. Nofar, G. Shaviv, Physics Reports **227** (1993) 223.

[Tak96] S. Takács, F. Tárkáanyi, and S.M. Qaim, Appl. Radiat. Isot. **47** (1996) 303.

[Thi96] F.-K. Thielemann, K. Nomoto, and M. Hashimoto, Astrophys. J. **460** (1996) 408.

[Tim95] F.X. Timmes, S.E. Woosley, and T.A. Weaver, Astrophys. J. **98** (1995) 617.

[Wal49] R.L. Walker, Phys. Rev. **76** (1949) 244.

[Wan91] T.R. Wang, R.B. Vogelaar, and R.W. Kavanagh, Phys. Rev. C **43** (1991) 883.

[Wan93] J.C. Wang, G.L. Jensen, and J.B. Czirr, Nucl. Sci. Eng. **113** (1993) 77.

[Wes82] D. West and A.C. Sherwood, Ann. Nucl. Energy **9** (1982) 551.

[Wie81] M.E. Wiedenbeck and D.E. Greiner, Astrophys. J. **247** (1981) L119.

[Wil60] R.M. Williamson, T. Katman, and B.S. Burton, Phys. Rev **117** (1960) 1325.

[Woo95] S.E. Woosley and T.A. Weaver, Astrophys. J. Supp. **101** (1995) 181.

[Woo80] S.E. Woosley and T.A. Weaver, Astrophys. J. **238** (1980) 1017.

[Woo78] S.E. Woosley, W.A. Fowler, J.A. Holmes, and B.A. Zimmerman, At. Data Nucl. Data Tables **22** (1978) 371.

[Zie77] J.F. Ziegler, The Stopping and Ranges of Ions in Matter (Pergamon, New York, 1977), Volume 4.

[Zwa77] L. van der Zwan and K.W. Geiger, Nucl. Phys. **A284** (1977) 189.